

Synthesis, structure and electric conductivity of higher hydrides of ytterbium at high pressure

Tomasz Jaroń,^{a,b,c*} Jianjun Ying,^{b,d} Marek Tkacz,^e Adam Grzelak,^a Vitali B. Prakapenka,^f Viktor. V. Struzhkin^{b,g*}, Wojciech Grochala^{a*}

^aCentre of New Technologies, University of Warsaw, Banacha 2c, 02-097 Warsaw, Poland, ^bGeophysical Laboratory, Carnegie Institution of Washington, 5251 Broad Branch Road NW, Washington, DC 20015, USA, ^cFaculty of Chemistry, University of Warsaw, Pasteura 1, 02-089 Warsaw, Poland, ^dHPCAT, Geophysical Laboratory, Carnegie Institution of Washington, Argonne, IL 60439, USA, ^eInstitute for Physical Chemistry, Polish Academy of Science, Warsaw, Poland, ^fConsortium for Advanced Radiation Sources, The University of Chicago, Chicago, IL 60637, USA, ^gCenter for High Pressure Science and Technology Advanced Research, Shanghai 201203, China.

*e-mail: tjaron@uw.edu.pl, viktor.struzhkin@hpstar.ac.cn, w.grochala@cent.uw.edu.pl

ABSTRACT

While most of the rare earth metals readily form trihydrides, due to increased stability of the filled 4f electronic shell for Yb(II), only YbH_{2.67}, formally corresponding to Yb^{II}(Yb^{III}H₄)₂ (or Yb₃H₈), remains the highest hydride of ytterbium. Utilizing diamond anvil cell methodology and synchrotron powder x-ray diffraction we have attempted to push this limit further *via* hydrogenation of metallic Yb (at room temperature and heated *in situ*) and of Yb₃H₈. Compression of the latter has also been investigated in a neutral pressure transmitting medium (PTM). While the *in situ* heating of Yb facilitates the formation of YbH_{2+x} hydride, we have not observed the clear qualitative differences between the systems compressed in H₂ and He or Ne PTM. In all these cases a sequence of phase transitions from the unit cells of *P*-31m symmetry to the *I*4/m and *I*4/mmm systems occurred within *ca.* 13–18 GPa and around 27 GPa, respectively. At the same time, the molecular volume of the systems compressed in H₂ PTM is *ca.* 1.5% larger than of those compressed in inert gases, suggesting a small hydrogen uptake. Nevertheless, hydrogenation towards YbH₃ is incomplete, and polyhydrides do not form up to the highest pressure studied here (*ca.* 75 GPa). As pointed out by our electronic transport measurements under compression in NaCl PTM, the mixed-valence Yb₃H₈ retains its semiconducting character up to at least 50 GPa, although the very low remnant activation energy of conduction (<5 meV) suggests that the metallization under further compression should be achievable. Finally, we provide a theoretical description of a hypothetical stoichiometric YbH₃.

KEYWORDS

ytterbium, hydrogen, mixed-valence, electric conductivity, high pressure

1. Introduction

The enormous interest in diverse hydrogen-rich systems manifested in the last decades can be linked mainly to the two topics – energy storage in chemical compounds and phonon-driven

superconductivity (SC), depending on the nature of systems studied. Due to the high gravimetric efficiency required for the energy storage in most potential applications, the first area has been dominated by the materials composed predominantly of light elements such as Li, B, Al, etc.^{1–4} On the other hand, the hydrides which have been studied as potential superconductors are not limited in this respect and their components cover virtually the entire periodic table.^{5–8}

The recent upsurge in the search for high-temperature SC in hydrides under high pressure has been stimulated by Neil Ashcroft's idea of "chemical precompression" of hydrogen contained in hydrogen-rich chemical compounds.⁹ In such hydrogen-dominated systems (in terms of an atomic fraction) the hydrogen sub-lattice is expected to contribute to the metallic state at drastically lower pressures compared to elemental hydrogen. This would finally allow for taking an advantage of the large phonon frequencies related to the lightweight hydrogen atoms to raise the critical temperature of SC. SC might occur provided that the system features a high density of electronic states at the Fermi level and strong electron-phonon coupling. As a consequence of this concept, many binary and even more complex hydride-based systems have been screened theoretically¹⁰ leading ultimately to experimental discovery of superconductivity in some of them. Several hydrides, especially those containing the *p*-block and rare-earth (*RE*) elements,⁷ reveal strikingly-high critical temperatures of superconductivity (T_C): compressed H_2S forming superconducting H_3S phase of $T_C = 203$ K at 155 GPa,¹¹ an incompletely identified C-S-H material synthesized in a diamond anvil cell (DAC) of $T_C = 288$ K at 267 GPa,¹² LaH_{10} of $T_C = 250$ – 260 K upon compression to *ca.* 200 GPa,^{13–15} or YH_6 of $T_C \approx 220$ K at 166–183 GPa^{16,17} and YH_9 of $T_C = 243$ – 262 K at 182–201 GPa.^{17,18}

Considering the *RE*-based systems, in these superhydrides the hydrogen sub-lattice is usually composed of clathrate-like and other complex geometrical motifs or contain mixed molecular and atomic units.^{5,10,19} While the polyhydrides of exotic compositions may form in a megabar pressure range, they are preceded by more usual stoichiometries appearing at much lower pressure. Some of the latter also superconduct, as it has been verified experimentally or as expected based on computational screening.⁷ Obviously, lowering the pressure of synthesis of a superconducting hydride or metastability of such phases under as close to ambient conditions as possible would be beneficial for more thorough macroscopic studies and possible applications. Recently, such high-temperature superconducting phases have been found for the hydrides based on lanthanides below the megabar pressure region.^{20,21}

With the exception of Eu and Yb, all lanthanides are easily hydrogenated at room temperature, absorbing up to 300 mol% of hydrogen to form trihydrides, LnH_3 , already under the pressure of a few atmospheres,²² see also *Fig. S1* in the Supplementary Information (SI). However, due to the

stabilization of half-filled or filled 4f electronic shells for Eu(II) and Yb(II), respectively, oxidation of these elements to the trivalent state by hydrogen is much more difficult. While the corresponding dihydrides can be readily prepared,²² further absorption of hydrogen requires significantly higher pressure. The uptake of hydrogen by EuH₂ occurs only above 8.7 GPa, as has been reported by Matsuoka *et al.* based on x-ray diffraction and Eu-Mössbauer spectroscopy measurements.²³ At this pressure range a tetragonal EuH_{2+x} containing trivalent Eu³⁺ starts to form, and the latter remains the only detected oxidation state of Eu above 12.5 GPa.²⁴ Very recently, Semenok *et al.*²⁵ reported that EuH₉ is present in the samples already at 74 GPa, while the other europium superhydrides were detected within the range 74–130 GPa, some of them showing antiferromagnetic ordering. Unfortunately, the lower-pressure regime has not been studied in this work, leaving the gap between *ca.* 50 GPa for which EuH_{2+x} phases were reported and 74 GPa with the superhydride phases already formed.

In the case of ytterbium, some early reports indicated preparation of cubic YbH_{2+x}, *x* < 0.7, after reaction of this metal with hydrogen pressurized to *ca.* 120 bar.^{26–28} These findings have been clarified by Auffermann, who prepared the metastable higher hydride of ytterbium *via* a high-pressure, high-temperature reaction (200 – 3200 bar, >600 K).²⁹ While the major features of the powder x-ray diffraction pattern of YbH_{2+x} are compatible with an *fcc* unit cell reported earlier, application of powder neutron diffraction allowed for proper identification and refinement of its crystal structure. It appeared that the prepared compound can be described as YbH_{2.67}, *i.e.* Yb₃H₈ or Yb^{II}(Yb^{III}H₄)₂, and it crystallizes in a trigonal unit cell with close packing of the nine ytterbium atoms (stacking sequence: ...ABC...), while hydrogen occupies all the tetrahedral and 2/3 of the octahedral holes, and no disorder is observed in the structure. The crystal structures of the higher hydrides of Yb and Eu relevant to the current study were summarized in *Figure 1*.

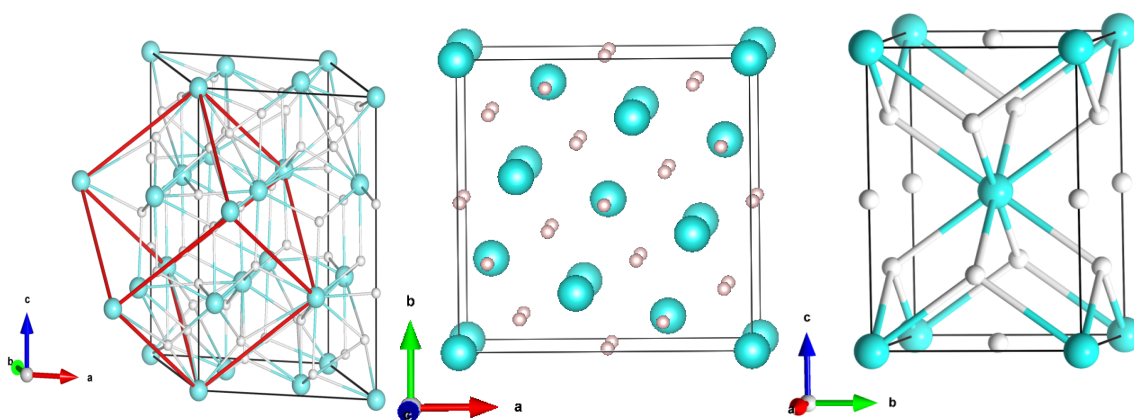


*Figure 1. Overview of the crystal structures of LnH_{2+x}, Ln = Yb, Eu: (a) Yb₃H₈ (YbH_{2.67}) *P*-31m,²⁹ (b) EuH_{2+x} *I*4/*m*; (c) EuH_{2+x} *I*4/*mmm*.²³*

The case of Yb(III) is special.² The vicinity of 4f shell closure for 4f¹³ electron configuration of Yb^{III} resembles the 3d⁹ configuration of parent oxocuprate superconductors, and the early DFT calculations indicated the possibility of significant contribution of H 1s states to the electron density at the Fermi level even for the stoichiometric Yb(III) hydrides.³⁰ Markedly, the only hole in the f electron set usually resides on the orbital which forms sigma* states with H(1s), which is analogous to a hole in the d set of Cu(II) residing in sigma* states with O(2p) in cuprates. Moreover, Yb(III) features a large magnetic moment of *ca.* 4.3–4.9 m_B corresponding formally to spin-½ which again renders it similar to Cu(II) in parent compounds of oxocuprate superconductors; thus, one might expect that electron doping could affect magnetism and lead to SC, just like for Cu(II) oxides. Last but not the least, more recent theoretical considerations suggest that besides yttrium and the lightweight lanthanides (Ln)^{31–33} the late lanthanides (Yb and Lu) should also form the superhydrides of T_C > 100 K.³⁴

The above findings have stimulated the present work in which we expand the chemistry of Yb-H system far beyond the previously studied range of *ca.* 0.3 GPa. Using DAC methodology we investigate the reaction of metallic Yb with H₂ and attempt further hydrogenation of Yb₃H₈ (YbH_{2.67}). We discuss the observed phase transitions as well as the possibility of formation of the higher hydrides of ytterbium, *i.e.* YbH_{2+x}, especially with x > 0.67. We have also studied the electronic transport of the mixed-valence Yb₃H₈ in the function of external pressure.

2. Methods

Experimental

Metallic Yb (99.9%, Sigma-Aldrich) and Au pressure standard (99.999%, Alfa Aesar) have been loaded into the DAC. Diamonds of 200–300 µm culets and rhenium gaskets have been used. Yb₃H₈ has been prepared according to the literature procedure,²⁹ and analyzed at ambient conditions using powder X-ray diffraction, *cf.* Fig. S2, and Tab. S1 in the SI. Ne, He, and H₂, loaded at *ca.* 170 MPa in the custom-designed gas loading systems of GL CIW and GSE CARS APS,³⁵ were applied as the pressure-transmitting medium (PTM).

High-pressure angle-dispersive x-ray diffraction (XRD) measurements have been performed using Advanced Photon Source synchrotron facility of Argonne National Laboratory. The measurements were carried out on sectors 13ID-D and 16ID-B operating at wavelengths from 0.2952 Å to 0.4066 Å. The sample to detector distance and other geometrical parameters were calibrated using LaB₆ or

CeO₂ standards. One of the samples of Yb in H₂ PTM was heated by the double-sided laser systems available at the beamlines, to the maximum temperatures of about 2100 K measured by fitting grey body thermal radiation.³⁶ Heating was carried out in several pulses lasting a few seconds, however, the overall amount of energy absorbed by the sample was not monitored. The heating was not uniform across the sample, which has manifested as variable amounts of crystalline phases present in various areas of the sample.

The electronic transport properties were carried out in a custom, miniaturized diamond anvil cell in a classical four-electrode geometry, using a Quantum Design Physical Property Measurement System. NaCl has been used as a PTM, and the pressure has been measured using ruby fluorescence.

The two-dimensional diffraction images were analyzed and integrated using the DIOPTAS software.³⁷ X-Cel has been used for pattern indexing.³⁸ The structures were refined in JANA2006.³⁹ The pseudo-Voigt function with Berar-Baldinozzi correction for asymmetry has been utilized for modeling of diffraction peak shape. The background was corrected by Legendre polynomials. The third-order Birch-Murnaghan equations of state (EoS) were fitted using EoSFit7-GUI program.^{40,41}

Computational

Density Functional Theory (DFT) calculations were performed using CASTEP.⁴² Generalized Gradient Approximation (GGA) was used with PBE functional adjusted for solids (PBEsol).⁴³ As hydrides usually require a large cutoff, here the value of 700 eV was applied to lead to very good energy convergence. The density of the k-point grid was set at 0.04 Å⁻¹; ultrasoft generated on the fly pseudopotentials were used as they provide more accurate lattice parameters. YbH₃ stoichiometry was assumed and the *I*4/mmm structure type exhibited by YbH_{2+x} at elevated pressures was adopted. The sqrt2 x sqrt2 x 1 supercell (Z=4) was applied to account for various magnetic ordering schemes; the formal spin of Yb(III) was used as the initial one in the first SCF step. For the magnetic structures, the DFT+U formalism has been used, with U = 5 eV for the 4*f* electrons of Yb. Enthalpies of various magnetic models and that of a nonmagnetic one, were calculated at several pressure values. Electronic density of states (DOS) was computed for the lowest enthalpy solutions.

3. Results and discussion

As it could be expected, the reaction between metallic ytterbium and hydrogen proceeds already at room temperature immediately after hydrogen loading to the cell. However, the unreacted metal is present in the whole pressure range studied, contributing to the strongest diffraction peaks (*cf.* Table 1), even for the largest pressure achieved for the sample compressed at room temperature to *ca.* 40

GPa, Fig. S3–S4. The evolution of the crystalline phases detected in this sample well corresponds to that described earlier, and YbH_2 remains the main hydridic phase.^{44–46} The crystalline phase which can be attributed to a higher hydride of ytterbium, YbH_{2+x} , is barely detected even at *ca.* 40 GPa, Fig. S3. However, the composition is variable from sample to sample, and in the case of the second DAC the clear, although relatively weak signals of the *P*-31m phase of YbH_{2+x} are visible already at 3.6 GPa, before heating of the sample, *cf.* Fig. 2a. This may be attributed to a variable degree of surface oxidation which should hamper further hydrogenation of the sample (this problem has been recently addressed by using a thin Pd coating for the synthesis of yttrium superhydrides).¹⁸

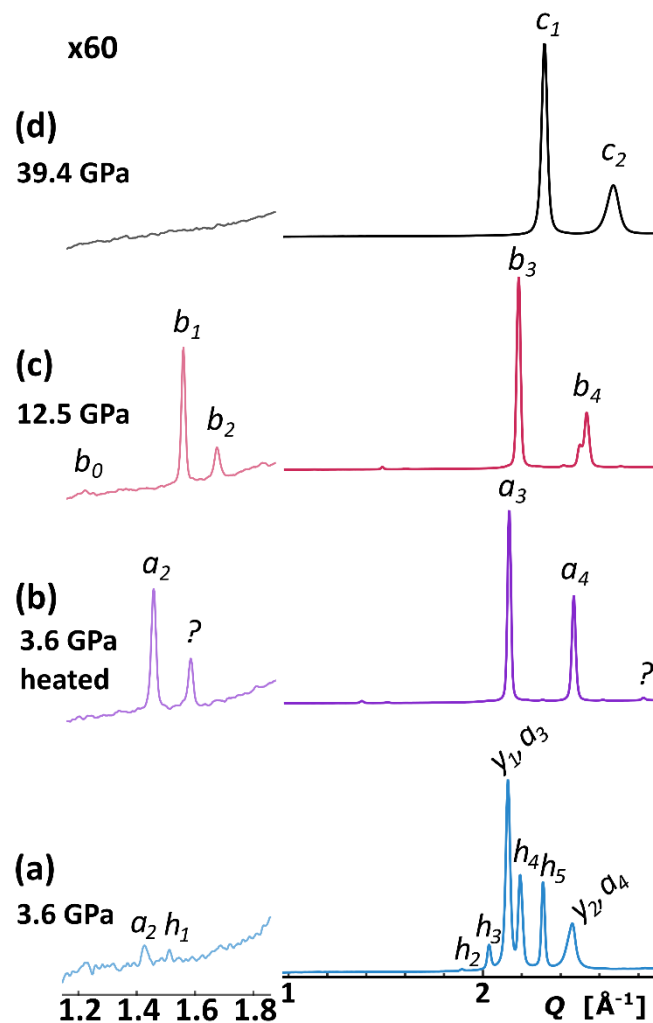


Figure 2. The diffraction patterns for the sample of Yb compressed in H_2 : (a) before and (b) after the laser heating at *ca.* 3.6 GPa; (c) after several rounds of laser heating (*ca.* 12.5 GPa); (d) at *ca.* 39.4 GPa. The low-Q part has been additionally presented in 60x magnification of intensity. $\lambda = 0.3344 \text{ \AA}$. *a* – YbH_{2+x} *P*-31m: 2-(1 0 1), 3-(0 0 3) and (2 -1 1), 4-(1 1 2); *b* – YbH_{2+x} *I*4/m: 0-(1 1 0), 1-(1 0 1), 2-(2 0 0), 3-(2 1 1), 4-(0 0 2) and (3 1 0); *c* – YbH_{2+x} *I*4/mmm: 1-(1 0 1), 2-(1 1 0) and (0 0 2); *h* – YbH_2 *Pnma*: 1-(101), 2-(0 0 2), 3-(0 1 1), 4-(1 0 2) and (2 0 0), 5-(1 1 1); *y* – Yb *Fm*-3m: 1-(1 1 1), 2-(0 0 2).

Table 1. Selected low-angle reflections originating from four distinct phases, as marked in Figures 2–4.

phase	reflections
YbH _{2+x} <i>P</i> -31m	a ₁ -(1 0 0), a ₂ -(1 0 1), a ₃ -(0 0 3) and (2 -1 1), a ₄ -(1 1 2), a ₅ -(2 -1 4) and (3 0 0)
YbH _{2+x} <i>I</i> 4/m	b ₁ -(1 0 1), b ₂ -(2 0 0), b ₃ -(2 1 1), b ₄ -(0 0 2) and (3 1 0), b ₅ -(3 1 2) and (4 2 0)
YbH _{2+x} <i>I</i> 4/mmm	c ₁ -(1 0 1), c ₂ -(0 0 2) and (1 1 0), c ₃ -(1 1 2) and (2 0 0), c ₄ -(1 0 3) and (2 1 1)
YbH ₂ <i>Pnma</i>	h ₁ -(101), h ₂ -(0 0 2), h ₃ -(0 1 1), h ₄ -(1 0 2) and (2 0 0), h ₅ -(1 1 1)
Yb <i>Fm</i> -3m	y ₁ -(1 1 1), y ₂ -(0 0 2)

The *in situ* laser heating of the partially hydrogenated ytterbium sample up to *ca.* 2100 K, with several pulses lasting a few seconds each, facilitates further hydrogenation and delivers the *P*-31m phase of YbH_{2+x} (Fig. 1a) which predominates the powder diffraction pattern, Fig. 2b and Fig. S5–S7. The YbH₂ is detected in the sample in a minor amount, together with very weak signals from an unidentified crystalline phase(s), Fig. S7. Although the sample remains not fully homogenous, it can be concluded that both these phases disappear after a few additional heating cycles on larger compression, Fig. S8. Above *ca.* 12.5 GPa the *P*-31m phase of YbH_{2+x} undergoes a transition to the *I*4/m phase which is isostructural to that reported for EuH_{2+x} at 8.7–9.7 GPa,²³ as indicated by the peak splitting (*e.g.* the peak *b*₄ of (0 0 2) and (3 1 0) reflections, while the (1 1 2) reflection of the trigonal phase contributes solely to the related *a*₄ peak) and the low-intensity reflections from the tetragonal superstructure (*e.g.* (1 1 0), (1 0 1), (2 0 0), marked as *b*₀, *b*₁, and *b*₂, respectively), Fig. 2c. During further compression, the latter phase symmetrizes to the *I*4/mmm structure, Fig. 2d, similar to EuH_{2+x} analog reported for the hydrogen pressures exceeding 9.7 GPa.²³ That second phase transition manifests itself as the vanishing superstructure signals and as a less pronounced peak splitting for the main peaks (*e.g.* *c*₂ corresponding to (0 0 2) and (1 1 0) reflections).

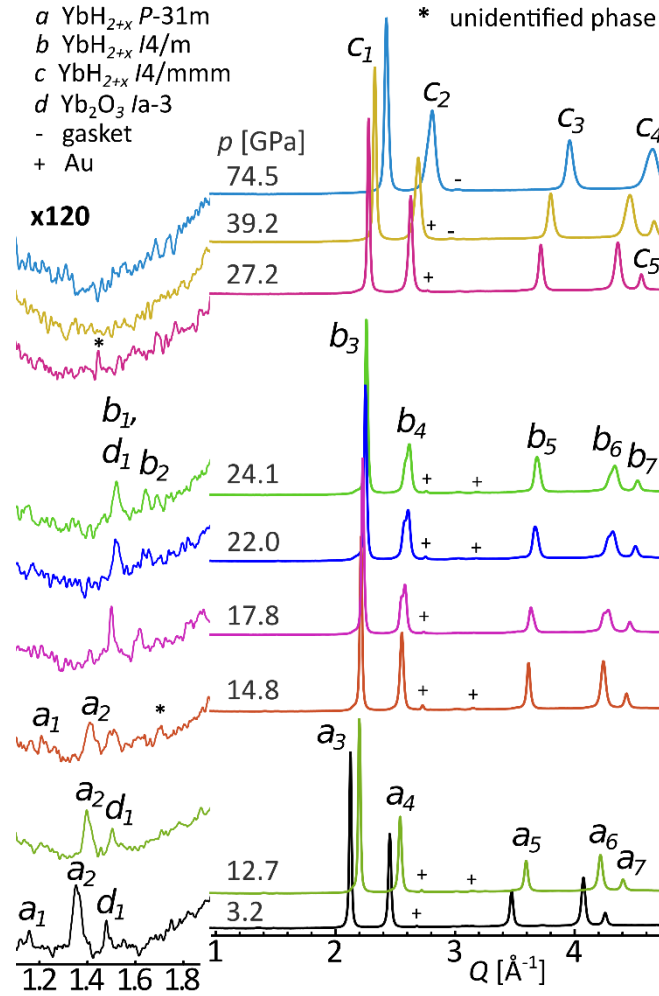


Figure 3. The diffraction patterns for the sample of Yb_3H_8 compressed in H_2 at room temperature. The low- Q part has been additionally presented in 120x magnification of intensity. $\lambda = 0.4066 \text{ \AA}$. a – YbH_{2+x} P -31m: 1-(1 0 0), 2-(1 0 1), 3-(0 0 3) and (2 -1 1), 4-(1 1 2); b – YbH_{2+x} $I4/m$: 1-(1 0 1), 2-(2 0 0), 3-(2 1 1), 4-(0 0 2) and (3 1 0); c – YbH_{2+x} $I4/mmm$: 1-(1 0 1), 2-(1 1 0) and (0 0 2).

To study the more homogenous samples including those of fixed content of hydrogen we have also investigated Yb_3H_8 (YbH_{2+x} , $x = 0.67$) which was prepared *ex-situ* according to the Auffermann's procedure²⁹; here, Yb_3H_8 was studied in DAC under compression in H_2 or in He or Ne pressure-transmitting media (PTM). The evolution of the crystalline phases for Yb_3H_8 compressed in H_2 or an inert PTM well corresponds to that observed for the sample of ytterbium heated in H_2 , Fig. 3, and Fig. S10–S23. It appears that the P -31m and $I4/m$ phases coexists within the range of *ca.* 13–18 GPa regardless of the PTM. The superstructure signals of the $I4/m$ phase vanish above *ca.* 27 GPa indicating the transition to the $I4/mmm$ phase. However, minor low-angle diffraction peaks have still been observed for some of the Yb_3H_8 samples compressed in the neutral PTM above 35 GPa (Fig. S20). The high-symmetry $I4/mmm$ phase of YbH_{2+x} remains stable up to the highest pressures reached in our investigations of *ca.* 75 GPa, Fig. 3.

The diffraction patterns from Yb_3H_8 samples in H_2 and Ar PTMs (Fig. 4) are quite similar to each other. All key reflections may be assigned to the same crystalline phase in both datasets. Such qualitative picture alone may suggest that an additional H_2 uptake does not occur for Yb_3H_8 even at 74.5 GPa, the highest pressure reached in our experiments. However, for the $I4/mmm$ phase, the corresponding diffraction signals are shifted towards lower Q values for the sample of Yb_3H_8 compressed in H_2 PTM indicating larger unit cell volume. This phenomenon is noticeable around 30 GPa, becoming obvious for larger pressures, Fig. S23.

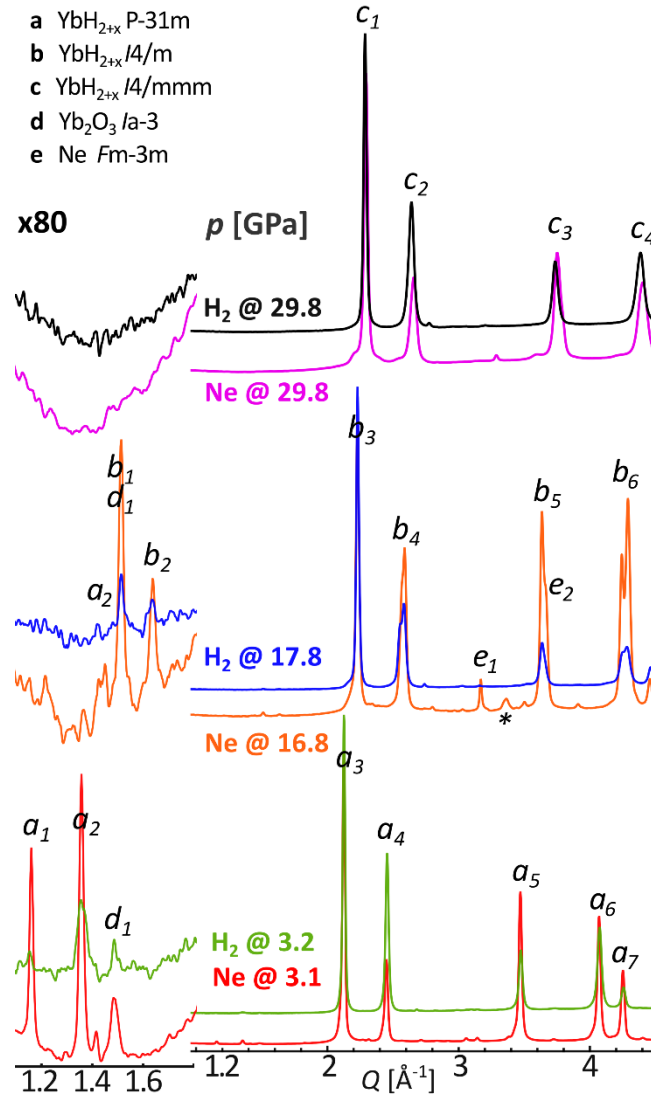


Figure 4. A comparison of the integrated diffraction data for Yb_3H_8 compressed in Ne and in H_2 . The low- Q region has been expanded (left). $\lambda = 0.3344 \text{ \AA}$ (Ne at 3.1 and 16.8 GPa), 0.2952 \AA (Ne at 29.8 GPa) and 0.4066 \AA (H_2). The most visible reflections of the YbH_{2+x} and Yb_2O_3 phases were marked: a – YbH_{2+x} P-31m: 1-(1 0 0), 2-(1 0 1), 3-(0 0 3) and (2 -1 1), 4-(1 1 2); b – YbH_{2+x} I4/m: 1-(1 0 1), 2-(2 0 0), 3-(2 1 1), 4-(0 0 2) and (3 1 0); c – YbH_{2+x} I4/mmm: 1-(1 0 1), 2-(0 0 2) and (1 1 0), 3-(1 1 2) and (2 0 0), 4-(1 0 3) and (2 1 1). * - the strongest signal from the unidentified phase.

EoS for Yb_3H_8 has been derived independently for the YbH_{2+x} crystalline phases present in the samples compressed in H_2 and Ne PTMs for the experimental runs covering a sufficient number of $V(p)$ data points, *Fig. S24–S29*. The obtained fit parameters are presented in *Table 2*, while some of the available EoS parameters for the related lanthanide hydrides were summarized in *Table S2*. In general, the V_0 of the low-pressure trigonal form is slightly lower than the high-pressure $I4/mmm$ phase, and the inverse trend is observed for their bulk moduli. The $P\text{--}31m$ form of Yb_3H_8 reveals V_0 comparable to the $Pnma$ YbH_2 of $V_0 = 35.63(7) \text{ \AA}^3$, but the former remains significantly less compressible, *cf. Fig. 5*, (for $Pnma$ YbH_2 $B_0 = 40.2(22) \text{ GPa}$).⁴⁵ The $I4/mmm$ phase of YbH_{2+x} present above *ca.* 27 GPa has a slightly smaller molecular volume with increased bulk modulus. These values fulfill a similar trend for the europium hydrides: the $I4/mmm$ phase of EuH_{2+x} of $V_0 = 38.8(1) \text{ \AA}^3$ (slightly bulkier than the Yb analog, according to the relation of Eu and Yb ionic radii) shows significantly higher bulk modulus in comparison to the dihydride ($B_0 = 69(2) \text{ GPa}$ vs. $B_0 = 40 - 45 \text{ GPa}$ for the two polymorphs of EuH_2).⁴⁷ Contrastingly, the trihydrides of the neighboring lanthanides (especially the Sm for Eu and Er or Tm for Yb) reveal rather larger values of the bulk moduli, while the V_0 of the $I4/mmm$ forms of EuH_{2+x} and YbH_{2+x} falls close to the values reported for hexagonal and cubic polymorphs of the respective LnH_3 , $\text{Ln} = \text{Sm}$ (for Eu), Er and Tm (for Yb), see *Table S2*.

Table 2. Summary of the parameters of the third-order Birch-Murnaghan EoS obtained from the compression data. The estimated standard deviations (E.S.D.) are given in parentheses. B_0' has been fixed for the final refinement. N – number of data points.

phase of YbH_{2+x}	PTM, sample	V_0 per Yb atom [\AA^3]	B_0 [GPa]	B_0'	max Δp [GPa]	χ^2 , N
$P\text{--}31m$	Ne , (g)	35.033(32)	56.13(63)	5.5	0.31	1.82, 19
	Ne , (h)	35.31(12)	53.4(19)	5.5	-0.43	6.82, 11
	H₂ , (d)	35.292(88)	55.0(14)	5.5	0.22	3.26, 8
$I4/m$	Ne , (g)	35.82(23)	63.1(22)	3.0	-0.31	1.15, 8
$I4/mmm$	Ne , (i)	34.05(34)	64.0(33)	4.5	1.03	7.95, 10
	H₂ , (d)	34.98(27)	59.7(23)	4.5	1.67	7.21, 19

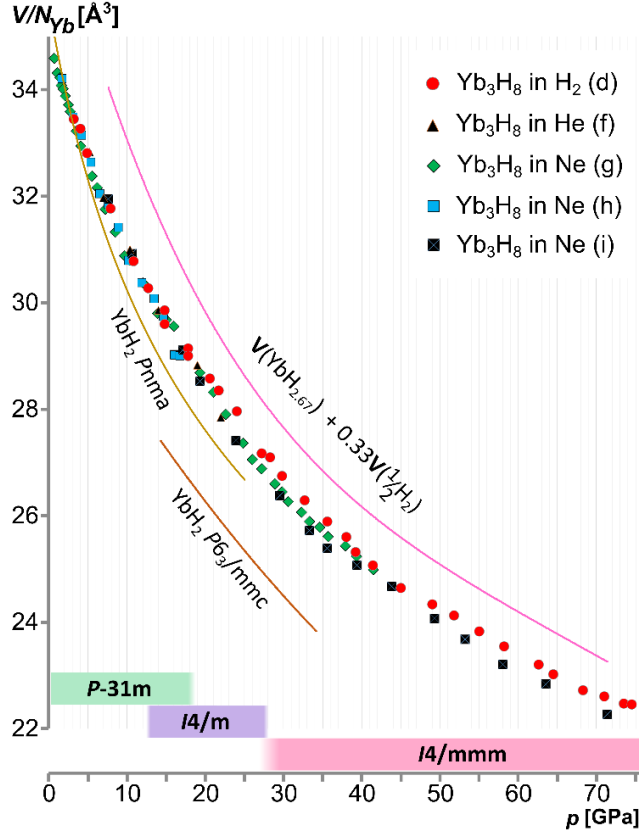


Figure 5. The volume per one ytterbium atom in the function of pressure for the compression of Yb_3H_8 in H_2 , He , and Ne at room temperature. The molecular volumes of YbH_2 (both polymorphs)⁴⁵ and the volume estimated for YbH_3 have also been plotted. The crystallographic phases of YbH_{2+x} , detected under a specific pressure range, are indicated at the bottom.

One key issue is that of the composition of the YbH_{2+x} specimen studied and that of a possible H_2 uptake by the sample in the H_2 atmosphere. Inspection of Fig. 5 reveals that the differences in the molar volume of the Yb_3H_8 specimen compressed in various PTM are only marginal, which is also reflected by the respective EoS curves, Fig. S30. However, on larger compression, the $V(p)$ curve seems to be slightly less steep for the sample pressurized in H_2 . Although the discrepancy is rather small and it may be caused by the errors in the determination of pressure in both types of samples, it is fairly consistent across the pressures for which the tetragonal phases are favored, especially 25–75 GPa. The EoS curves fitted for the $I4/mmm$ YbH_{2+x} in H_2 and Ne PTM fall apart by *ca.* 1.5% in terms of $V(p)$, Fig. S31. At the same time, a simple addition of 1/3 atomic volume of hydrogen would cause a raise in the molecular volume of $I4/mmm$ YbH_{2+x} by *ca.* 4.8% at this pressure range. Altogether, this might suggest that the composition of the sample compressed in excess H_2 is similar to $\text{YbH}_{2.77}$ rather than $\text{YbH}_{2.67}$.

Indeed, one might speculate that amount of 1/3 of vacancies is not a natural value for the tetragonal $I4/mmm$ cell and that 1/4 would be a more natural value (hence, $\text{YbH}_{2.75}$ would be a more appropriate

composition for such specimen, very close to $\text{YbH}_{2.77}$ suggested above from the EOS analyses). However, at lack of direct support for such a scenario one must refrain from making any firm conclusions here. In any case, the stoichiometry of the samples studied must be still far from the one expected for Yb(III)H_3 stoichiometry (Fig. 5). Resistance of Yb to be fully oxidized to Yb(III) in the hydride environment is remarkable; it turns out that only if a negative charge density on hydride is reduced, *e.g.* by binding it to B(III) in the form of BH_4^- anion, stoichiometric Yb(III) species may form and yet they are thermodynamically metastable at ambient (p,T) conditions.^{48–51}

The electric conductivity of formally mixed-valence species, be it $\text{YbH}_{2.67}$, $\text{YbH}_{2.75}$ or $\text{YbH}_{2.77}$, is of great interest in the context of potential generation of superconductivity in this material. Figure 6 (top) shows the electric resistivity versus temperature plot for a sample of Yb_3H_8 embedded in NaCl PTM. It is clear that the low-pressure phases of Yb_3H_8 show a semiconducting behavior as their resistivity is strongly decreasing with the temperature raising. Large drop of resistivity may be seen between 20.2 and 25.2 GPa, roughly corresponding to the second structural phase transition from the $I4/m$ to the $I4/mmm$ polymorphs.

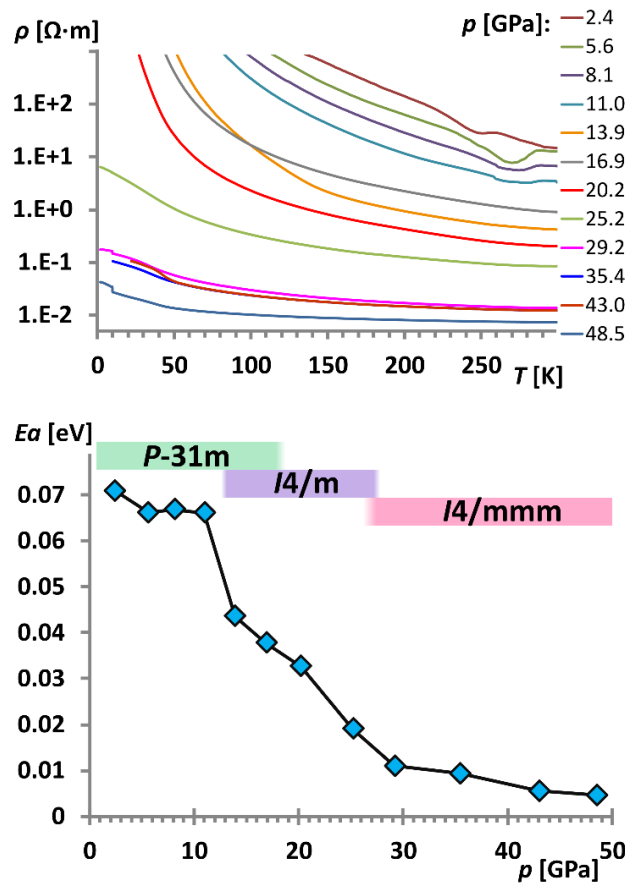


Figure 6. The resistivity vs. T [K] for Yb_3H_8 compressed in NaCl presented in a logarithmic scale indicating semiconductor-like behavior (top). Evolution of the activation energy of the electronic transport in the function of pressure (bottom). Despite the significant decrease of the E_a , the system avoids full metallization till 50 GPa (the highest pressure in our experiment).

Analysis of the activation energy for conductivity, E_a , (Fig. 6 bottom) suggests that E_a is already quite small (*ca.* 0.07 eV or 812 K) for Yb_3H_8 at low pressure (2.4 GPa). This feature comes certainly from the mixed-valence nature of the compound. One sharp drop of the E_a value is seen between 11.0 and 13.9 GPa, roughly corresponding to the first crystallographic phase transition. The second drop of the E_a value between 20 and 29 GPa is more subtle which suggests that the second phase transition affects E_a less considerably, and it is followed by the flattening of the curve above *ca.* 29 GPa. The E_a value determined at 48.5 GPa is as small as 0.005 eV (58 K) yet not null. Thus, Yb_3H_8 retains its semiconducting character even at *ca.* 50 GPa; this makes it similar to Fe_3O_4 .⁵² Metallicity, which would correspond to the formulation of $\text{Yb(III)}_3\text{H}_8(\text{e}^-)$ might be within the reach of the 1 Mbar experiments.

To learn what properties might be expected from fully stoichiometric YbH_3 , we have performed quantum mechanical calculations for this compound; we have assumed that it would adopt the $I4/mmm$ structure observed here, similar to the europium analog for which solely the Eu^{3+} oxidation state has been detected above 12.5 GPa.²⁴ Both the magnetic and nonmagnetic models were considered. Optimization of geometry resulted in the molar volumes approaching the experimental results, especially for the larger pressures, while the EOS for YbH_4 polyhydride of the same symmetry (as proposed for YH_4 and other REH_4)⁵³ is obviously different, Fig. S33, and it does not match experimental data.

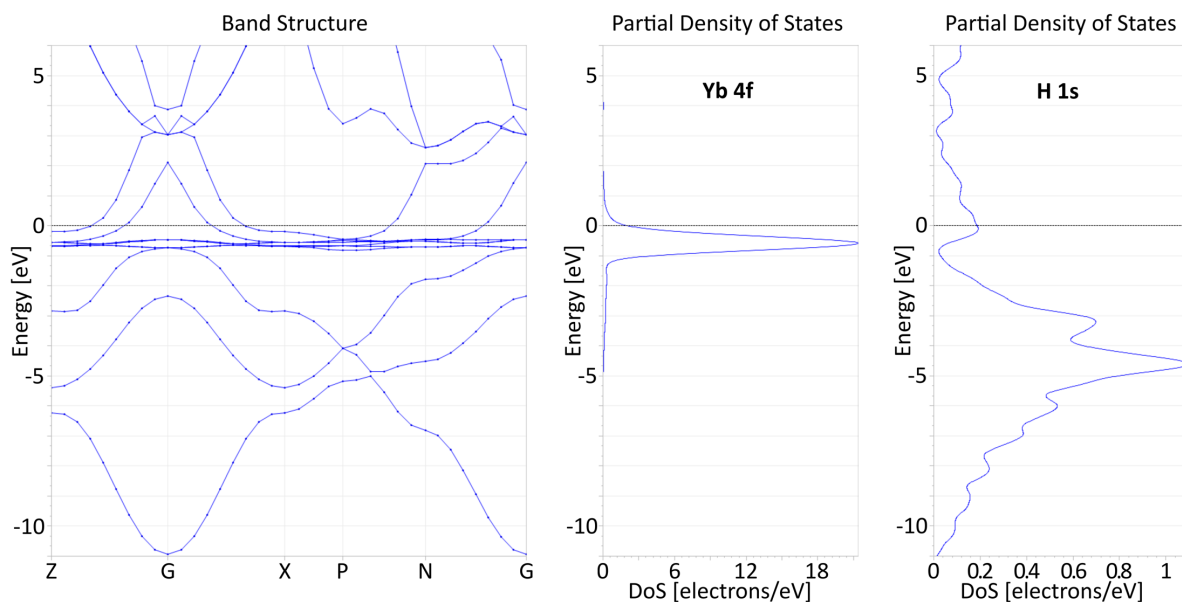


Figure 7. Electronic band structure (left) and DOS (Yb 4f center, H 1s right) for the spin-unpolarized solution, for YbH_3 in the $I4/mmm$ structure type at 50 GPa. Note the partial DOS scale difference between those for Yb and H electrons.

The DFT calculations for all magnetic states converge to solutions characterized by extremely small remnant magnetic moments. This implies that YbH₃ if prepared, could be a nonmagnetic solid. The corresponding spin-nonpolarized band structure and DOS (Figure 7) suggest that the compound would have a metallic nature, with several broad bands crossing the Fermi level. Both Yb(f) and H(s) states contribute to the states at the Fermi level; such strong hybridization was noticed previously.³⁰ The fact that the spin of Yb(III) would not localize but instead give rise to itinerant electrons may seem surprising but this could be due to strong hybridization with broad H(s) states (and this was the reason why we were targeting YbH₃ composition in experiments).

CONCLUSIONS

We have attempted synthesis of yet elusive ytterbium trihydride utilizing both metallic Yb and its currently most hydrogen-rich hydride, YbH_{2.67}, as the precursors in high-pressure hydrogenation (up to *ca.* 75 GPa). Our results point at the lack of a marked qualitative difference between these systems compressed in H₂ and the samples of YbH_{2.67} pressurized in He or Ne PTM. In all these cases a sequence of phase transitions from the unit cells of *P*-31m symmetry to the *I*4/m and *I*4/mmm systems occurred within *ca.* 13–18 GPa and around 27 GPa, respectively. The same tetragonal phases have been observed upon compression of EuH₂ in H₂ PTM: the *I*4/m system formed from the *P*6₃/mmc dihydride above 8.7 GPa and the high-symmetry *I*4/mmm phase containing Eu³⁺ has been detected above 9.7 GPa.²³ The fact that Eu³⁺ in a hydride environment forms at pressure as large as 9.7 GPa, while analogous species of Yb³⁺ may be prepared at several kPa, is following the standard redox potentials of the Eu³⁺/Eu²⁺ and Yb³⁺/Yb²⁺ pairs, which are –0.35 V and –1.05 V, respectively. In other words, Yb²⁺ can be easier oxidized by H₂ to Yb³⁺ than its Eu²⁺ analog.

For the highest pressure investigated here (25–75 GPa) corresponding to the *I*4/mmm phase, the molecular volume of the systems compressed in H₂ PTM consistently remains *ca.* 1.5% larger than that for the systems compressed in inert gas media. This indicates incremental hydrogenation towards YbH₃ and could correspond to the formation of YbH_{2.75–2.77}. However, additional research is necessary to fully identify the stoichiometry achieved upon hydrogenation, and even rather larger pressure is needed to push the system towards stoichiometric YbH₃ or ytterbium polyhydrides. Such compounds should be interesting due to their metallic nature, as expected on the basis of DFT calculations for YbH₃. At the same time, while the mixed-valence Yb₃H₈ retains its semiconducting character up to at least 50 GPa, the very low remnant activation energy of conduction (<5 meV) suggests that the metallization under further compression of this mixed-valence compound should also be achievable.

Acknowledgements

T. J. thanks Polish Ministry of Science and Higher education for funding (project "Mobility Plus" No. 1064/MOB/13/2014/0). W.G. acknowledges Polish National Science Center (NCN) for the Harmonia project 2012/06/M/ST5/00344. T. J. and V. V. S. acknowledge Dr. Ross Hrubia for the help in the XRD measurements, and Dr. Sergey Tkachev for Ne loading using GSECARS gas loading system at Advanced Photon Source (APS). Use of the COMPRES-GSECARS gas loading system was supported by COMPRES under National Science Foundation (NSF) Cooperative Agreement EAR 11-57758 and by GSECARS through NSF grant EAR-1128799 and DOE grant DE-FG02-94ER14466. Portions of this work were performed at GeoSoilEnviroCARS (The University of Chicago, Sector 13), APS, Argonne National Laboratory. GeoSoilEnviroCARS is supported by NSF – Earth Sciences (EAR-1128799) and DOE-GeoSciences (DE-FG02-94ER14466). Portions of this work were performed at HPCAT (Sector 16), APS Argonne National Laboratory. HPCAT operations are supported by DOE-NNSA under Award No. DE-NA0001974 and DOE-BES under Award No. DE-FG02-99ER45775, with partial instrumentation funding by NSF. This research used resources of the APS, a U.S. DOE Office of Science User Facility operated by Argonne National Laboratory under Contract No. DE-AC02-06CH11357.

References

- (1) Schlapbach, L.; Züttel, A. Hydrogen-Storage Materials for Mobile Applications. *Nature* **2001**, *414* (6861), 353–358. <https://doi.org/10.1038/35104634>.
- (2) Grochala, W.; Edwards, P. P. Thermal Decomposition of the Non-Interstitial Hydrides for the Storage and Production of Hydrogen. *Chem. Rev.* **2004**, *104* (3), 1283–1316. <https://doi.org/10.1021/cr030691s>.
- (3) Bannenberg, L. J.; Heere, M.; Benzidi, H.; Montero, J.; Dematteis, E. M.; Suwarno, S.; Jaroń, T.; Winny, M.; Orłowski, P. A.; Wegner, W.; Starobrat, A.; Fijałkowski, K. J.; Grochala, W.; Qian, Z.; Bonnet, J. P.; Nuta, I.; Lohstroh, W.; Zlotea, C.; Mounkachi, O.; Cuevas, F.; Chatillon, C.; Latroche, M.; Fichtner, M.; Baricco, M.; Hauback, B. C.; El Kharbachi, A. Metal (Boro-) Hydrides for High Energy Density Storage and Relevant Emerging Technologies. *Int. J. Hydrogen Energy* **2020**, *45* (58), 33687–33730. <https://doi.org/10.1016/j.ijhydene.2020.08.119>.
- (4) Modi, P.; Aguey-Zinsou, K. F. Room Temperature Metal Hydrides for Stationary and Heat Storage Applications: A Review. *Front. Energy Res.* **2021**, *9*. <https://doi.org/10.3389/fenrg.2021.616115>.
- (5) Wang, H.; Li, X.; Gao, G.; Li, Y.; Ma, Y. Hydrogen-Rich Superconductors at High Pressures. *Wiley Interdiscip. Rev. Comput. Mol. Sci.* **2018**, *8* (1), e1330. <https://doi.org/10.1002/wcms.1330>.
- (6) Bi, T.; Zarifi, N.; Terpstra, T.; Zurek, E. The Search for Superconductivity in High Pressure Hydrides. In *Reference Module in Chemistry, Molecular Sciences and Chemical Engineering*; Elsevier, 2019. <https://doi.org/10.1016/B978-0-12-409547-2.11435-0>.

- (7) Gao, G.; Wang, L.; Li, M.; Zhang, J.; Howie, R. T.; Gregoryanz, E.; Struzhkin, V. V.; Wang, L.; Tse, J. S. Superconducting Binary Hydrides: Theoretical Predictions and Experimental Progresses. *Mater. Today Phys.* **2021**, *21*, 100546. <https://doi.org/10.1016/j.mtphys.2021.100546>.
- (8) Struzhkin, V.; Li, B.; Ji, C.; Chen, X. J.; Prakapenka, V.; Greenberg, E.; Troyan, I.; Gavriluk, A.; Mao, H. K. Superconductivity in La and Y Hydrides: Remaining Questions to Experiment and Theory. *Matter Radiat. Extrem.* **2020**, *5* (2), 028201. <https://doi.org/10.1063/1.5128736>.
- (9) Ashcroft, N. W. Hydrogen Dominant Metallic Alloys: High Temperature Superconductors? *Phys. Rev. Lett.* **2004**, *92* (18), 187002. <https://doi.org/10.1103/PhysRevLett.92.187002>.
- (10) Hilleke, K. P.; Zurek, E. Tuning Chemical Precompression: Theoretical Design and Crystal Chemistry of Novel Hydrides in the Quest for Warm and Light Superconductivity at Ambient Pressures. **2021**.
- (11) Drozdov, A. P.; Eremets, M. I.; Troyan, I. A.; Ksenofontov, V.; Shylin, S. I. Conventional Superconductivity at 203 Kelvin at High Pressures in the Sulfur Hydride System. *Nature* **2015**, *525* (7567), 73–76. <https://doi.org/10.1038/nature14964>.
- (12) Snider, E.; Dasenbrock-Gammon, N.; McBride, R.; Debessai, M.; Vindana, H.; Vencatasamy, K.; Lawler, K. V.; Salamat, A.; Dias, R. P. Room-Temperature Superconductivity in a Carbonaceous Sulfur Hydride. *Nature* **2020**, *586* (7829), 373–377. <https://doi.org/10.1038/s41586-020-2801-z>.
- (13) Somayazulu, M.; Ahart, M.; Mishra, A. K.; Geballe, Z. M.; Baldini, M.; Meng, Y.; Struzhkin, V. V.; Hemley, R. J. Evidence for Superconductivity above 260 K in Lanthanum Superhydride at Megabar Pressures. *Phys. Rev. Lett.* **2019**, *122* (2), 027001. <https://doi.org/10.1103/PhysRevLett.122.027001>.
- (14) Drozdov, A. P.; Kong, P. P.; Minkov, V. S.; Besedin, S. P.; Kuzovnikov, M. A.; Mozaffari, S.; Balicas, L.; Balakirev, F. F.; Graf, D. E.; Prakapenka, V. B.; Greenberg, E.; Knyazev, D. A.; Tkacz, M.; Eremets, M. I. Superconductivity at 250 K in Lanthanum Hydride under High Pressures. *Nature* **2019**, *569* (7757), 528–531. <https://doi.org/10.1038/s41586-019-1201-8>.
- (15) Geballe, Z. M.; Liu, H.; Mishra, A. K.; Ahart, M.; Somayazulu, M.; Meng, Y.; Baldini, M.; Hemley, R. J. Synthesis and Stability of Lanthanum Superhydrides. *Angew. Chemie Int. Ed.* **2018**, *57* (3), 688–692. <https://doi.org/10.1002/anie.201709970>.
- (16) Troyan, I. A.; Semenok, D. V.; Kvashnin, A. G.; Sadakov, A. V.; Sobolevskiy, O. A.; Pudalov, V. M.; Ivanova, A. G.; Prakapenka, V. B.; Greenberg, E.; Gavriluk, A. G.; Lyubutin, I. S.; Struzhkin, V. V.; Bergara, A.; Errea, I.; Bianco, R.; Calandra, M.; Mauri, F.; Monacelli, L.; Akashi, R.; Oganov, A. R. Anomalous High-Temperature Superconductivity in YH6. *Adv. Mater.* **2021**, *33* (15), 2006832. <https://doi.org/10.1002/adma.202006832>.
- (17) Kong, P.; Minkov, V. S.; Kuzovnikov, M. A.; Drozdov, A. P.; Besedin, S. P.; Mozaffari, S.; Balicas, L.; Balakirev, F. F.; Prakapenka, V. B.; Chariton, S.; Knyazev, D. A.; Greenberg, E.; Eremets, M. I. Superconductivity up to 243 K in the Yttrium-Hydrogen System under High Pressure. *Nat. Commun.* **2021**, *12* (1), 5075. <https://doi.org/10.1038/s41467-021-25372-2>.
- (18) Snider, E.; Dasenbrock-Gammon, N.; McBride, R.; Wang, X.; Meyers, N.; Lawler, K. V.; Zurek, E.; Salamat, A.; Dias, R. P. Synthesis of Yttrium Superhydride Superconductor with a Transition Temperature up to 262 K by Catalytic Hydrogenation at High Pressures. *Phys. Rev. Lett.* **2021**, *126* (11), 117003. <https://doi.org/10.1103/PhysRevLett.126.117003>.
- (19) Zurek, E.; Bi, T. High-Temperature Superconductivity in Alkaline and Rare Earth Polyhydrides at High Pressure: A Theoretical Perspective. *J. Chem. Phys.* **2019**, *150* (5), 050901.

<https://doi.org/10.1063/1.5079225>.

- (20) Chen, W.; Semenok, D. V.; Huang, X.; Shu, H.; Li, X.; Duan, D.; Cui, T.; Oganov, A. R. High-Temperature Superconducting Phases in Cerium Superhydride with a T_c up to 115 K below a Pressure of 1 Megabar. *Phys. Rev. Lett.* **2021**, *127* (11), 117001. <https://doi.org/10.1103/PhysRevLett.127.117001>.
- (21) Di Cataldo, S.; Heil, C.; von der Linden, W.; Boeri, L. LaBH₈: Towards High- Low-Pressure Superconductivity in Ternary Superhydrides. *Phys. Rev. B* **2021**, *104* (2), L020511. <https://doi.org/10.1103/PhysRevB.104.L020511>.
- (22) Hirano, K.; Kadono, J.; Yamamoto, S.; Tanabe, T.; Miyake, H. Hydrogen-Absorbing Characteristics of 15 Rare Earth Elements. *J. Alloys Compd.* **2006**, *408–412*, 351–354. <https://doi.org/10.1016/j.jallcom.2005.04.052>.
- (23) Matsuoka, T.; Fujihisa, H.; Hirao, N.; Ohishi, Y.; Mitsui, T.; Masuda, R.; Seto, M.; Yoda, Y.; Shimizu, K.; Machida, A.; Aoki, K. Structural and Valence Changes of Europium Hydride Induced by Application of High-Pressure H₂. *Phys. Rev. Lett.* **2011**, *107* (2), 025501. <https://doi.org/10.1103/PhysRevLett.107.025501>.
- (24) Kuno, K.; Matsuoka, T.; Masuda, R.; Mitsui, T.; Seto, M.; Machida, A.; Fujihisa, H.; Hirao, N.; Ohishi, Y.; Shimizu, K.; Sasaki, S. Mixed-Valence State and Structure Changes of EuH_x ($x = 2$ and $2 < x \leq 3$) under High-Pressure H₂ Atmosphere. *J. Alloys Compd.* **2021**, *865*, 158637. <https://doi.org/10.1016/j.jallcom.2021.158637>.
- (25) Semenok, D. V.; Zhou, D.; Kvashnin, A. G.; Huang, X.; Galasso, M.; Kruglov, I. A.; Ivanova, A. G.; Gavriliuk, A. G.; Chen, W.; Tkachenko, N. V.; Boldyrev, A. I.; Troyan, I.; Oganov, A. R.; Cui, T. Novel Strongly Correlated Europium Superhydrides. *J. Phys. Chem. Lett.* **2021**, *12* (1), 32–40. <https://doi.org/10.1021/acs.jpclett.0c03331>.
- (26) Warf, J. C.; Hardcastle, K. A HIGHER HYDRIDE OF YTTERBIUM. *J. Am. Chem. Soc.* **1961**, *83* (9), 2206–2207. <https://doi.org/10.1021/ja01470a047>.
- (27) Warf, J. C.; Hardcastle, K. I. Rare Earth-Hydrogen Systems. IV. The Higher Hydride of Ytterbium, a New Type of Hydride. *Inorg. Chem.* **1966**, *5* (10), 1736–1740. <https://doi.org/10.1021/ic50044a021>.
- (28) Iwasieczko, W.; Drulis, M.; Drulis, H. Magnetic Properties of the β - and β' -Ytterbium Hydride Phases. *J. Alloys Compd.* **2001**, *327* (1–2), 11–16. [https://doi.org/10.1016/S0925-8388\(01\)01406-2](https://doi.org/10.1016/S0925-8388(01)01406-2).
- (29) Auffermann, G. Hochdrucksynthese Und Kristallstruktur von YbH₂, 67. *Zeitschrift für Anorg. und Allg. Chemie* **2002**, *628* (7), 1615. [https://doi.org/10.1002/1521-3749\(200207\)628:7<1615::AID-ZAAC1615>3.0.CO;2-W](https://doi.org/10.1002/1521-3749(200207)628:7<1615::AID-ZAAC1615>3.0.CO;2-W).
- (30) Jaroń, T.; Grochala, W.; Hoffmann, R. Towards Superconductivity in Hydrides: Computational Studies of Two Hypothetical Ternary Compounds, YbIIBeH₄ and Cs₃YbIIH₆. *J. Mol. Model.* **2007**, *13* (6–7), 769–774. <https://doi.org/10.1007/s00894-007-0183-x>.
- (31) Li, Y.; Hao, J.; Liu, H.; Tse, J. S.; Wang, Y.; Ma, Y. Pressure-Stabilized Superconductive Yttrium Hydrides. *Sci. Rep.* **2015**, *5* (1), 9948. <https://doi.org/10.1038/srep09948>.
- (32) Liu, H.; Naumov, I. I.; Hoffmann, R.; Ashcroft, N. W.; Hemley, R. J. Potential High-Tc Superconducting Lanthanum and Yttrium Hydrides at High Pressure. *Proc. Natl. Acad. Sci. U. S. A.* **2017**, *114* (27), 6990–6995. <https://doi.org/10.1073/pnas.1704505114>.
- (33) Peng, F.; Sun, Y.; Pickard, C. J.; Needs, R. J.; Wu, Q.; Ma, Y. Hydrogen Clathrate Structures in

- Rare Earth Hydrides at High Pressures: Possible Route to Room-Temperature Superconductivity. *Phys. Rev. Lett.* **2017**, *119* (10), 107001. <https://doi.org/10.1103/PhysRevLett.119.107001>.
- (34) Sun, W.; Kuang, X.; Keen, H. D. J.; Lu, C.; Hermann, A. Second Group of High-Pressure High-Temperature Lanthanide Polyhydride Superconductors. *Phys. Rev. B* **2020**, *102* (14), 144524. <https://doi.org/10.1103/PhysRevB.102.144524>.
 - (35) Rivers, M.; Prakapenka, V.; Kubo, A.; Pullins, C.; Holl, C.; Jacobsen, S. The COMPRES/GSECARS Gas-Loading System for Diamond Anvil Cells at the Advanced Photon Source. *High Press. Res.* **2008**, *28* (3), 273–292. <https://doi.org/10.1080/08957950802333593>.
 - (36) Prakapenka, V. B.; Kubo, A.; Kuznetsov, A.; Laskin, A.; Shkurikhin, O.; Dera, P.; Rivers, M. L.; Sutton, S. R. Advanced Flat Top Laser Heating System for High Pressure Research at GSECARS: Application to the Melting Behavior of Germanium. *High Press. Res.* **2008**, *28* (3), 225–235. <https://doi.org/10.1080/08957950802050718>.
 - (37) Prescher, C.; Prakapenka, V. B. DIOPTAS : A Program for Reduction of Two-Dimensional X-Ray Diffraction Data and Data Exploration. *High Press. Res.* **2015**, *35* (3), 223–230. <https://doi.org/10.1080/08957959.2015.1059835>.
 - (38) Neumann, M. A. X-Cell: A Novel Indexing Algorithm for Routine Tasks and Difficult Cases. *J. Appl. Crystallogr.* **2003**, *36* (2), 356–365. <https://doi.org/10.1107/S0021889802023348>.
 - (39) Petricek, V.; Dusek, M.; Palatinus, L.; Petříček, V.; Dušek, M.; Palatinus, L.; Petríček, V.; Dušek, M.; Palatinus, L. Crystallographic Computing System JANA2006: General Features. *Zeitschrift fur Krist.* **2014**, *229* (5), 345–352. <https://doi.org/10.1515/zkri-2014-1737>.
 - (40) Angel, R. J.; Gonzalez-Platas, J.; Alvaro, M. EosFit7c and a Fortran Module (Library) for Equation of State Calculations. *Zeitschrift fur Krist.* **2014**, *229* (5), 405–419. <https://doi.org/10.1515/zkri-2013-1711>.
 - (41) Gonzalez-Platas, J.; Alvaro, M.; Nestola, F.; Angel, R. EosFit7-GUI: A New Graphical User Interface for Equation of State Calculations, Analyses and Teaching. *J. Appl. Crystallogr.* **2016**, *49* (4), 1377–1382. <https://doi.org/10.1107/S1600576716008050>.
 - (42) Clark, S. J.; Segall, M. D.; Pickard, C. J.; Hasnip, P. J.; Probert, M. I. J. J.; Refson, K.; Payne, M. C. First Principles Methods Using CASTEP. *Zeitschrift fur Krist.* **2005**, *220* (5/6), 567–570. <https://doi.org/10.1524/zkri.220.5.567.65075>.
 - (43) Perdew, J. P.; Ruzsinszky, A.; Csonka, G. I.; Vydrov, O. A.; Scuseria, G. E.; Constantin, L. A.; Zhou, X.; Burke, K. Restoring the Density-Gradient Expansion for Exchange in Solids and Surfaces. *Phys. Rev. Lett.* **2008**, *100* (13), 136406. <https://doi.org/10.1103/PhysRevLett.100.136406>.
 - (44) Takemura, K.; Syassen, K. Pressure-Volume Relations and Polymorphism of Europium and Ytterbium to 30 GPa. *J. Phys. F Met. Phys.* **1985**, *15* (3), 543–559. <https://doi.org/10.1088/0305-4608/15/3/010>.
 - (45) Olsen, J. S.; Buras, B.; Gerward, L.; Johansson, B.; Lebech, B.; Skriver, H. L.; Steenstrup, S. A New High-Pressure Phase and the Equation of State of YbH₂. *Phys. Scr.* **1984**, *29* (5), 503–507. <https://doi.org/10.1088/0031-8949/29/5/016>.
 - (46) Klotz, S.; Casula, M.; Komatsu, K.; Machida, S.; Hattori, T. High-Pressure Structure and Electronic Properties of YbD₂ to 34 GPa. *Phys. Rev. B* **2019**, *100* (2), 020101. <https://doi.org/10.1103/PhysRevB.100.020101>.

- (47) Matsuoka, T.; Fujihisa, H.; Hirao, N.; Ohishi, Y.; Mitsui, T.; Masuda, R.; Seto, M.; Yoda, Y.; Shimizu, K.; Machida, A.; Aoki, K. Erratum: Structural and Valence Changes of Europium Hydride Induced by Application of High-Pressure H₂ (Physical Review Letters (2011) 107 (025501) DOI: 10.1103/PhysRevLett.107.025501). *Phys. Rev. Lett.* **2019**, 122 (17), 179901. <https://doi.org/10.1103/PhysRevLett.122.179901>.
- (48) Olsen, J. E.; Frommen, C.; Sørby, M. H.; Hauback, B. C. Crystal Structures and Properties of Solvent-Free LiYb(BH₄)₄-xClx, Yb(BH₄)₃ and Yb(BH₄)₂-xClx. *RSC Adv.* **2013**, 3 (27), 10764. <https://doi.org/10.1039/c3ra40435h>.
- (49) Eirik Olsen, J.; Frommen, C.; Jensen, T. R.; Riktor, M. D.; Sørby, M. H.; Hauback, B. C. Structure and Thermal Properties of Composites with RE-Borohydrides (RE. *RSC Adv.* **2014**, 4, 1570–1582. <https://doi.org/10.1039/c3ra44012e>.
- (50) Wegner, W.; Jaroń, T.; Grochala, W. Preparation of a Series of Lanthanide Borohydrides and Their Thermal Decomposition to Refractory Lanthanide Borides. *J. Alloys Compd.* **2018**, 744. <https://doi.org/10.1016/j.jallcom.2018.02.020>.
- (51) Wegner, W.; Jaroń, T.; Grochala, W. MYb(BH₄)₄ (M = K, Na) from Laboratory X-Ray Powder Data. *Acta Crystallogr. Sect. C Cryst. Struct. Commun.* **2013**, 69 (11), 1289–1291. <https://doi.org/10.1107/S0108270113027145>.
- (52) Chen, K.; Baudelet, F.; Mijiti, Y.; Nataf, L.; Di Cicco, A.; Hu, Z.; Agrestini, S.; Komarek, A. C.; Sougrati, M.; Haines, J.; Rouquette, J.; Kong, Q.; Weng, T. C. Revisiting the Phase Transition of Magnetite under Pressure. *J. Phys. Chem. C* **2019**, 123 (34), 21114–21119. <https://doi.org/10.1021/acs.jpcc.9b04140>.
- (53) Liu, L. L.; Sun, H. J.; Wang, C. Z.; Lu, W. C. High-Pressure Structures of Yttrium Hydrides. *J. Phys. Condens. Matter* **2017**, 29 (32), 325401. <https://doi.org/10.1088/1361-648X/aa787d>.

Supplementary Information

Synthesis, structure and electric conductivity of higher hydrides of ytterbium at high pressure

Tomasz Jaroń,^{a,b,c*} Jianjun Ying,^{b,d} Marek Tkacz,^e Adam Grzelak,^a Vitali B. Prakapenka,^f Viktor. V. Struzhkin^{b,g*}, Wojciech Grochala^{a*}

^aCentre of New Technologies, University of Warsaw, Banacha 2c, 02-097 Warsaw, Poland,
^bGeophysical Laboratory, Carnegie Institution of Washington, 5251 Broad Branch Road NW, Washington, DC 20015, USA, ^cFaculty of Chemistry, University of Warsaw, Pasteura 1, 02-089 Warsaw, Poland, ^dHPCAT, Geophysical Laboratory, Carnegie Institution of Washington, Argonne, IL 60439, USA, ^eInstitute for Physical Chemistry, Polish Academy of Science, Warsaw, Poland, ^fConsortium for Advanced Radiation Sources, The University of Chicago, Chicago, IL 60637, USA, ^gCenter for High Pressure Science and Technology Advanced Research, Shanghai 201203, China.

*e-mail: tjaron@uw.edu.pl, viktor.struzhkin@hpstar.ac.cn, w.grochala@cent.uw.edu.pl

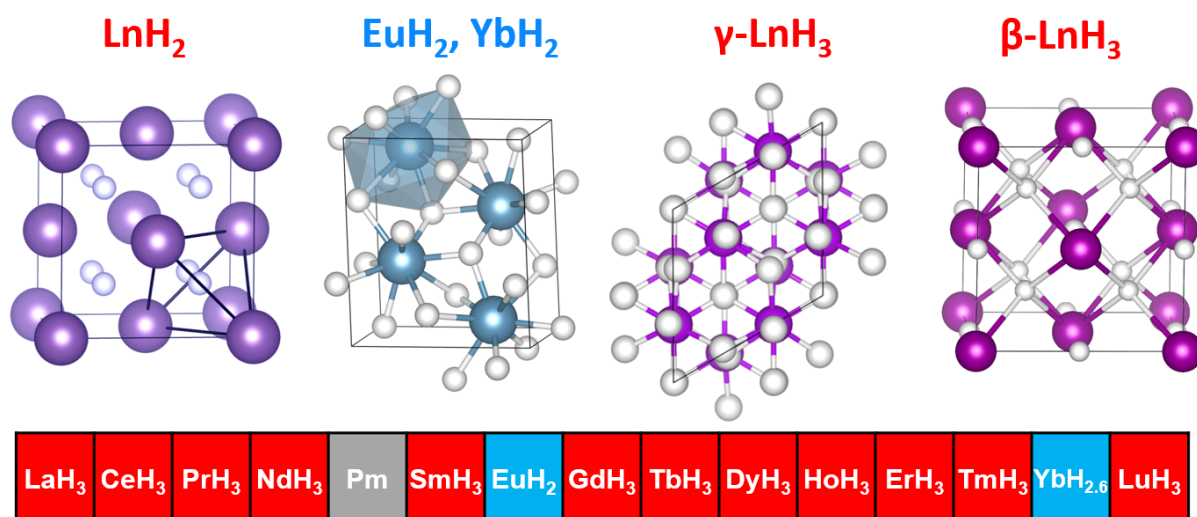


Figure S1. The crystal structures adopted by lanthanide hydrides near ambient pressure. EuH_2 and YbH_2 of ionic character crystallize in PbCl_2 structure ($Pnma$), while the other lanthanide dihydrides (metallic) – in fcc CaF_2 structure. The early LnH_3 crystallize in an fcc structure of LnH_2 , but with filled octahedral sites, while the later LnH_3 – in an hcp structure of HoH_3 type. The stoichiometry of LnH_x achievable at the pressures up to ca. 0.3 GPa has been listed at the bottom.

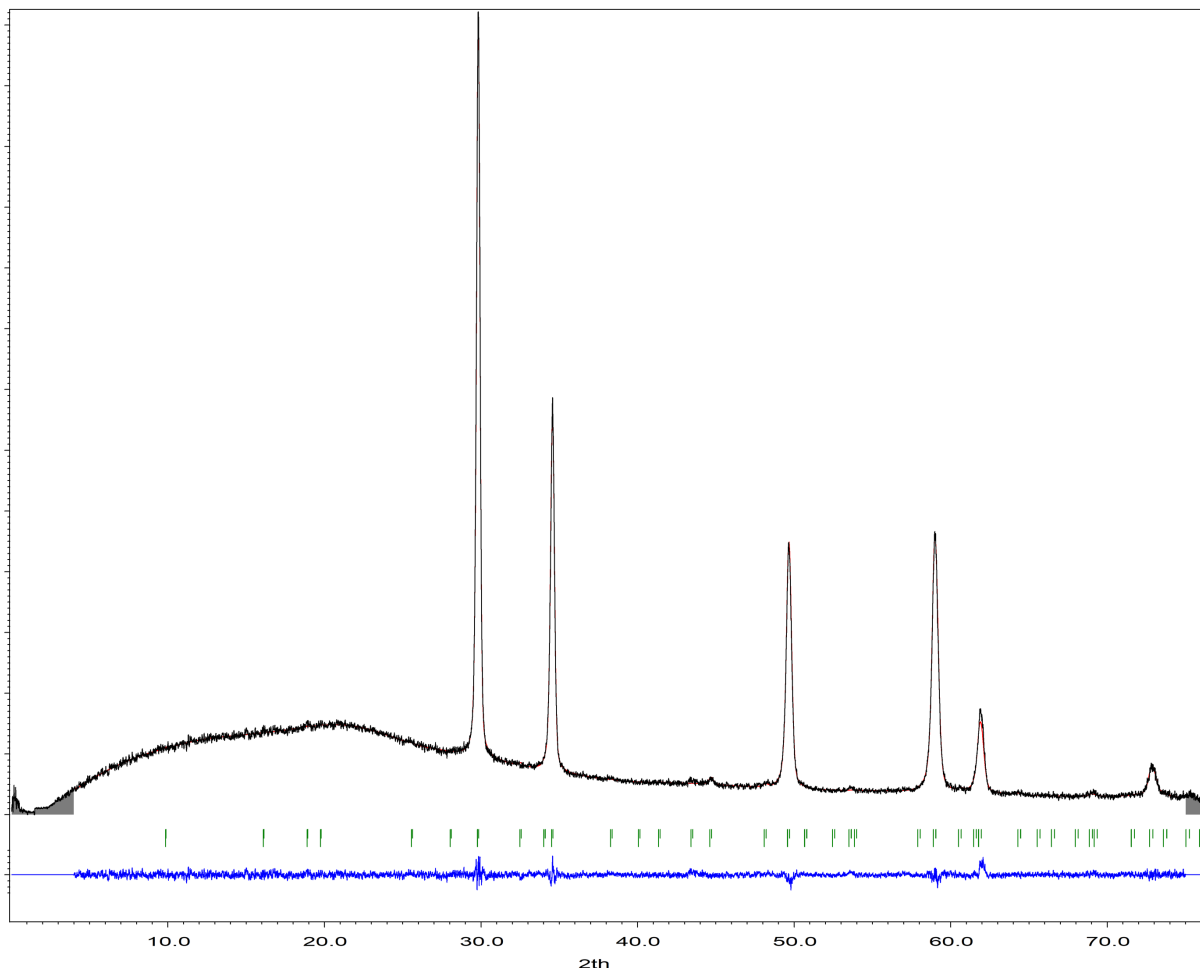


Figure S2. The PXD pattern of Yb_3H_8 measured under ambient conditions. Black curve – measured data, red – calculated, bottom – difference plot (Rietveld refinement). Cu K α radiation has been used ($\lambda \approx 1.5406 \text{ \AA}$).

Table S1. The results of Rietveld refinement of Yb_3H_8 measured under ambient conditions.

p [atm]	1		
T [°C]	RT, ca. 25		
space group	$P\bar{3}1m$ (162)		
a [Å]	6.3699(18)		
c [Å]	9.007(5)		
V [Å ³]	316.50(10)		
3Z	9		
V/3Z [Å ³]	35.167(11)		
wRp; cwRp [%]	4.00; 10.51		
d _{calc} [g cm ⁻³]	8.298(3)		
Yb1	0	0	Biso 2.39(6)*
Yb2	1/3	2/3	Biso 2.39(6)*
Yb3	0.3484(5)	0	0.3298(10) Biso 2.39(6)*
H1	0	0	0.644 Biso 3**
H2	1/3	2/3	0.219 Biso 3**
H3	0.322	0	0.5812 Biso 3**
H4	0.356	0	0.0757 Biso 3**
H5	0.2364	0	0.8319 Biso 3**

* Uiso of all Yb atoms has been set as equal, ** the parameters of H atoms were not refined

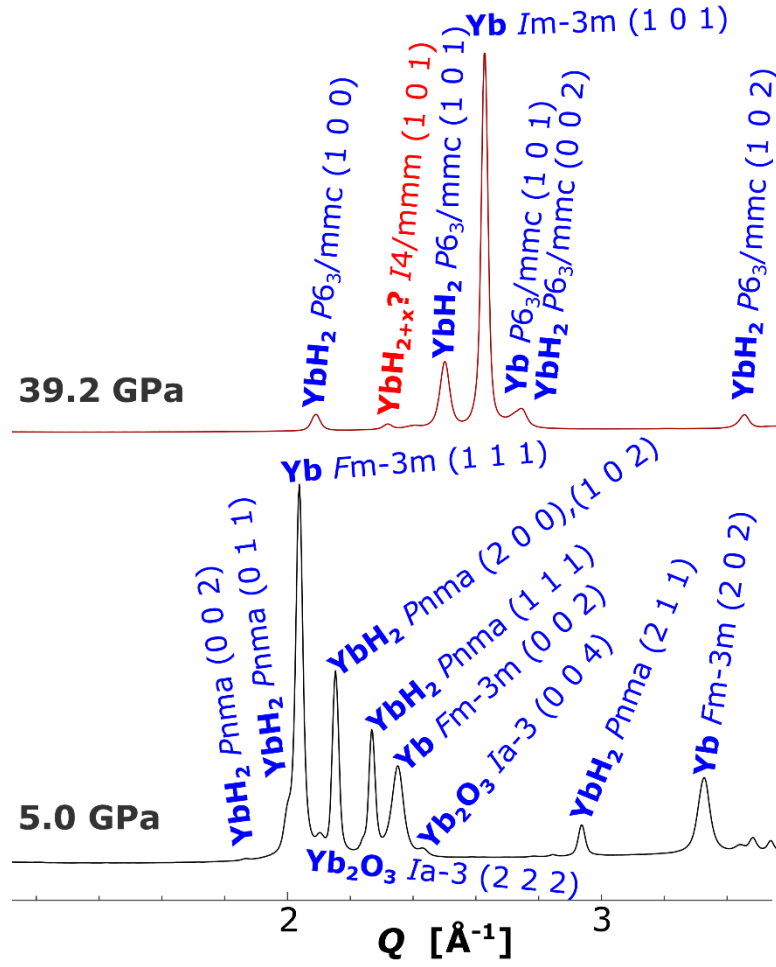


Figure S3. The diffraction data for the products of the reaction between Yb and H_2 performed at room temperature: $p = 5.0$ GPa and 39.2 GPa. The low- Q area has only been shown for better visibility. $\lambda = 0.3344$ \AA . The most visible signal possibly originating from the higher ytterbium hydride has been marked with the red font. YbH_{2+x} : $I4/mmm$, $a \approx 3.307$ \AA , $c \approx 4.709$ \AA , $V \approx 51.49$ \AA^3 .

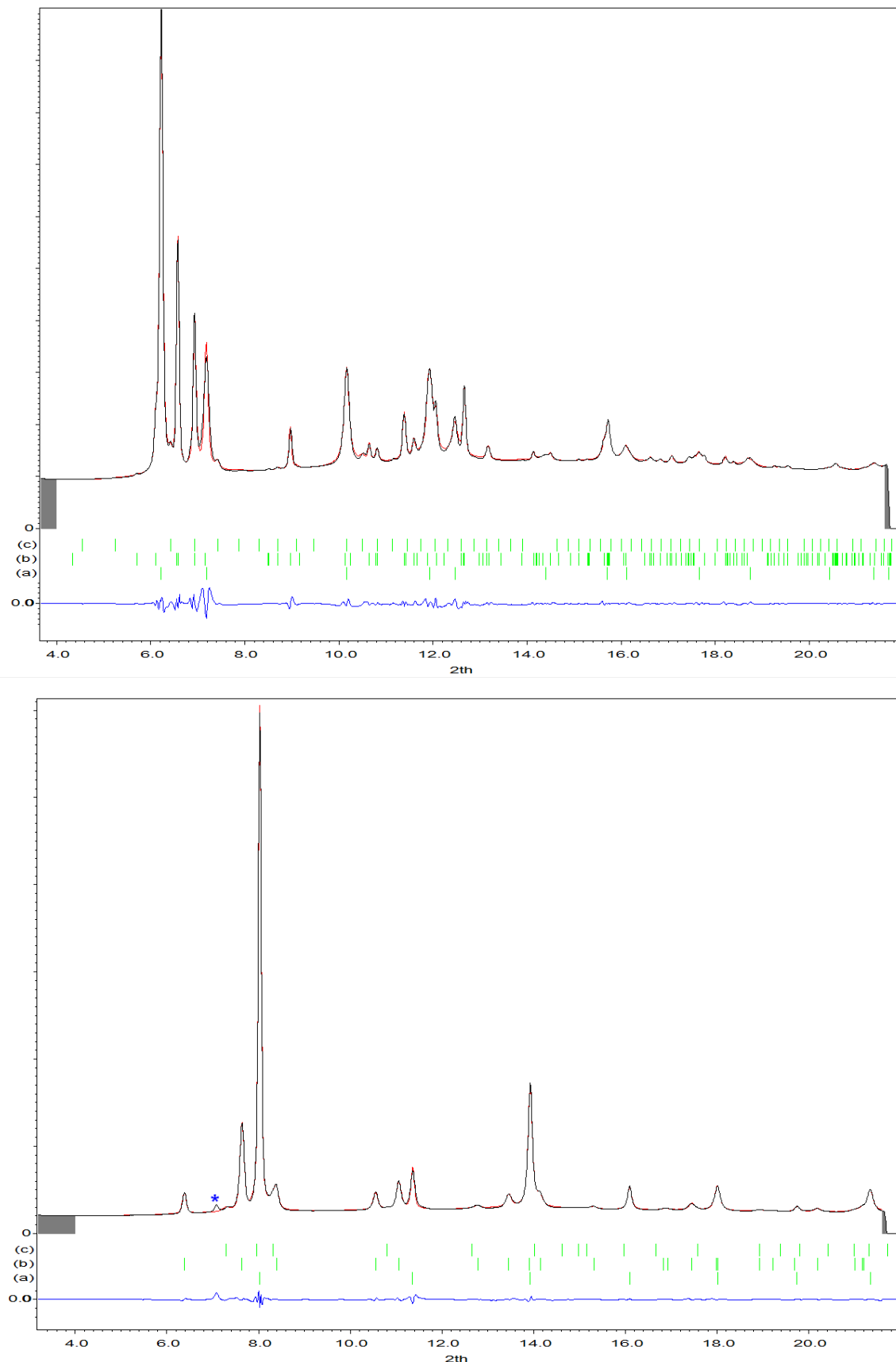


Figure S4. The typical diffraction data for the products of the reaction between Yb and H_2 performed at room temperature. **Top:** $p = 5.0$ GPa, (a) – Yb Fm-3m, (b) – YbH_2 Pnma, (c) – Yb_2O_3 Ia-3. **Bottom:** $p = 39.2$ GPa, (a) – Yb Im-3m, (b) – YbH_2 P6₃/mmc, (c) – Yb P6₃/mmc, * – $(1\ 0\ 1)$ reflection of YbH_{2+x} I4/mmm. LeBail fit has been marked with a red line, while the positions of Bragg reflections and the difference curve have been plotted at the bottom. $\lambda = 0.3344$ Å.

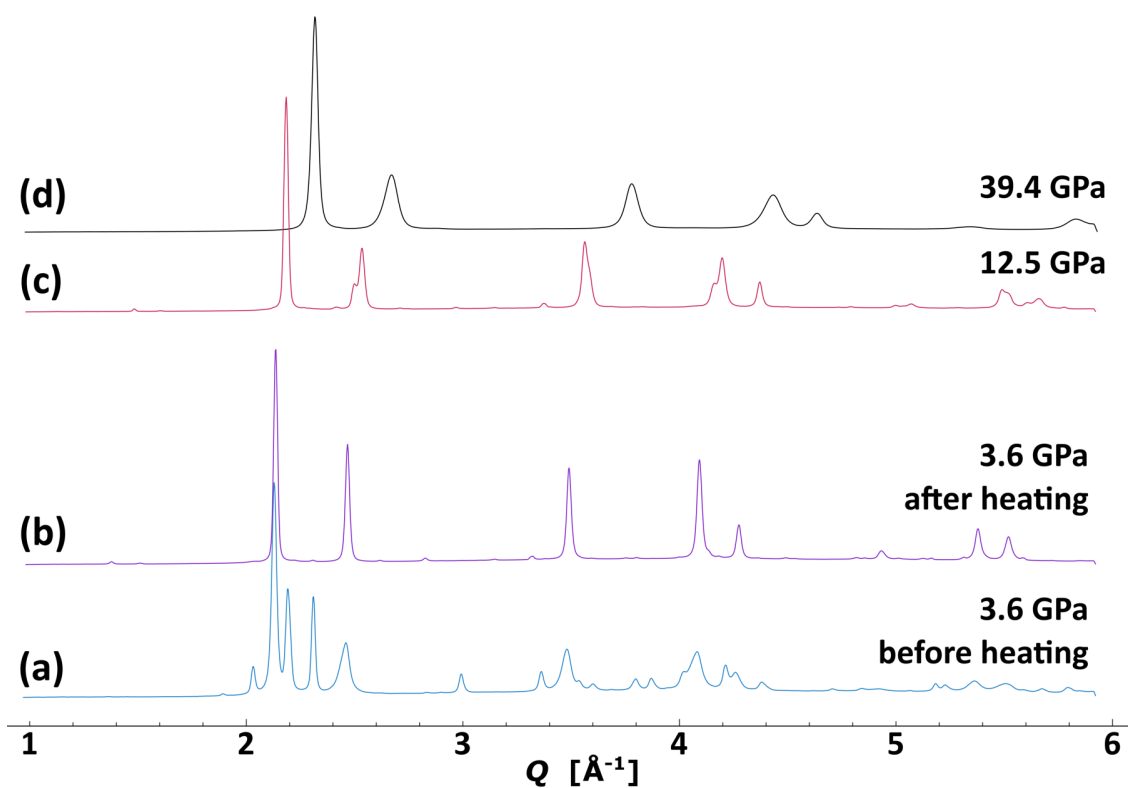
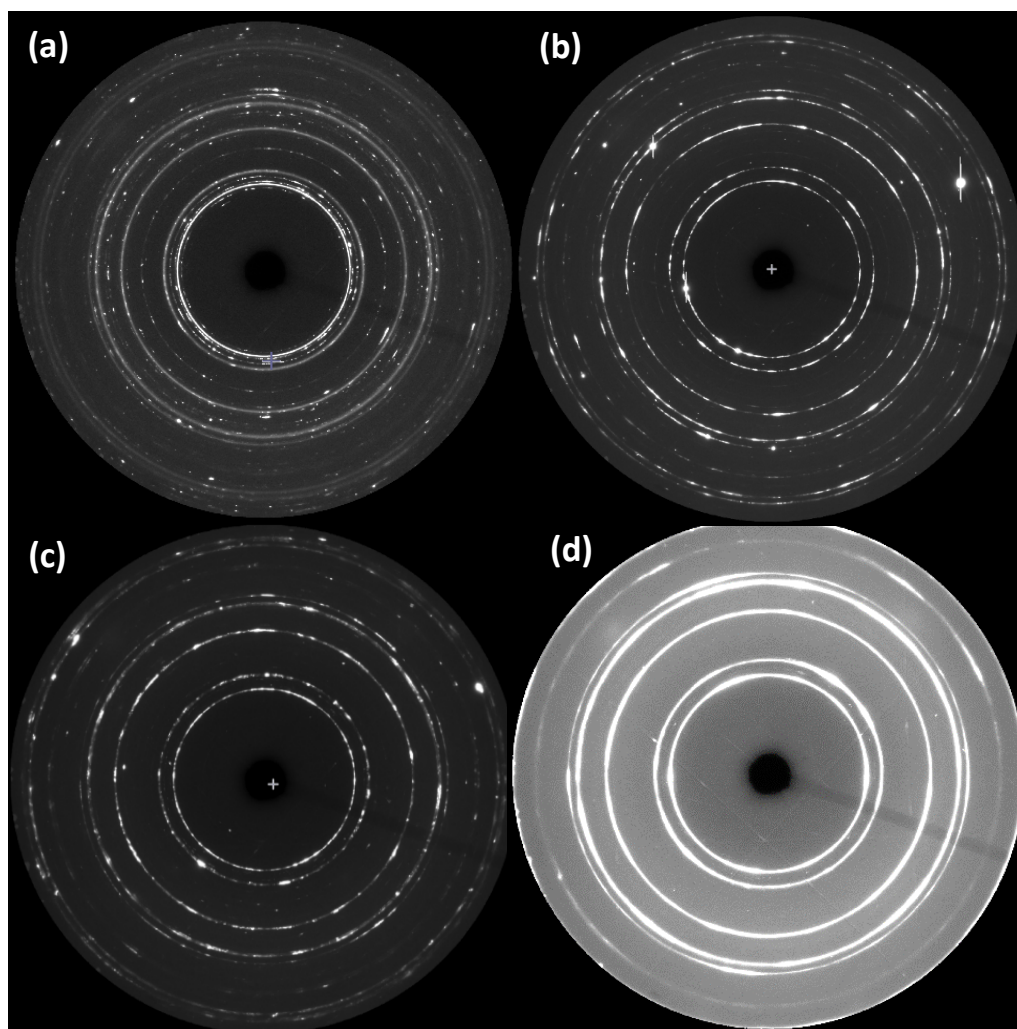


Figure S5. The raw diffraction images for the sample of Yb compressed in H_2 (top), and the corresponding integrated diffraction patterns: (a) before and (b) after the laser heating at ca. 3.6 GPa; (c) after several rounds of laser heating (ca. 12.5 GPa); (d) at ca. 39.4 GPa. Notice the simplification of the pattern (due to disappearance of YbH_2 and Yb phases) and better averaging of the diffraction signals after heating. $\lambda = 0.3344 \text{ \AA}$.

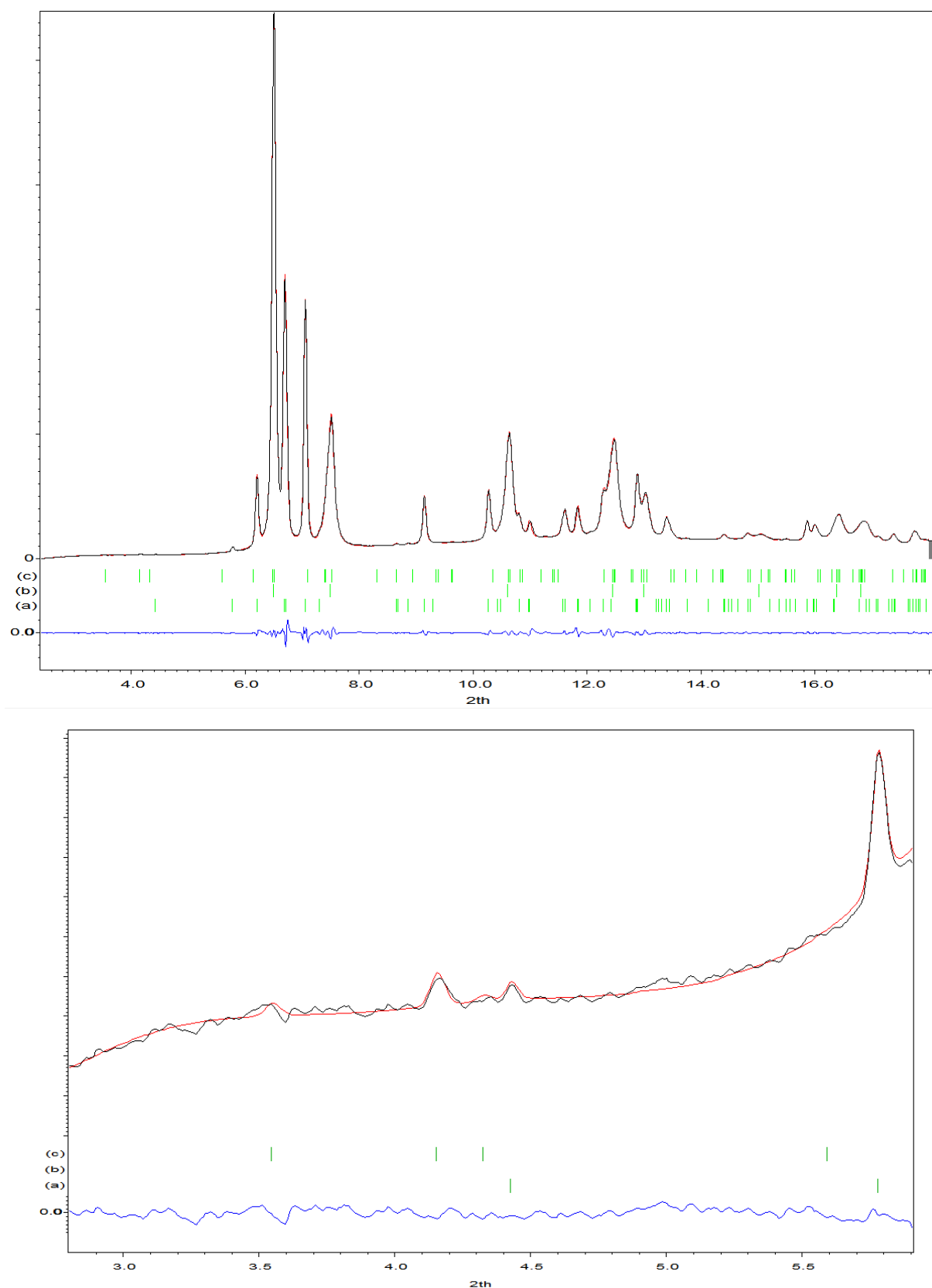


Figure S6. The diffraction data for the products of the reaction between Yb and H_2 before the system was heated. $p = 3.6$ GPa, (a) – YbH_2 $Pnma$, (b) – Yb $Fm-3m$, (c) – YbH_{2+x} $P-31m$. LeBail fit has been marked with a red line, while the positions of Bragg reflections and the difference curve have been plotted at the bottom. The low-angle region has been shown at the bottom, revealing i.a. a weak (1 0 1) reflection of the YbH_{2+x} $P-31m$ phase (ca. 4.15°). $\lambda = 0.3344$ Å.

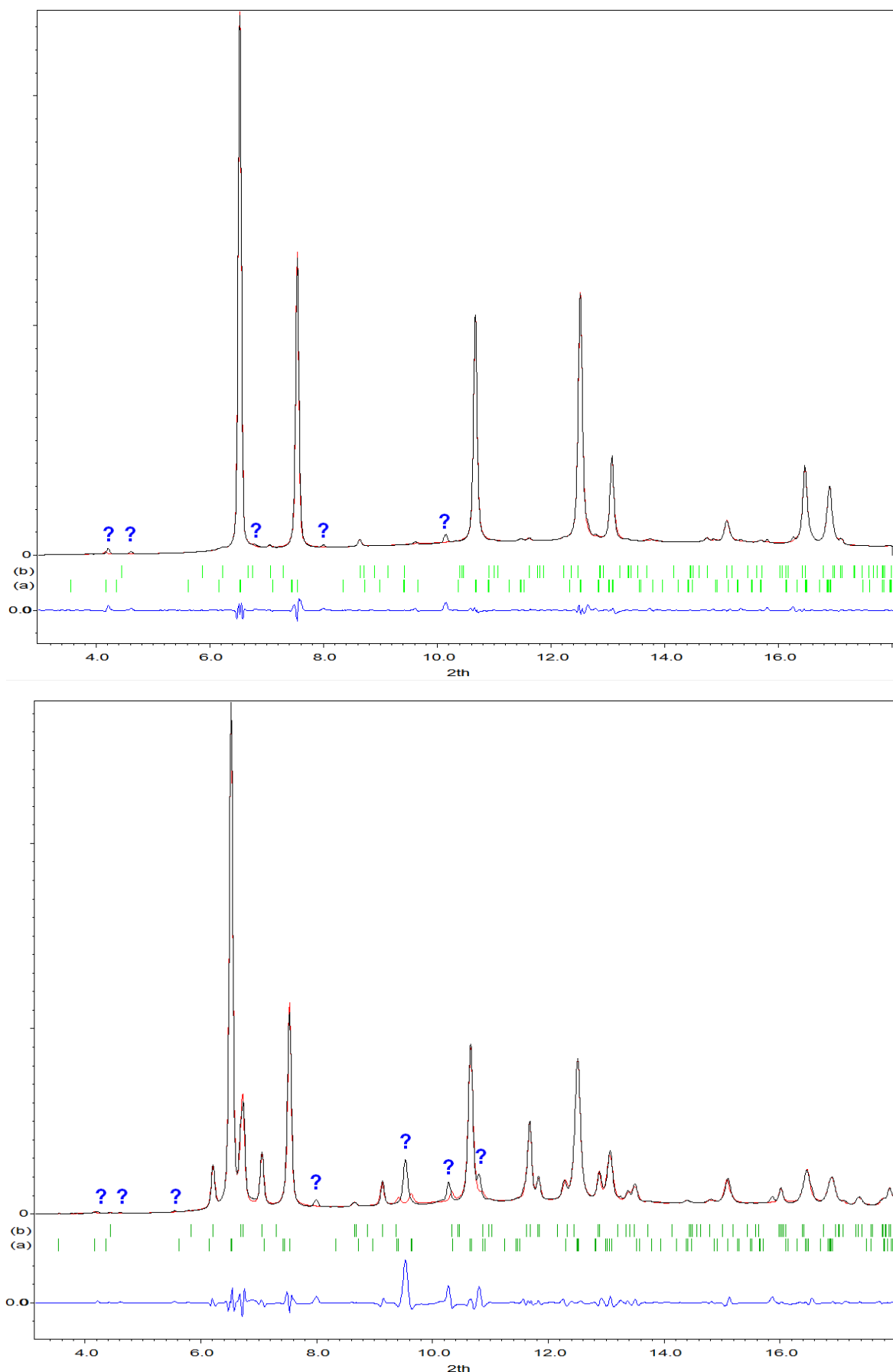


Figure S7. The diffraction data for the products of the reaction between Yb and H_2 after laser heating at ca. 3.6 GPa, as measured in the two areas of the sample (the top and the bottom plots): (a) – YbH_{2+x} P-31m, (b) – YbH_2 Pnma. LeBail fit has been marked with a red line, while the positions of Bragg reflections and the difference curve have been plotted at the bottom. The signals from the unidentified phase(s) have been marked with a “?”. $\lambda = 0.3344 \text{ \AA}$. Note the variable contribution of the crystalline phases across the sample.

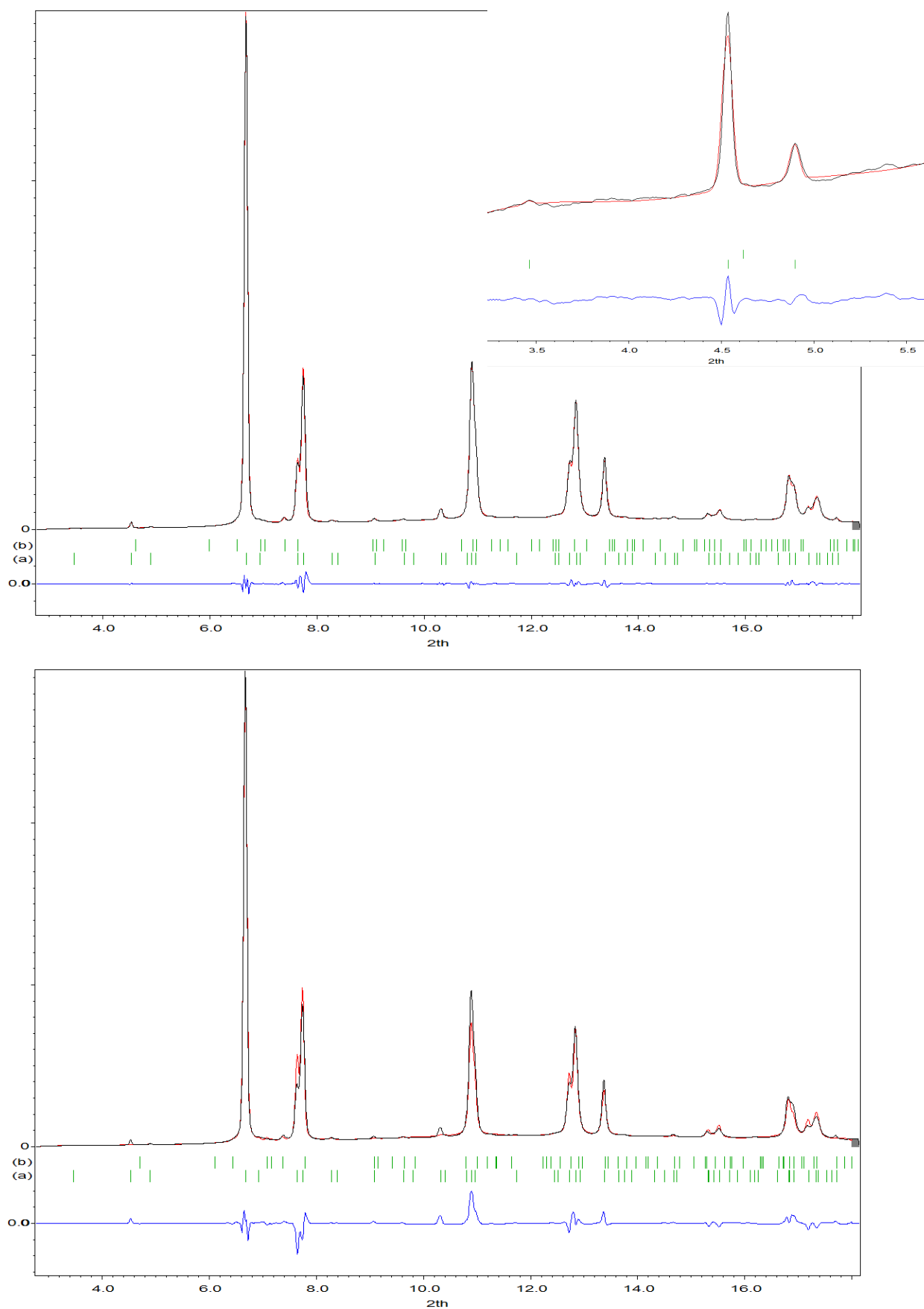


Figure S8. The diffraction data for the products of the reaction between Yb and H_2 after several cycles of laser heating, compressed to ca. 12.5 GPa. Top – LeBail fit, bottom – **Rietveld** fit with no correction for the preferred orientation: (a) – YbH_{2+x} $P4/m$, (b) – YbH_2 $Pnma$. The fit has been marked with a red line, while the positions of Bragg reflections and the difference curve have been plotted at the bottom. $\lambda = 0.3344 \text{ \AA}$.

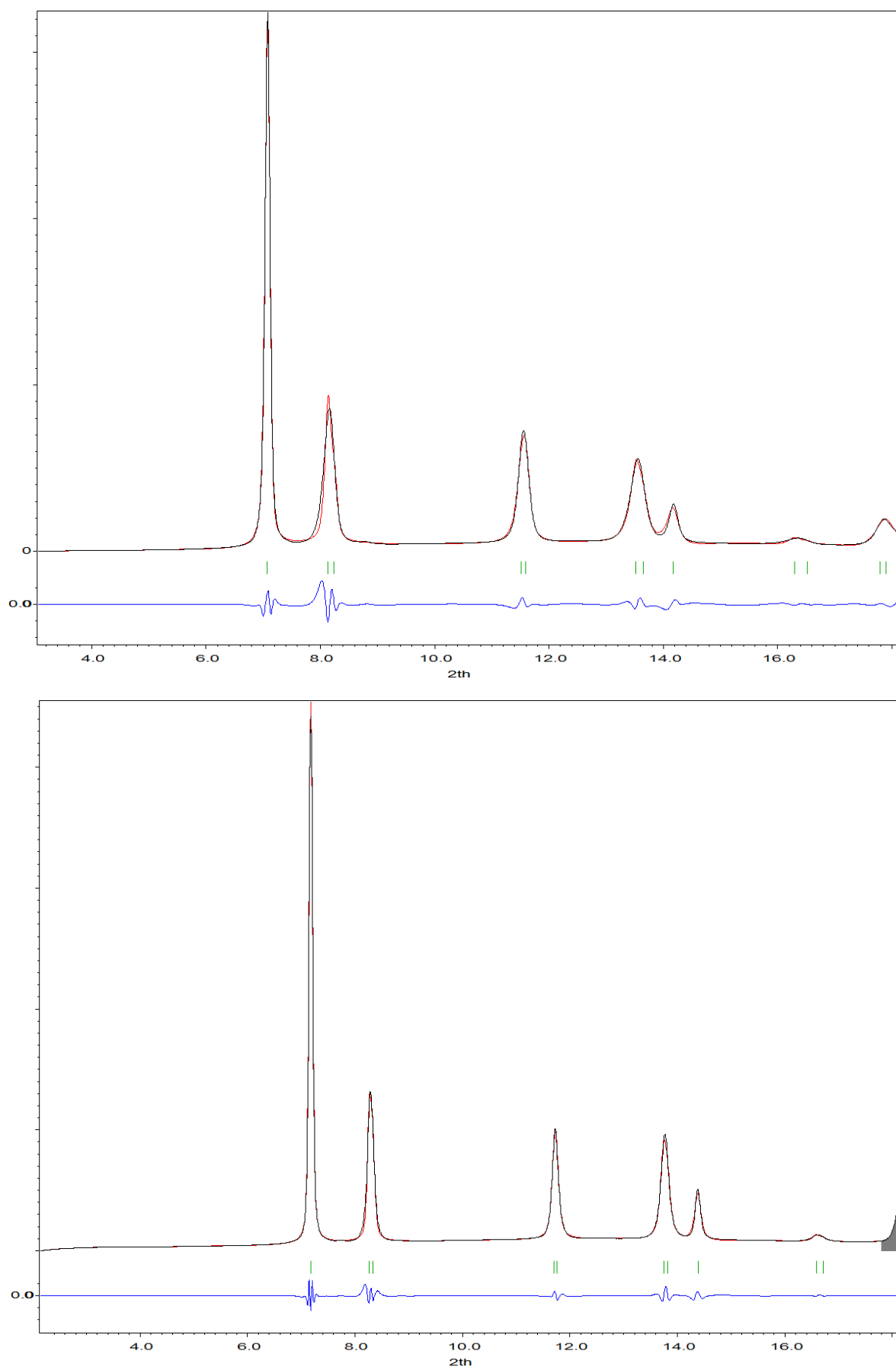


Figure S9. The diffraction data for the products of the reaction between Yb and H_2 after several cycles of laser heating, compressed to ca. 39.4 GPa, as measured in the two areas of the sample: $YbH_{2+x} P4/mmm$. The LeBail fit has been marked with a red line, while the positions of Bragg reflections and the difference curve have been plotted at the bottom. $\lambda = 0.3344$

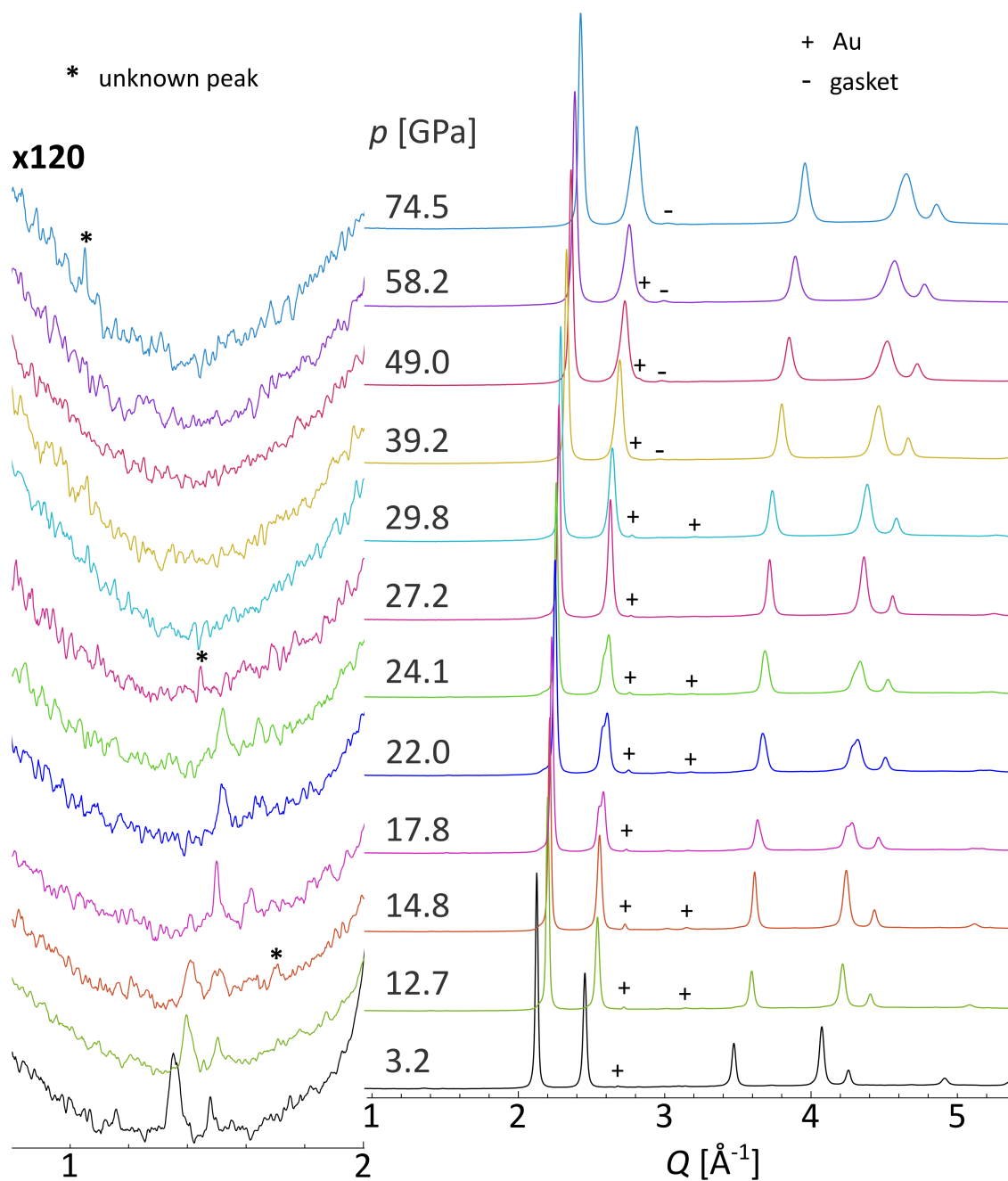


Figure S10. The integrated diffraction data for Yb_3H_8 compressed in H_2 (right) with the expanded low- Q region (left). $\lambda = 0.4066 \text{ \AA}$.

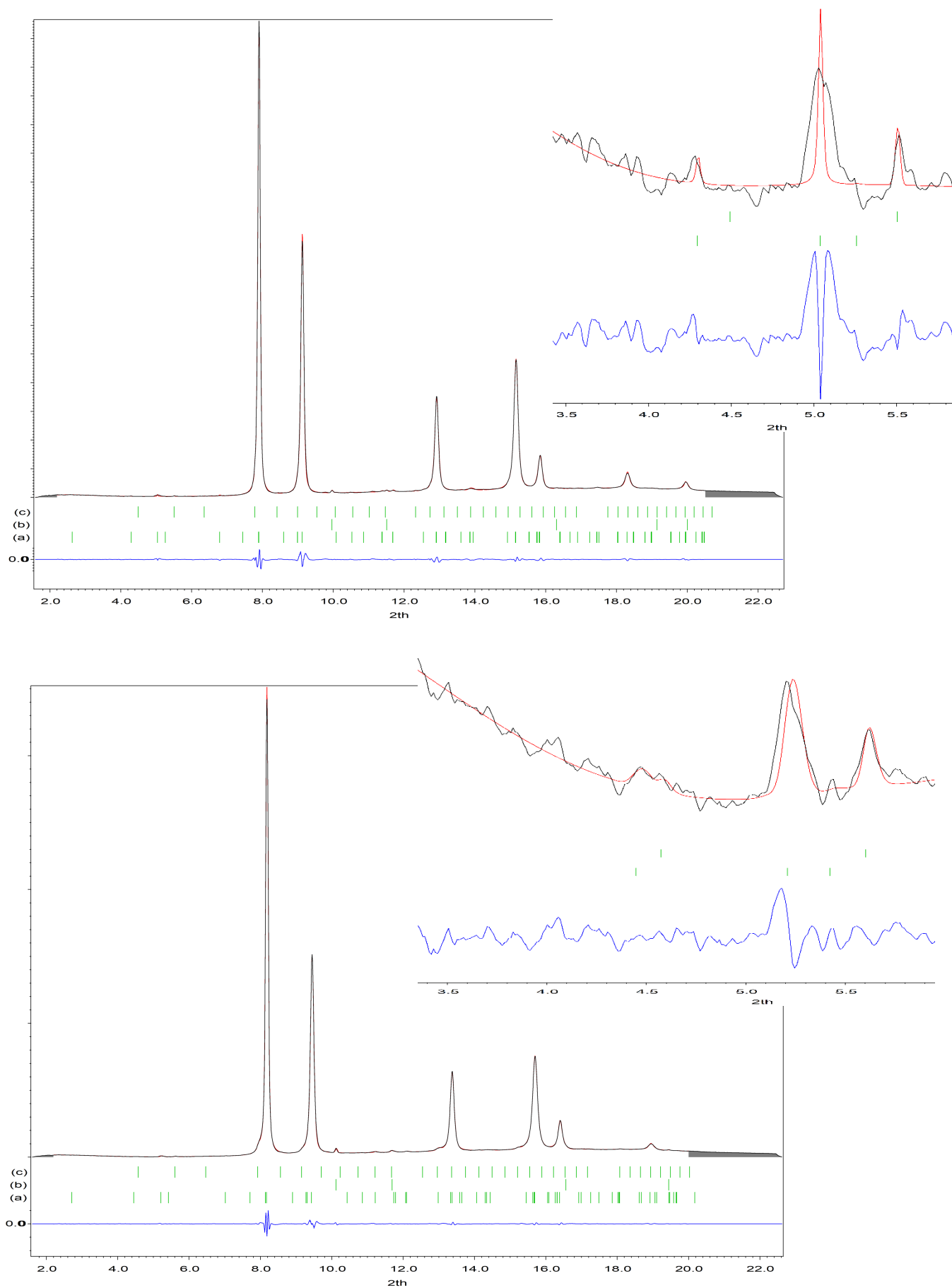


Figure S11. The diffraction data for Yb_3H_8 compressed in H_2 . $p = 3.6$ GPa (top) and 12.7 GPa (bottom), (a) – YbH_{2+x} P -31m, (b) – Au Fm-3m , (c) – Yb_2O_3 Ia-3 . LeBail fit has been marked with a red line, while the positions of Bragg reflections and the difference curve have been plotted at the bottom. The low-angle area is shown as an inset. $\lambda = 0.4066$ Å.

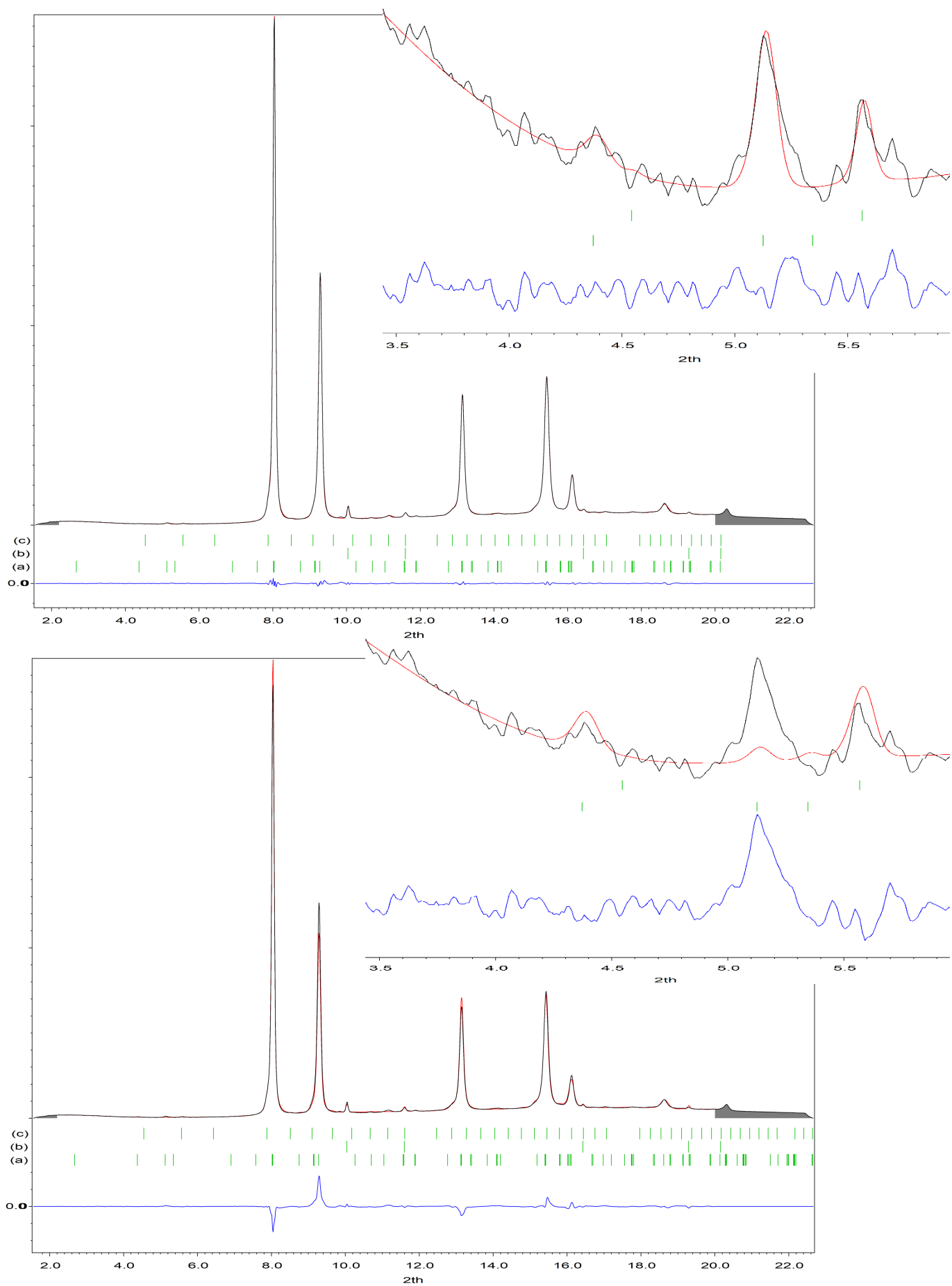


Figure S12. A comparison of the LeBail (top) and **Rietveld** fits (bottom) for Yb_3H_8 compressed in H_2 . $p = 7.9$ GPa, (a) – YbH_{2+x} $P\text{-}31m$, (b) – Au $Fm\text{-}3m$, (c) – Yb_2O_3 $Ia\text{-}3$. LeBail (top plot) and Rietveld (bottom plot) fit have been marked with a red line, while the positions of Bragg reflections and the difference curve have been plotted at the bottom. The low-angle area is shown as an inset. $\lambda = 0.4066$ Å. The relative phase amounts in wt.%: YbH_{2+x} (as Yb_3H_8): 96.6(9); Au : 1.02(16); Yb_2O_3 : 2.9(9). LeBail fit: $wRp = 2.28\%$. Rietveld fit: $wRp = 7.30\%$.

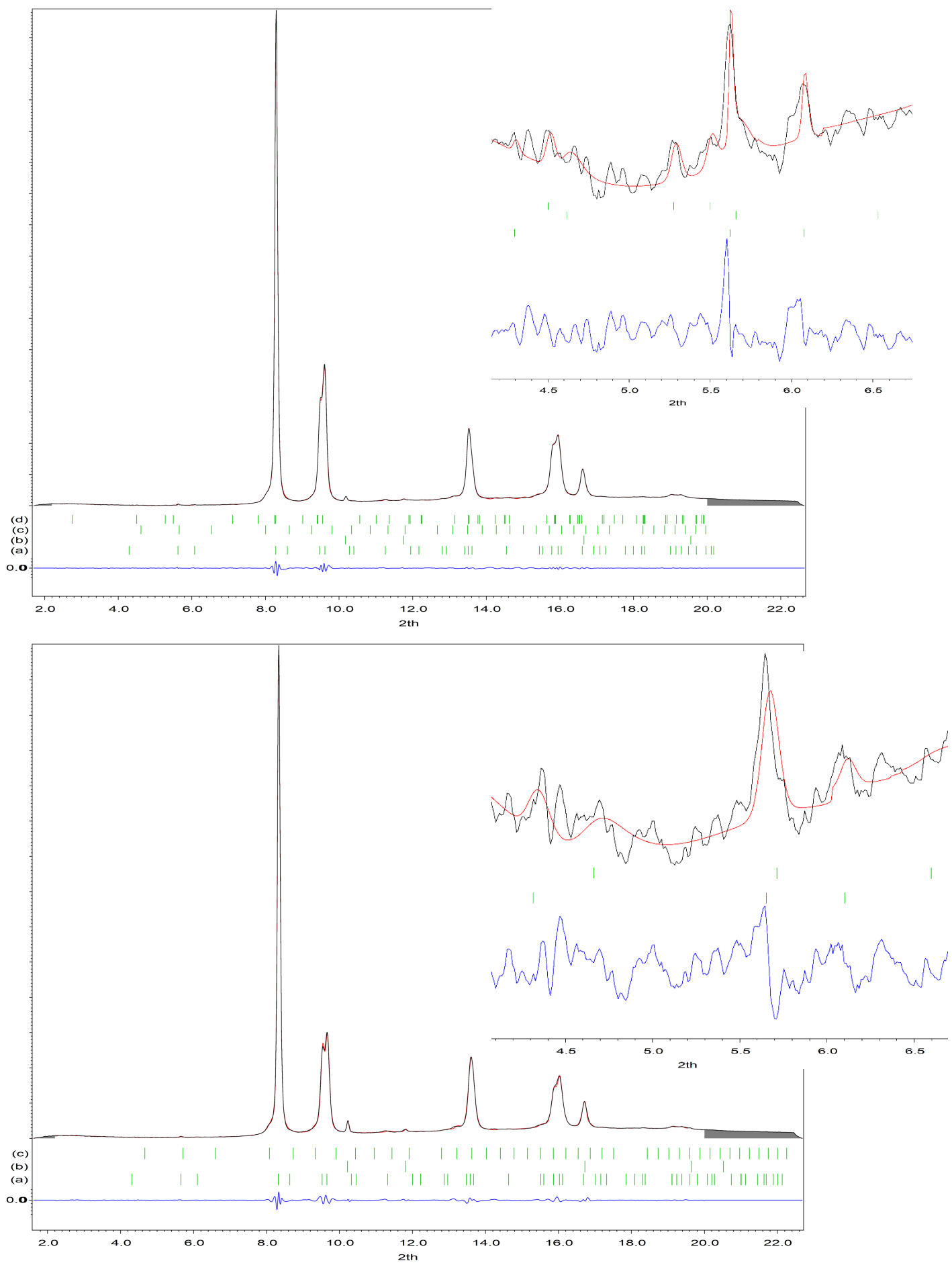


Figure S13. The diffraction data for Yb_3H_8 compressed in H_2 . $p = 17.8$ GPa (top) and 20.8 GPa (bottom), (a) – YbH_{2+x} $I4/m$, (b) – Au $Fm-3m$, (c) – Yb_2O_3 $Ia-3$, (d) – YbH_{2+x} $P-31m$. LeBail fit has been marked with a red line, while the positions of Bragg reflections and the difference curve have been plotted at the bottom. The low-angle area is shown as an inset. $\lambda = 0.4066$ Å.

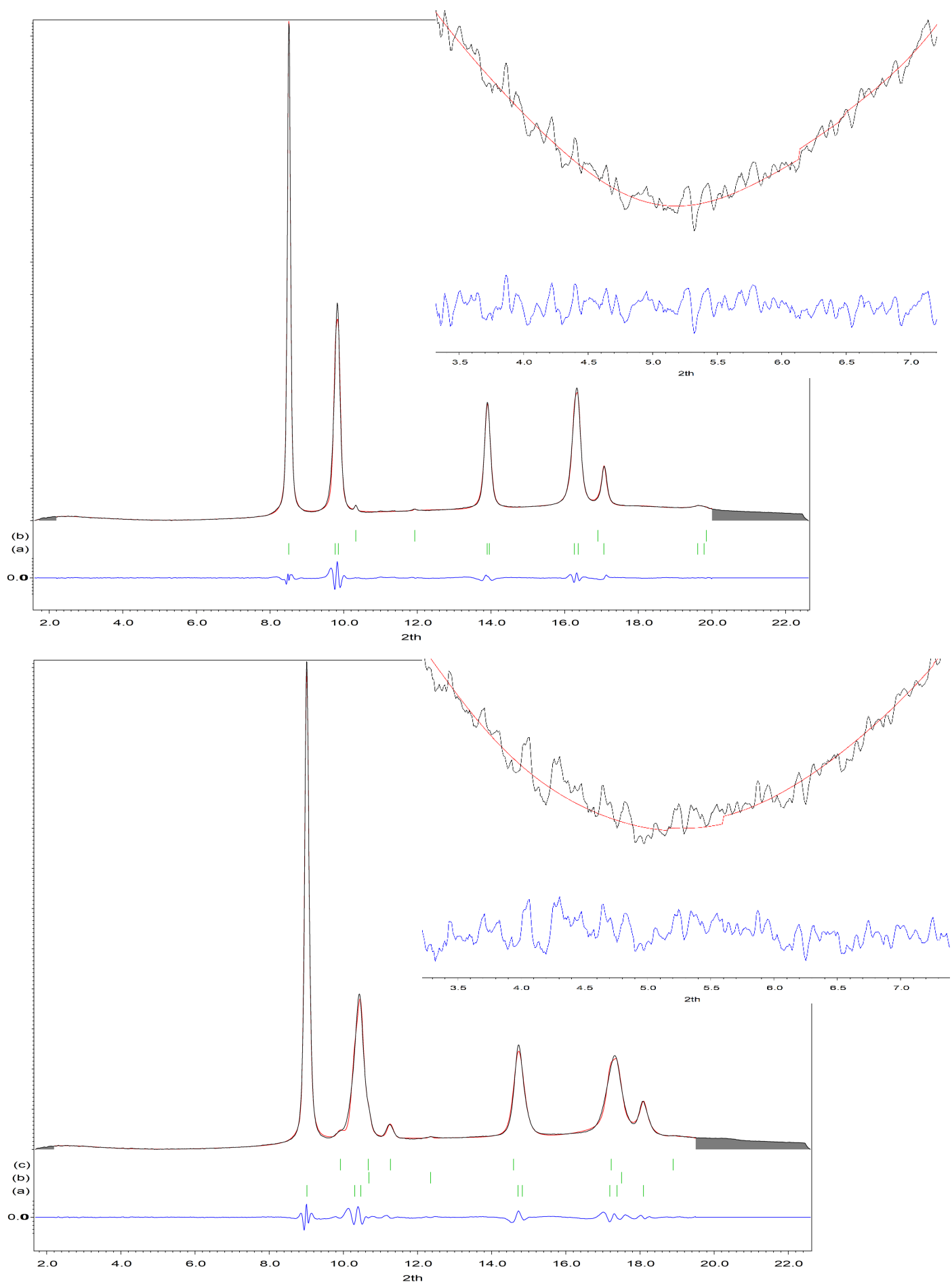


Figure S14. The diffraction data for Yb_3H_8 compressed in H_2 . $p = 29.8$ GPa (top) and 73.5 GPa (bottom), (a) – YbH_{2+x} $I4/mmm$, (b) – Au $Fm-3m$, (c) – Re gasket $P6_3/mmc$. LeBail fit has been marked with a red line, while the positions of Bragg reflections and the difference curve have been plotted at the bottom. The low-angle area is shown as an inset. $\lambda = 0.4066$ Å.

x YbH_x $P\text{-}31m$ (1 0 0)

l YbH_x $I4/m$ (1 0 1)

v Yb_2O_3 $Ia\text{-}3$ (1 1 2)

o YbH_x $P\text{-}31m$ (1 0 1)

/ YbH_x $I4/m$ (2 0 0)

Ne $Fm\text{-}3m$

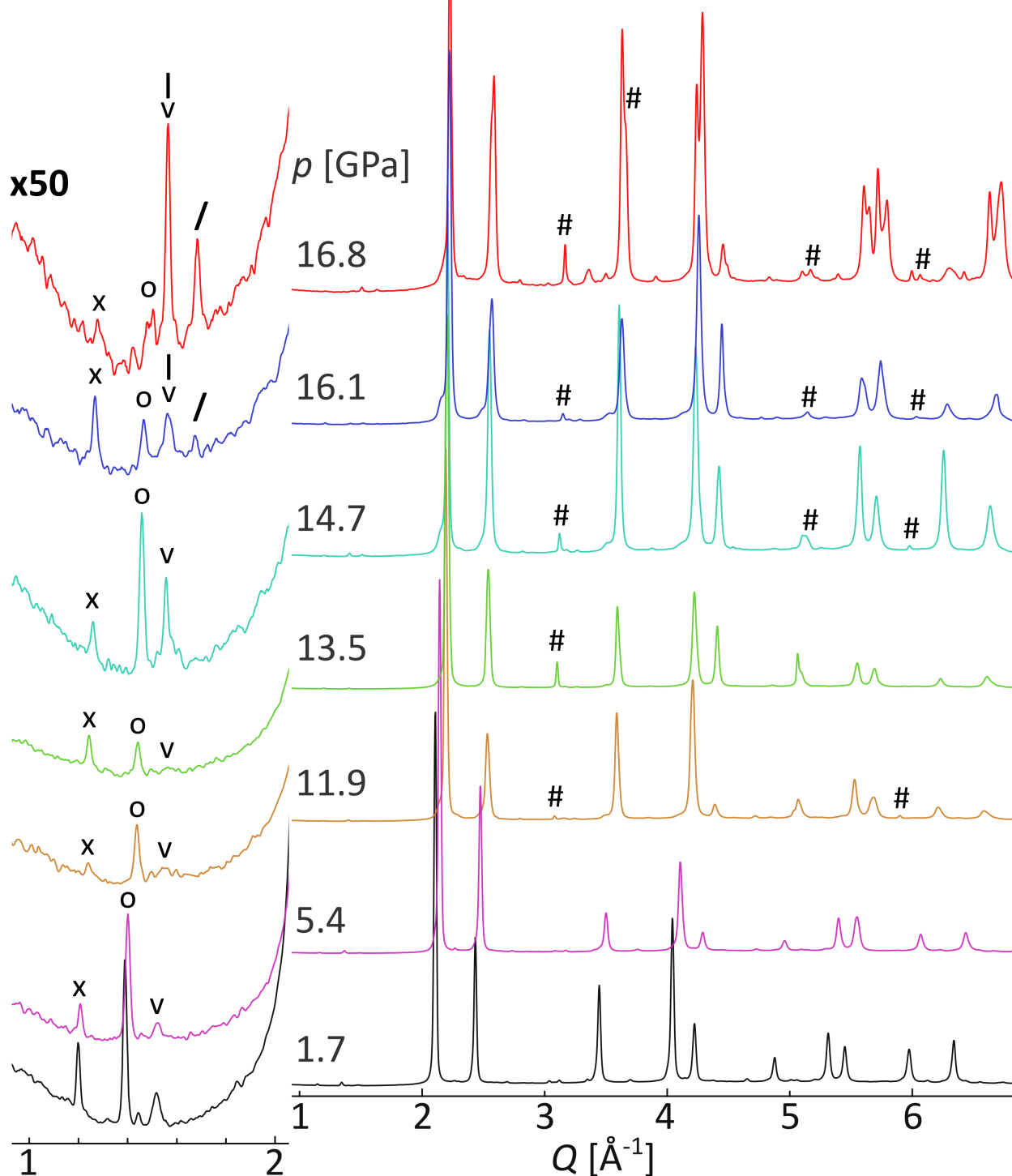


Figure S15. The integrated diffraction data for Yb_3H_8 compressed in Ne (right) with the expanded low- Q region (left). $\lambda = 0.3344 \text{ \AA}$. The most visible reflections of the YbH_{2+x} and Yb_2O_3 phases were marked on the low- Q region.

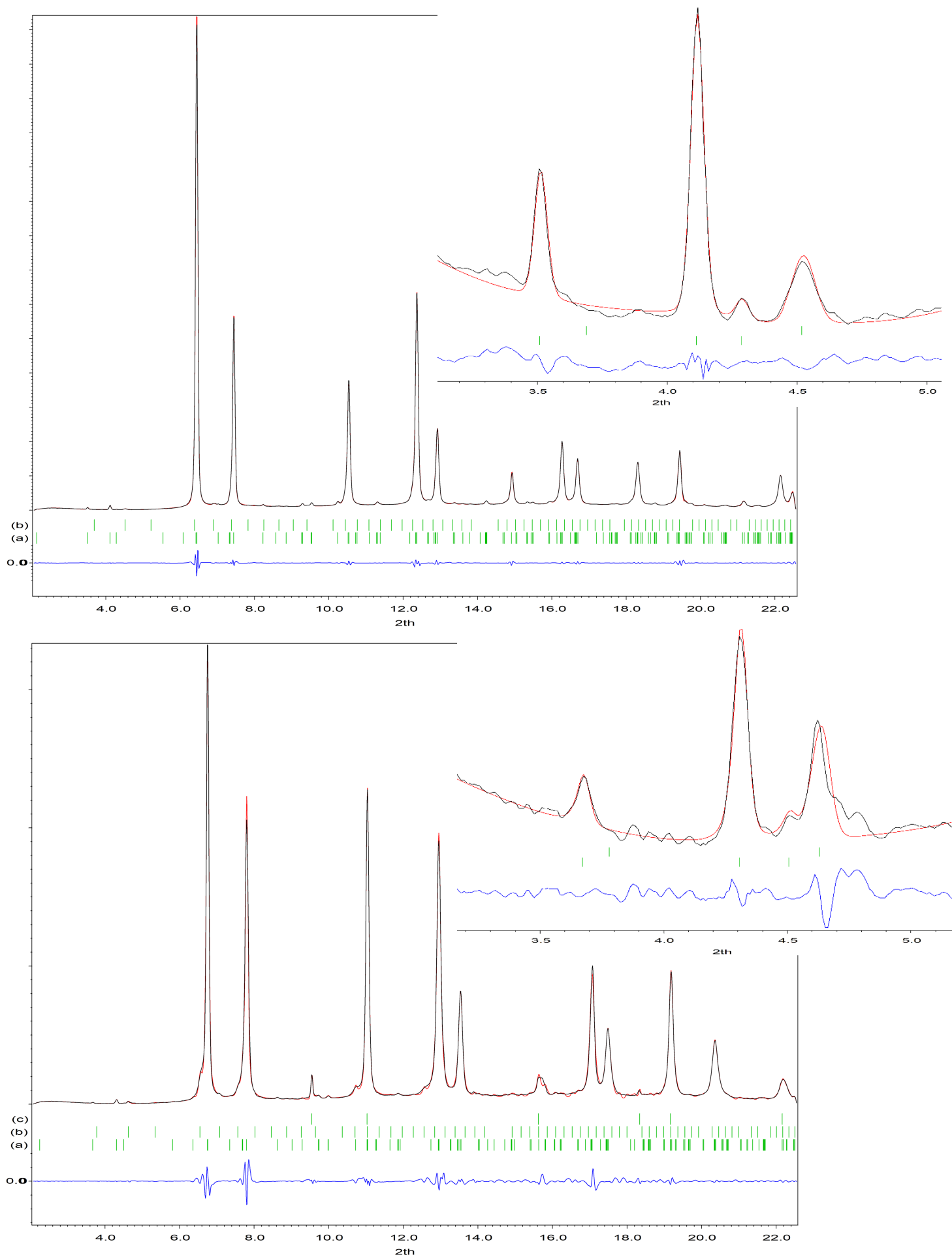


Figure S16. The diffraction data for Yb_3H_8 compressed in Ne. $p = 1.7$ GPa (top) and 14.7 GPa (bottom), (a) – YbH_{2+x} P-31m, (b) – Yb_2O_3 Ia-3, (c) – Ne Fm-3m. LeBail fit has been marked with a red line, while the positions of Bragg reflections and the difference curve have been plotted at the bottom. The low-angle area is shown as an inset. $\lambda = 0.3344$ Å.

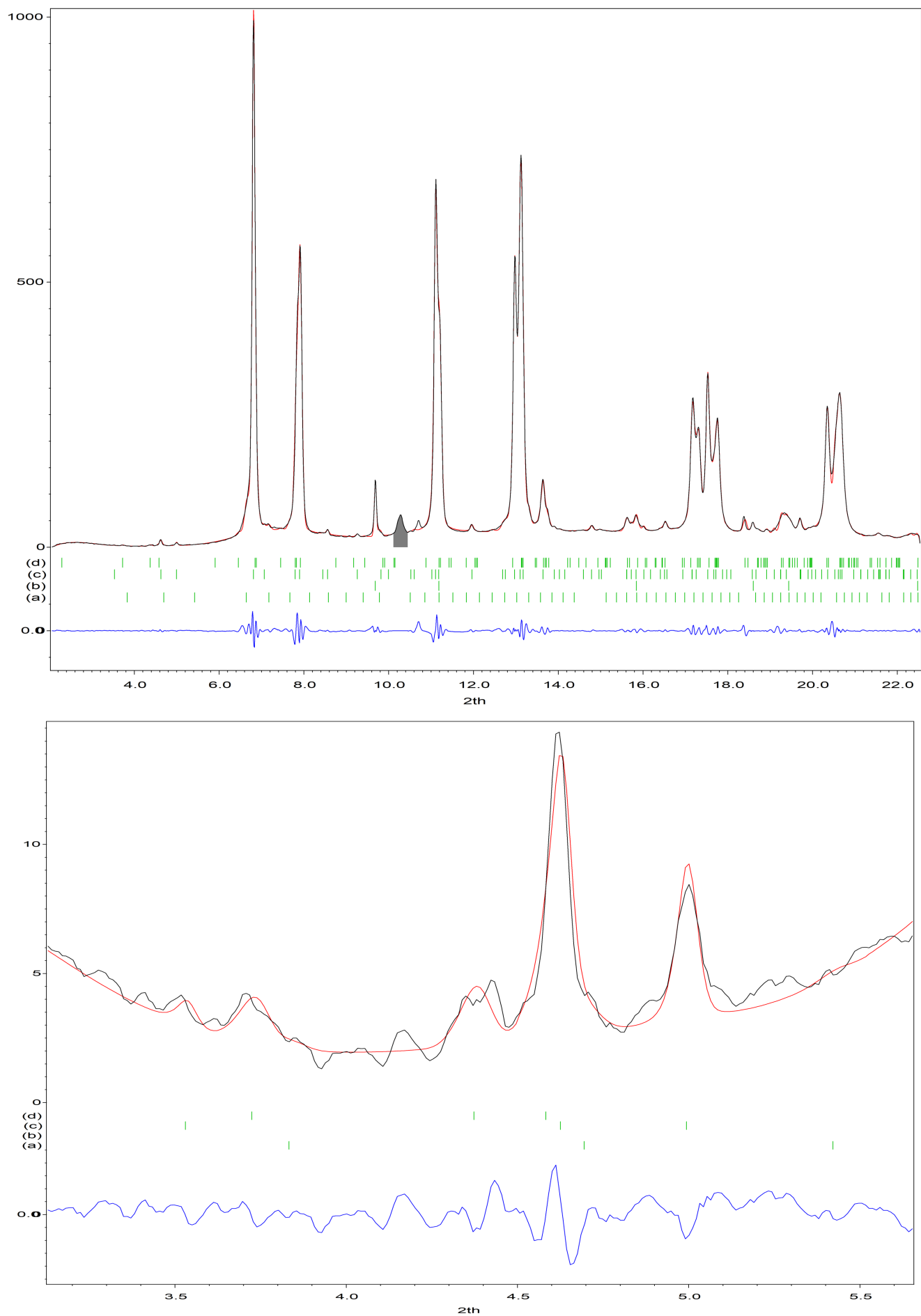


Figure S17. The diffraction data for Yb_3H_8 compressed in Ne. $p = 16.8$ GPa, (a) – Yb_2O_3 $Ia-3$, (b) – Ne $Fm-3m$, (c) – YbH_{2+x} $I4/m$, (d) – YbH_{2+x} $P-31m$. LeBail fit has been marked with a red line, while the positions of Bragg reflections and the difference curve have been plotted at the bottom. The low-angle area is shown at the bottom. $\lambda = 0.3344$ Å.

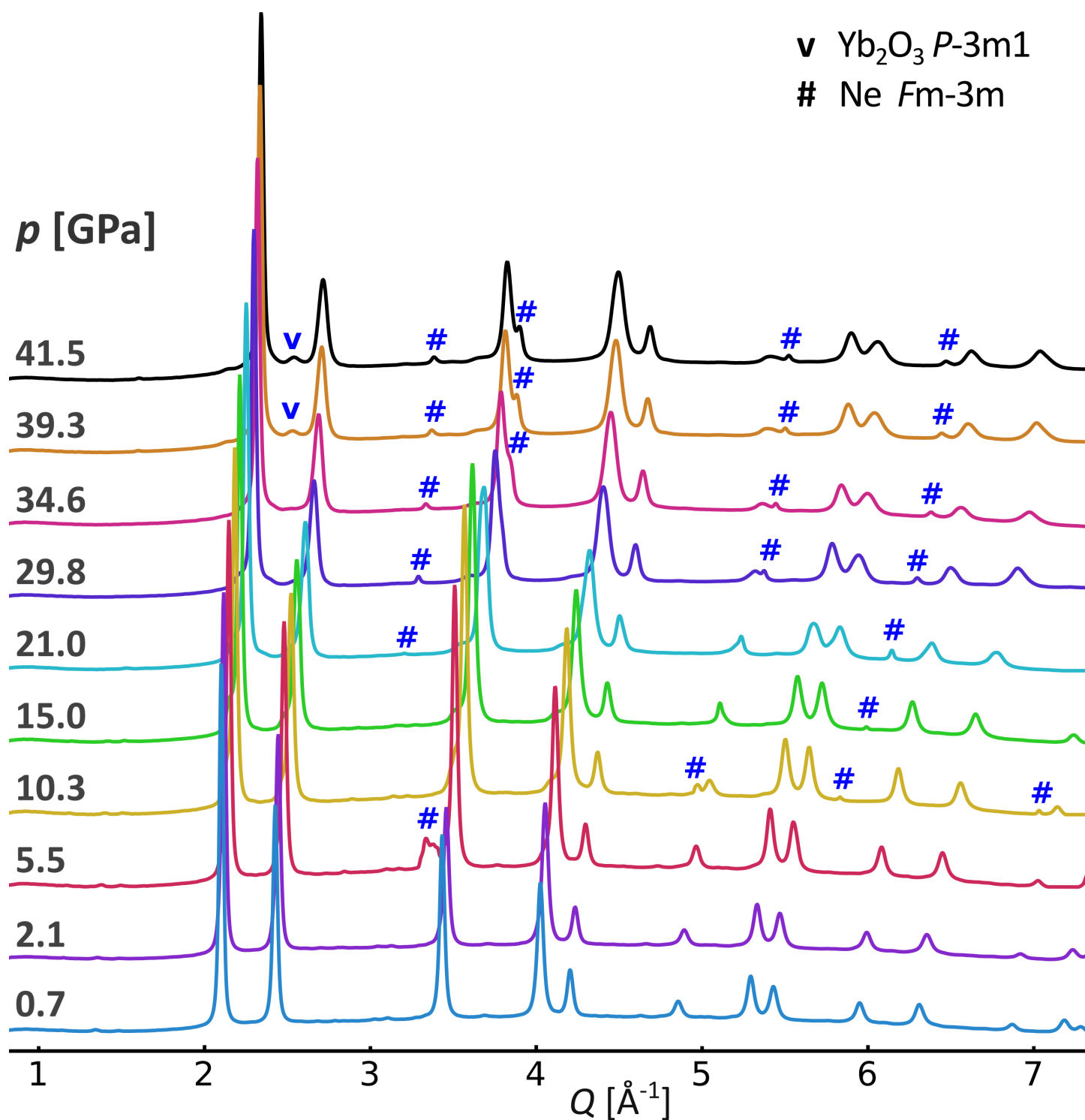


Figure S18. The integrated diffraction data for Yb_3H_8 compressed in Ne. $\lambda = 0.2952 \text{ \AA}$. The most visible reflections of the Yb_2O_3 and Ne phases were marked.

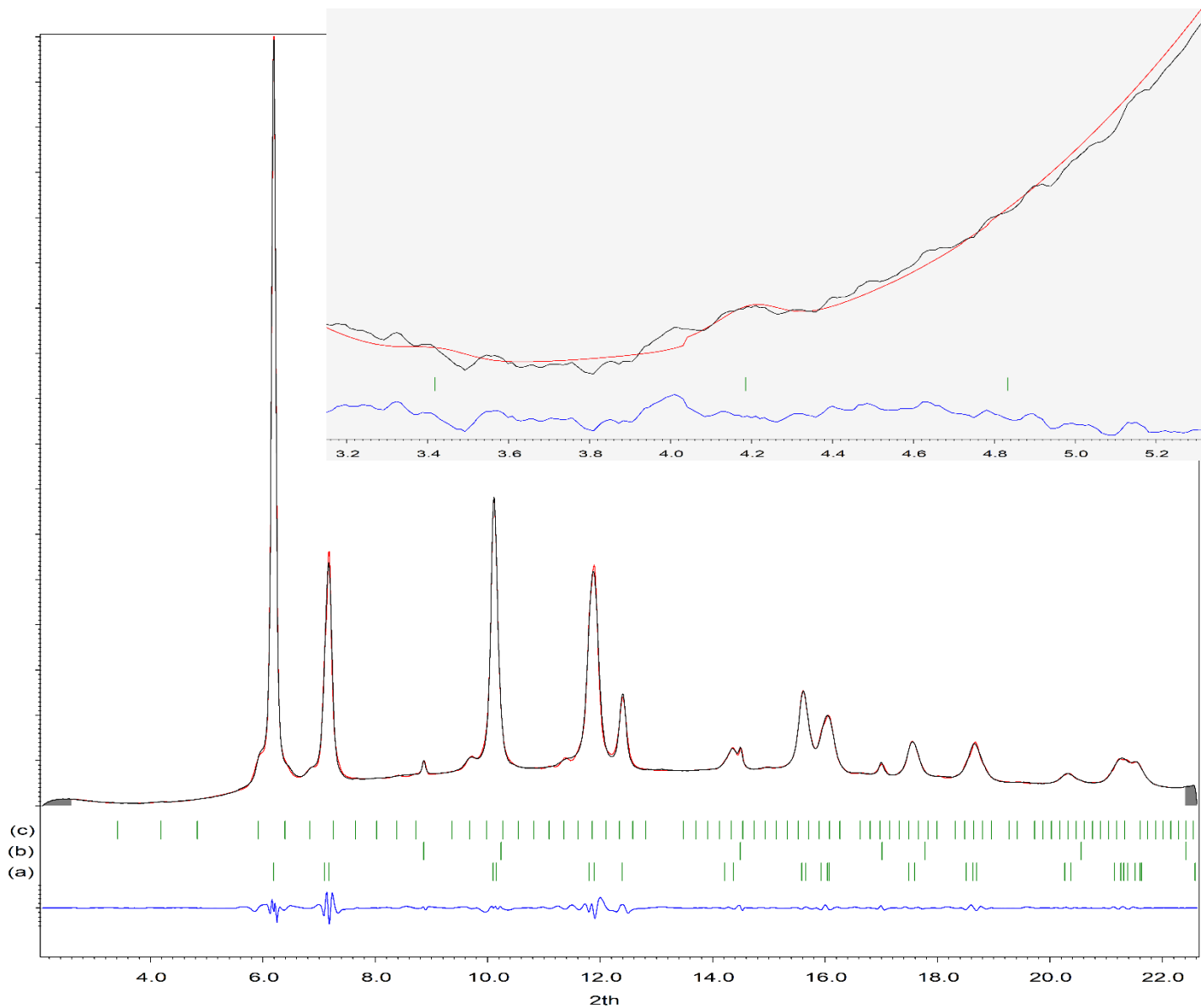


Figure S19. The diffraction data for Yb_3H_8 compressed in Ne. $p = 28.9$ GPa, (a) – YbH_{2+x} $I4/mmm$, (b) – Ne $Fm-3m$, (c) – Yb_2O_3 $Ia-3$. LeBail fit has been marked with a red line, while the positions of Bragg reflections and the difference curve have been plotted at the bottom. The low-angle area is shown as an inset (ca. 80x magnification of the ordinate). $\lambda = 0.2952$ Å.

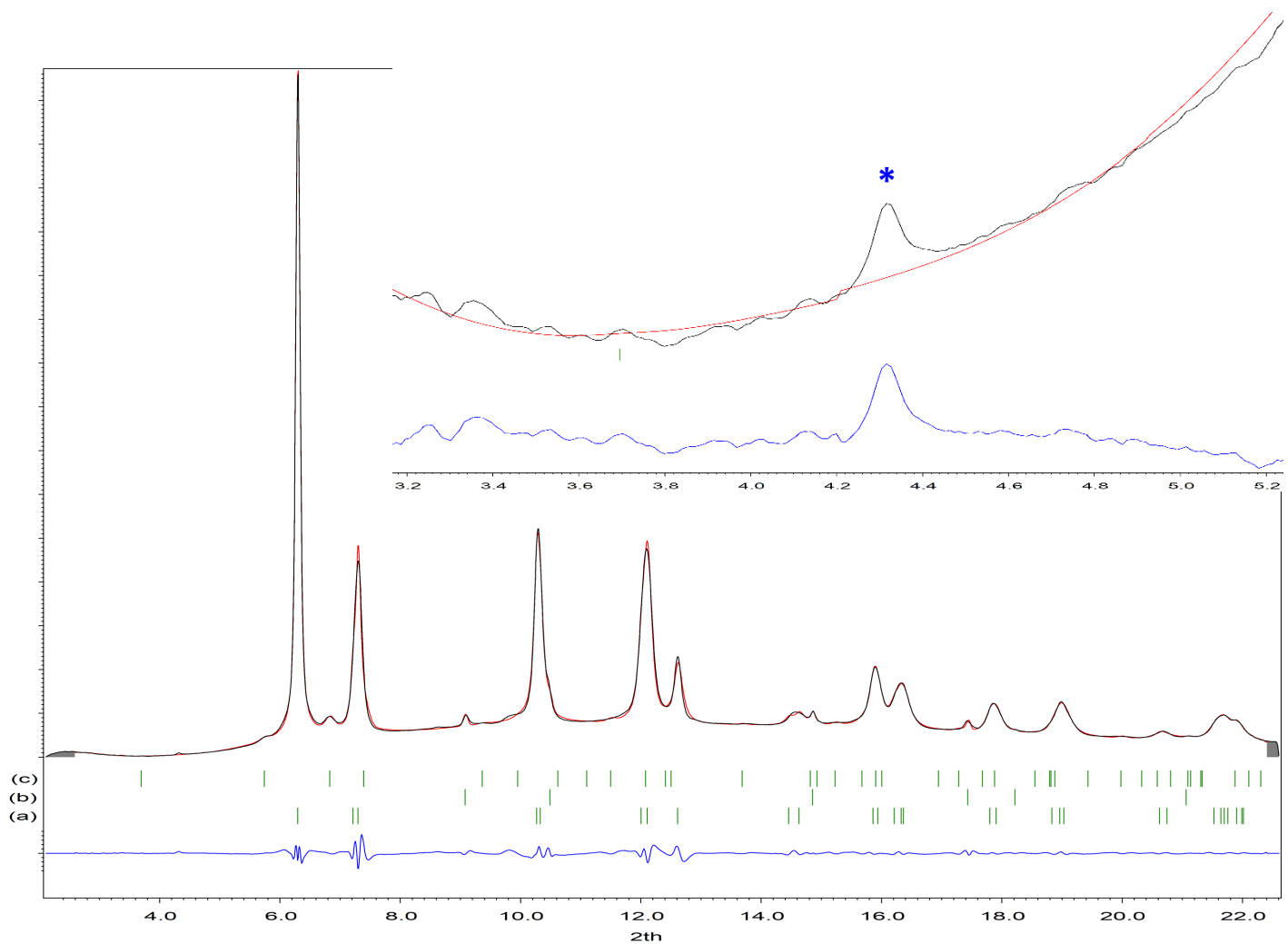


Figure S20. The diffraction data for Yb_3H_8 compressed in Ne. $p = 39.3$ GPa, (a) – YbH_{2+x} $I4/mmm$, (b) – Ne $Fm-3m$, (c) – Yb_2O_3 $P-3m1$; * – unidentified signal. LeBail fit has been marked with a red line, while the positions of Bragg reflections and the difference curve have been plotted at the bottom. The low-angle area is shown as an inset (ca. 80x magnification of the ordinate). $\lambda = 0.2952$ Å.

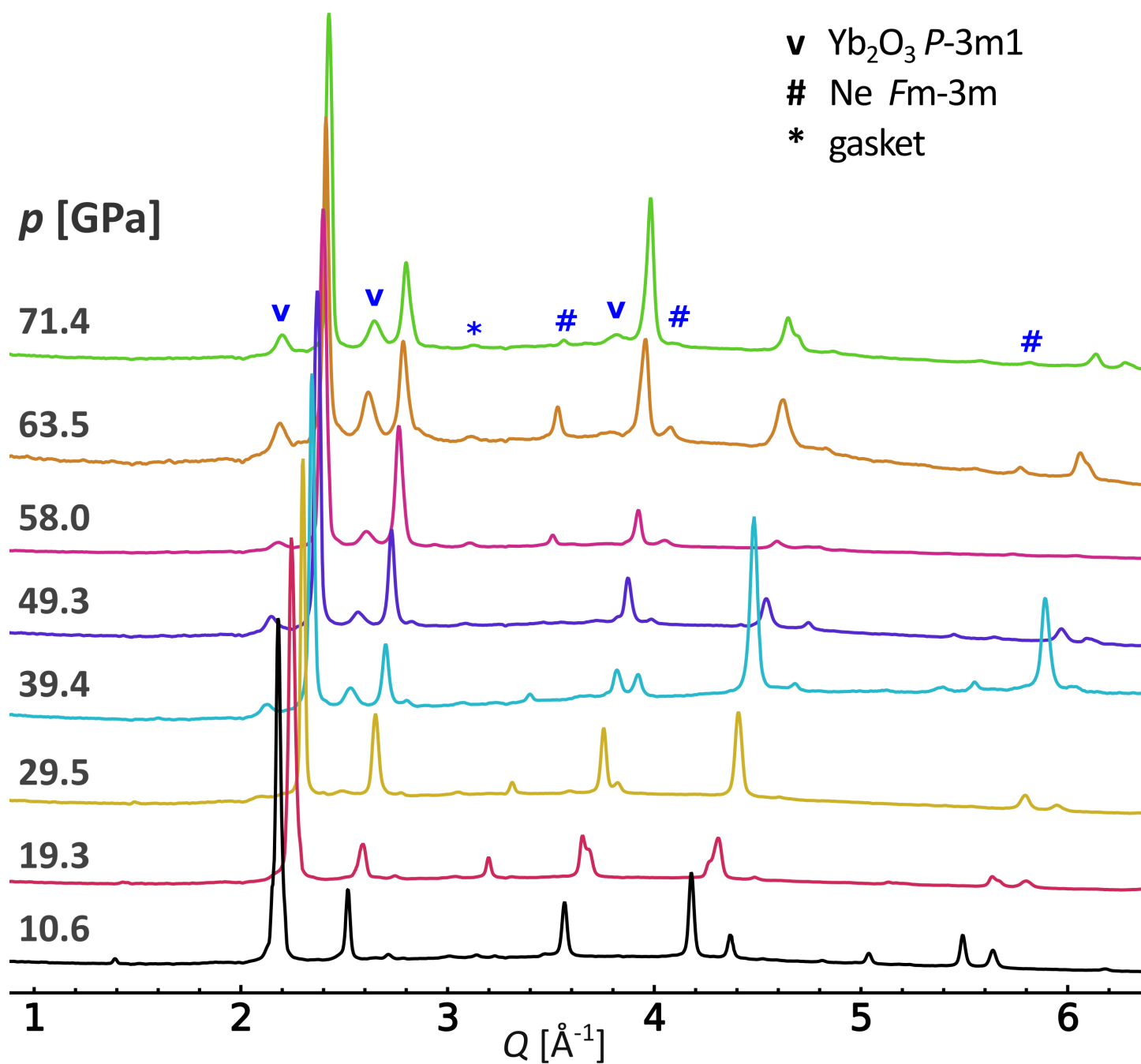


Figure S21. The integrated diffraction data for Yb_3H_8 compressed in Ne. $\lambda = 0.3445 \text{ \AA}$. The most visible reflections of the Yb_2O_3 and Ne phases were marked.

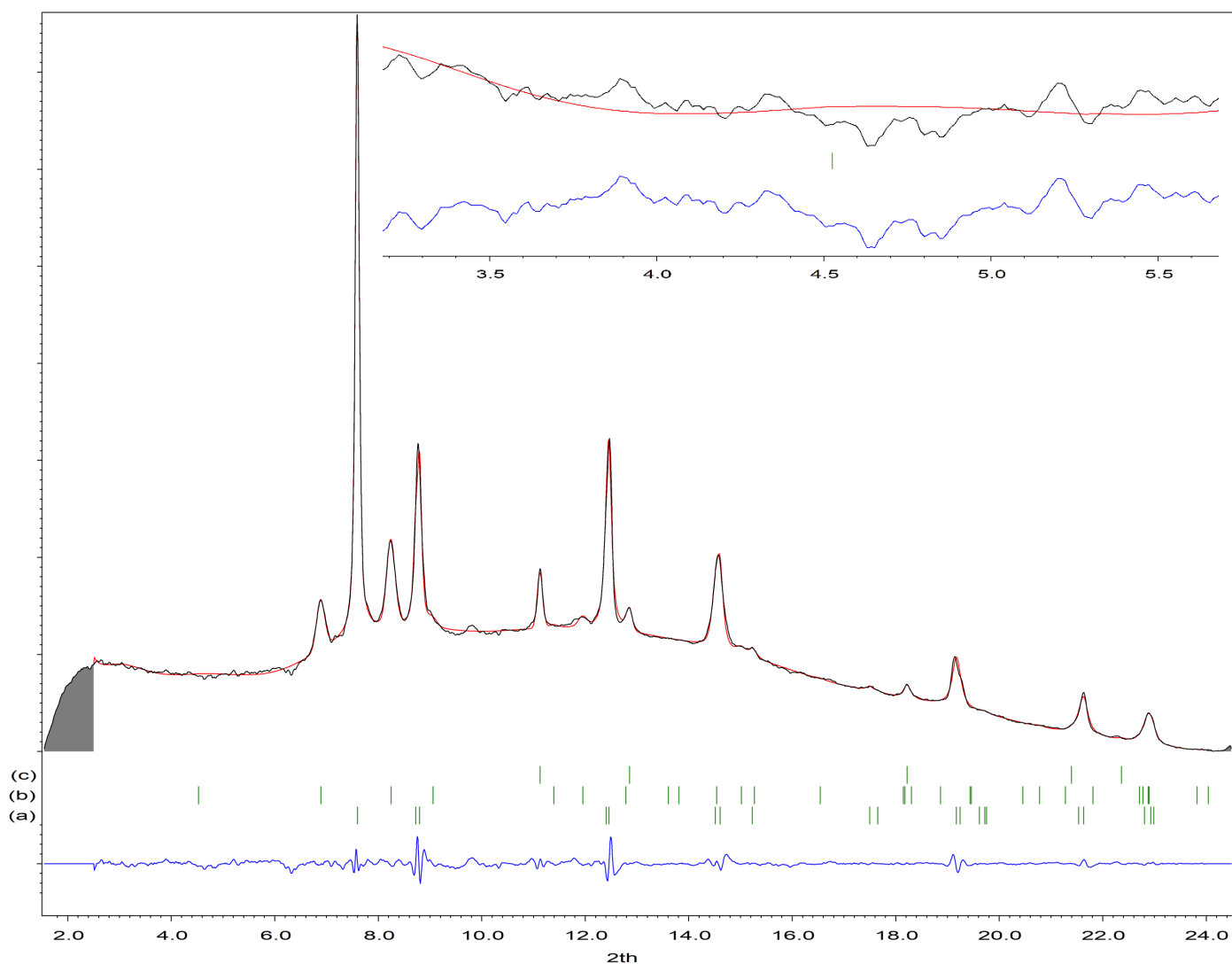


Figure S22. The diffraction data for Yb_3H_8 compressed in Ne. $p = 63.5$ GPa, (a) – YbH_{2+x} $I4/mmm$, (b) – Yb_2O_3 $P-3m1$, (c) – Ne $Fm-3m$. LeBail fit has been marked with a red line, while the positions of Bragg reflections and the difference curve have been plotted at the bottom. The low-angle area is shown as an inset (ca. 80x magnification of the ordinate). $\lambda = 0.3445$ Å.

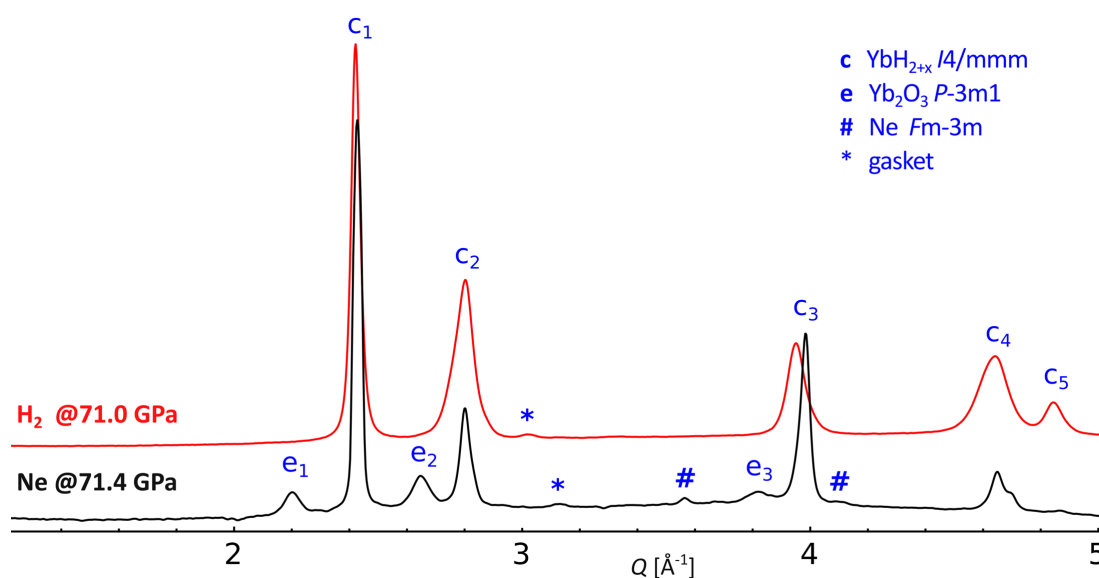
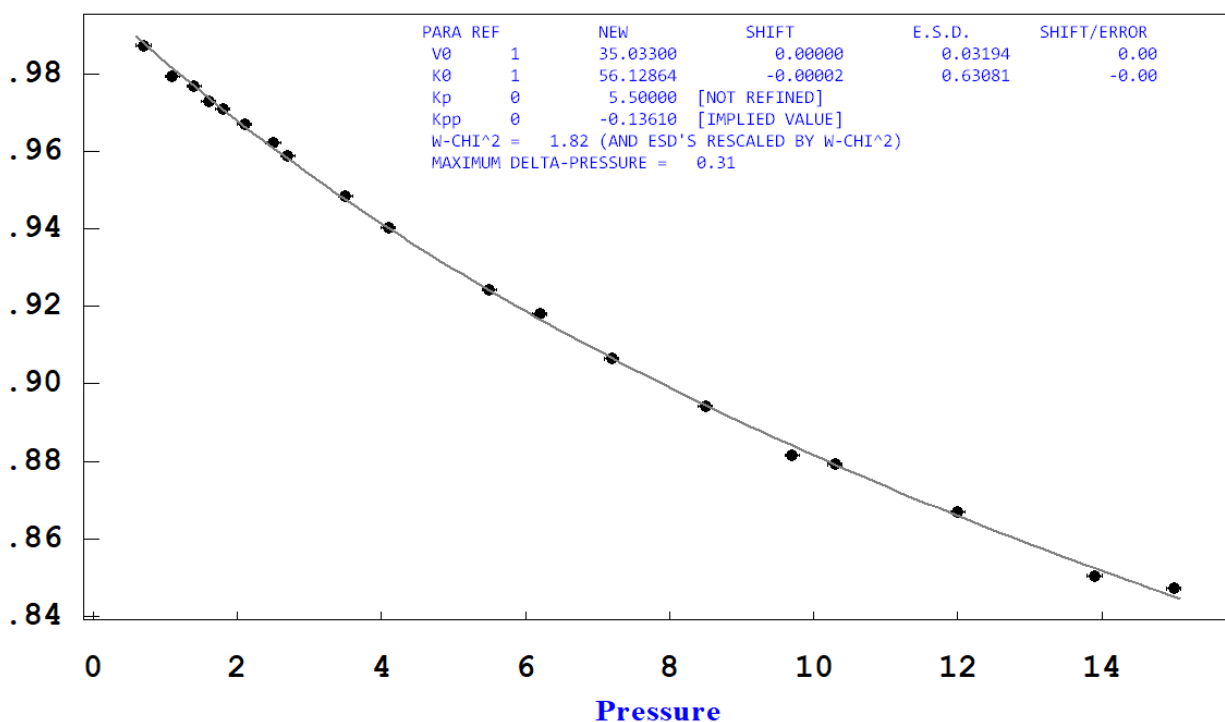


Figure S23. A comparison of the integrated diffraction data for Yb_3H_8 compressed to ca. 71 GPa in Ne and in H_2 . $\lambda = 0.3445$ Å (Ne) and 0.4066 Å (H_2). The most visible reflections of the YbH_{2+x} and Yb_2O_3 phases were marked: c – YbH_{2+x} $I4/mmm$: 1-(1 0 1), 2-(0 0 2) and (1 1 0), 3-(1 1 2) and (2 0 0), 4-(1 0 3) and (2 1 1), 5-(2 0 2); e – Yb_2O_3 $P-3m1$: 1-(1 0 0), 2-(1 0 1), 3-(2 -1 0).

V/V_0



Normalized Pressure (F)

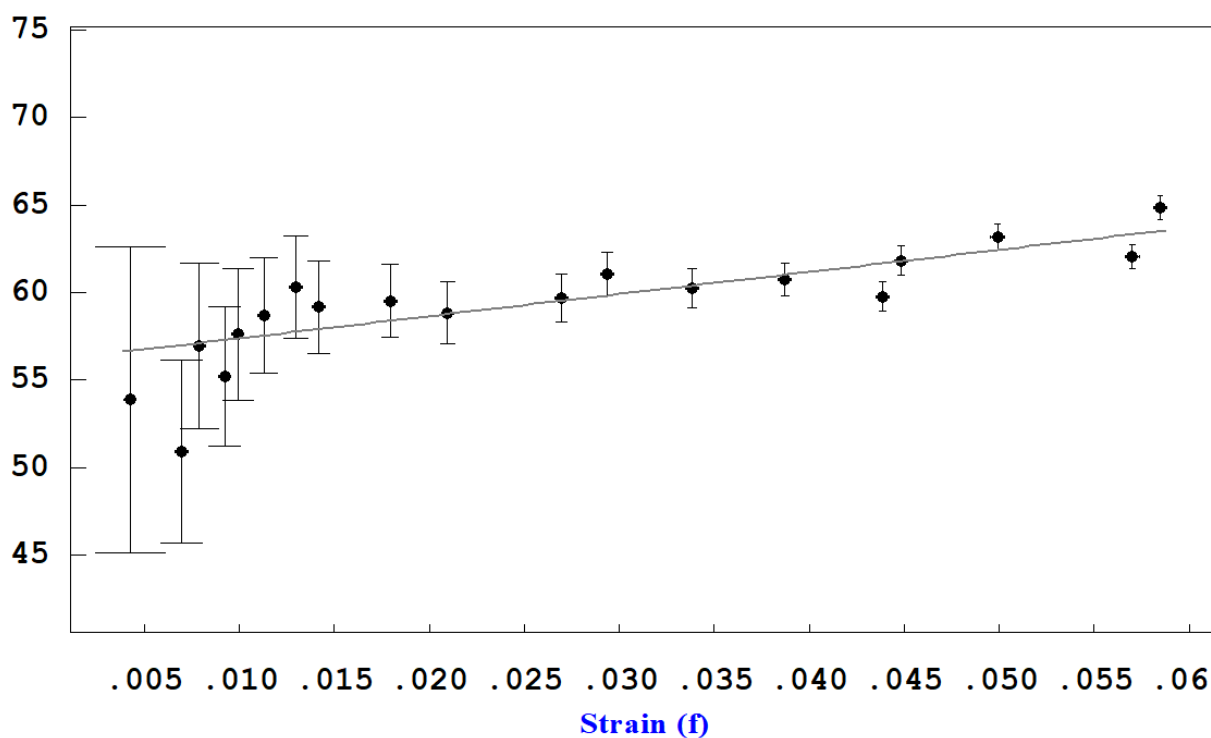
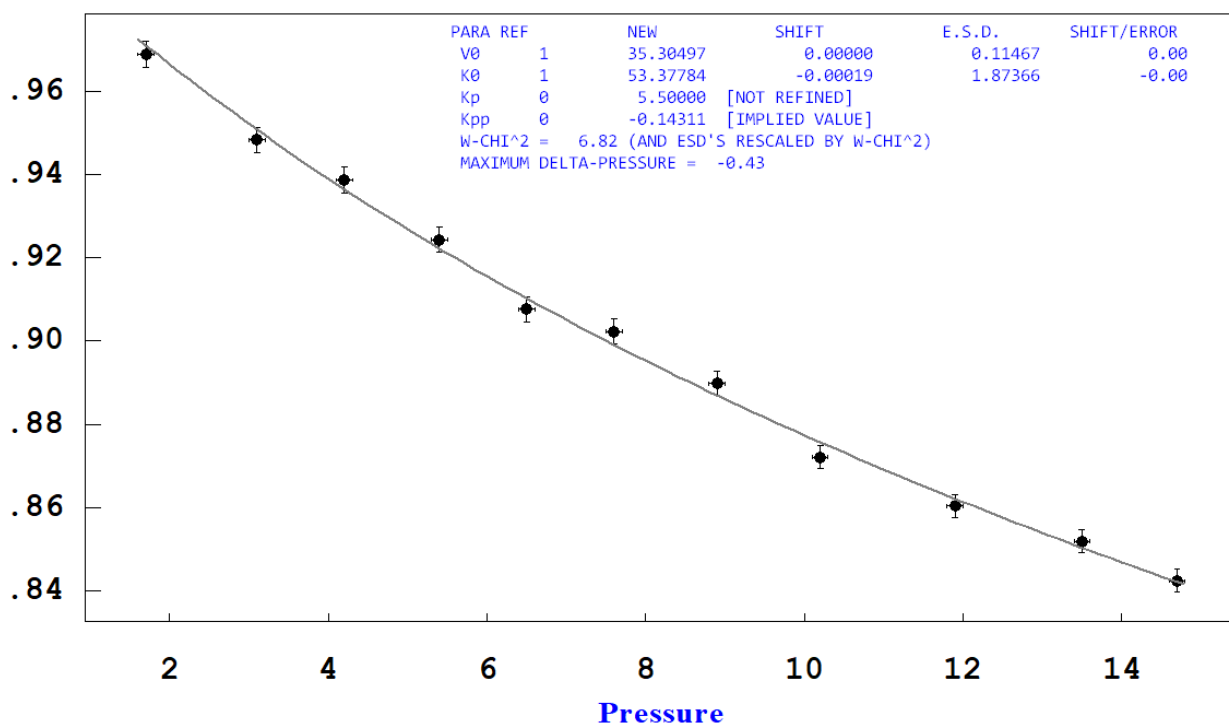


Figure S24. The fit of the volume per Yb atom to the third-order Birch-Murnaghan equation of state for P-31m phase of Yb_3H_8 compressed in Ne PTM (top) and the F - f plot (bottom). F – normalized pressure [GPa], f – Eulerian strain; $F = P/3f(1+2f)^{5/2}$, $f = [(V_0/V)^{2/3} - 1]/2$, $F = K_0 + [3K_0(K' - 4)/2]f$. The experimental data reveal the positive slope of the F - f plot, indicating $K' > 4$.¹ Run (g).

V/V₀



Normalized Pressure (F)

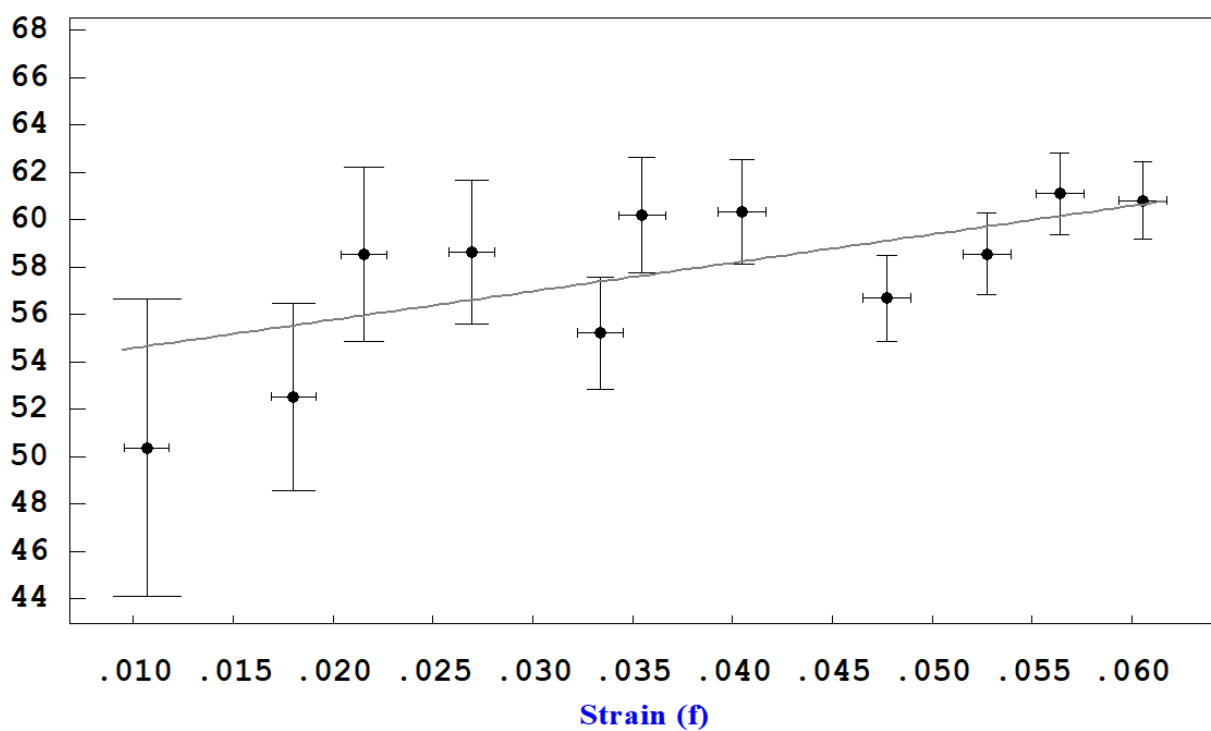
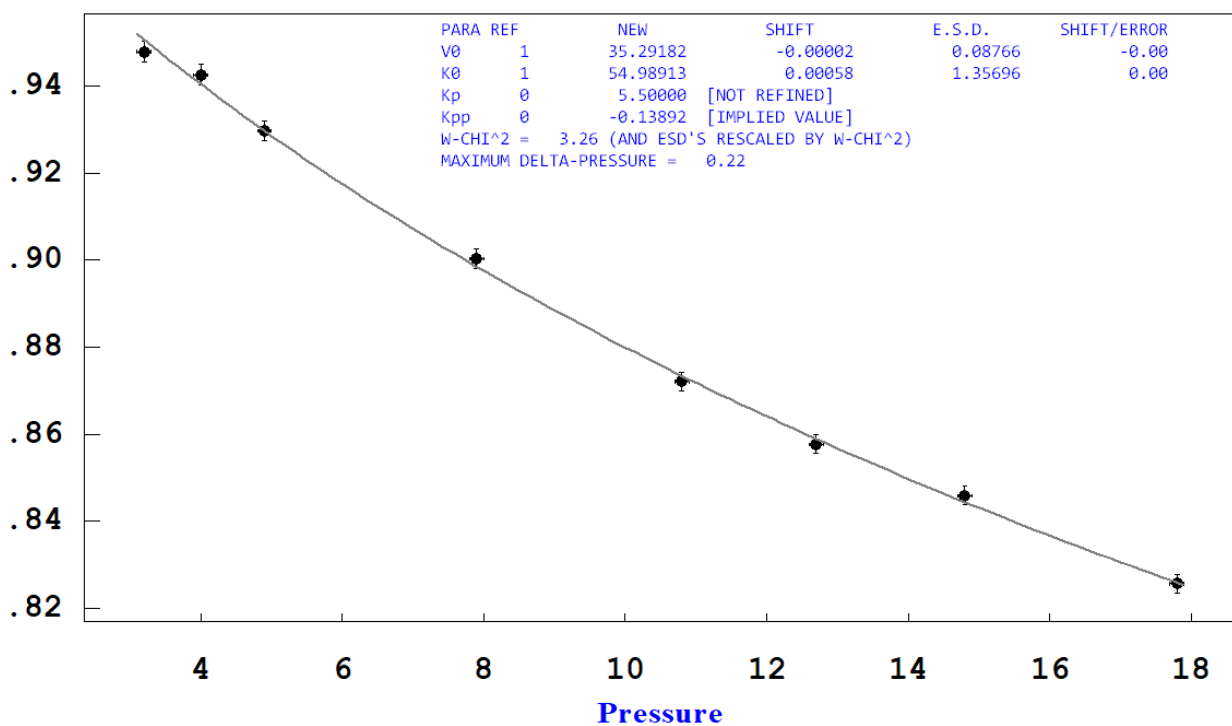


Figure S25. The fit of the volume per Yb atom to the third-order Birch-Murnaghan equation of state for P-31m phase of Yb₃H₈ compressed in Ne PTM (top) and the F-f plot (bottom). F – normalized pressure [GPa], f – Eulerian strain. Alternative run (h).

V/V₀



Normalized Pressure (F)

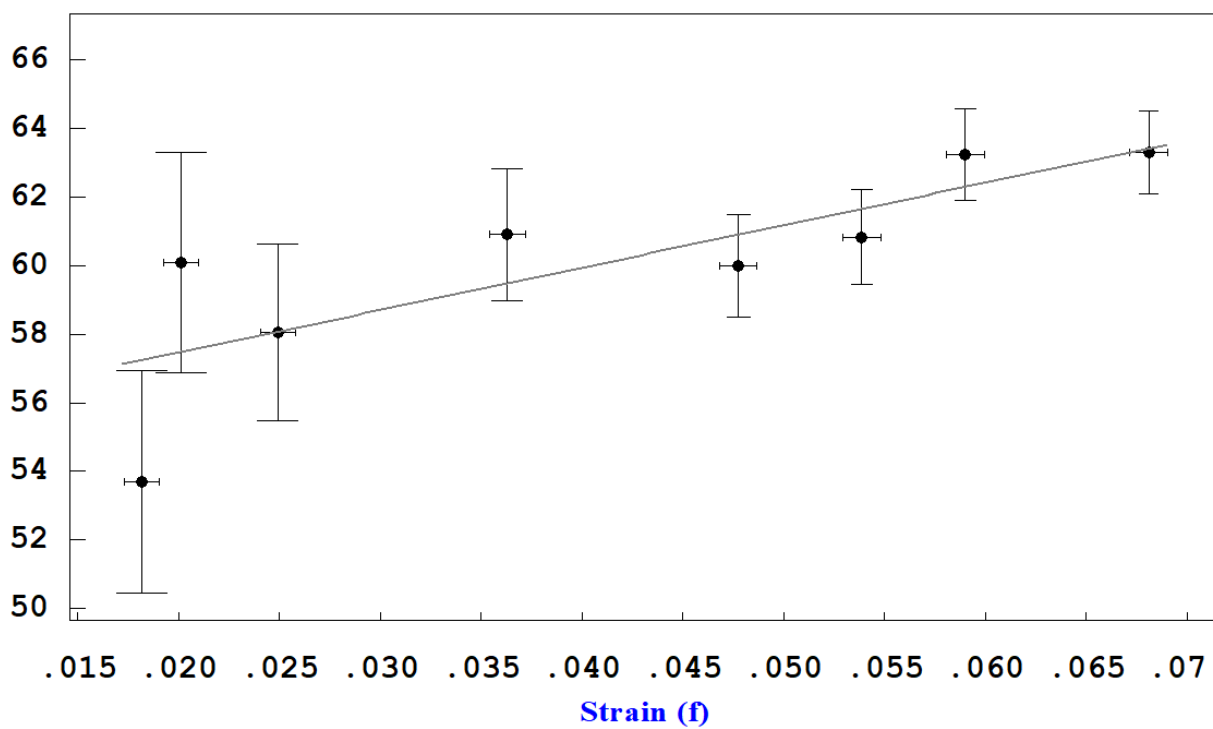
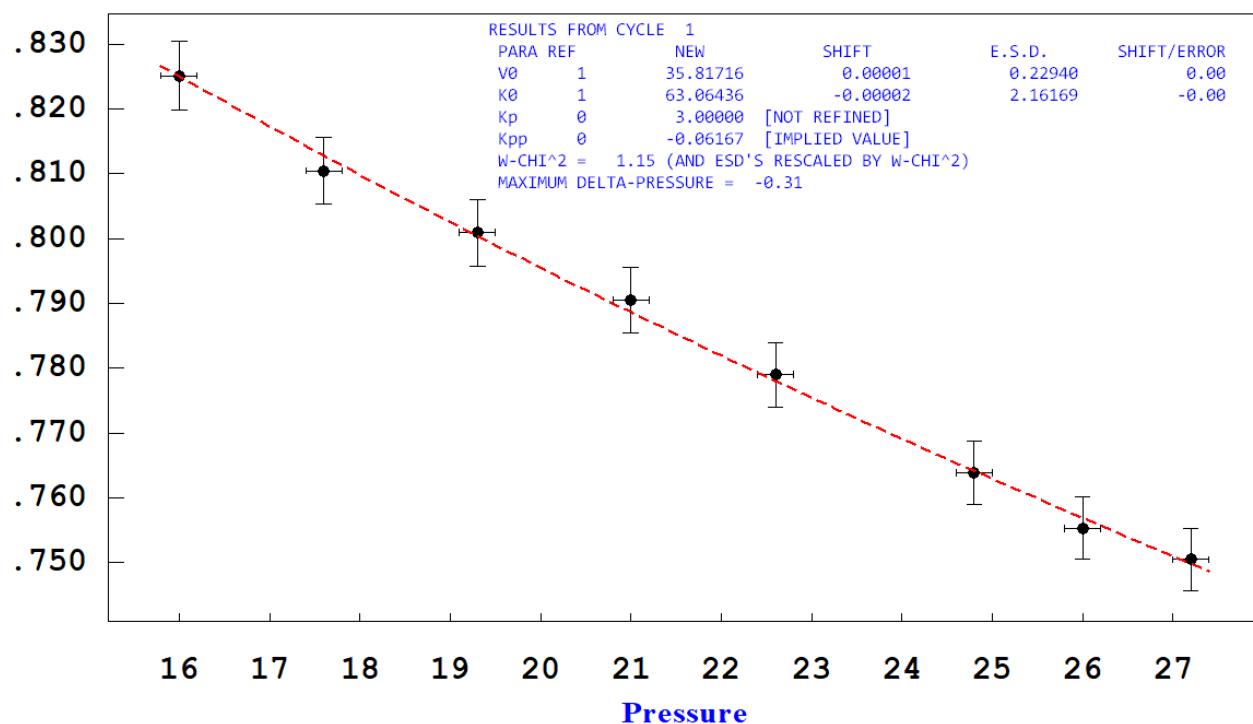


Figure S26. The fit of the volume per Yb atom to the third-order Birch-Murnaghan equation of state for P-31m phase of Yb₃H₈ compressed in H₂ PTM (top) and the F-f plot (bottom). F – normalized pressure [GPa], f – Eulerian strain. Run (d).

V/V₀



Normalized Pressure (F)

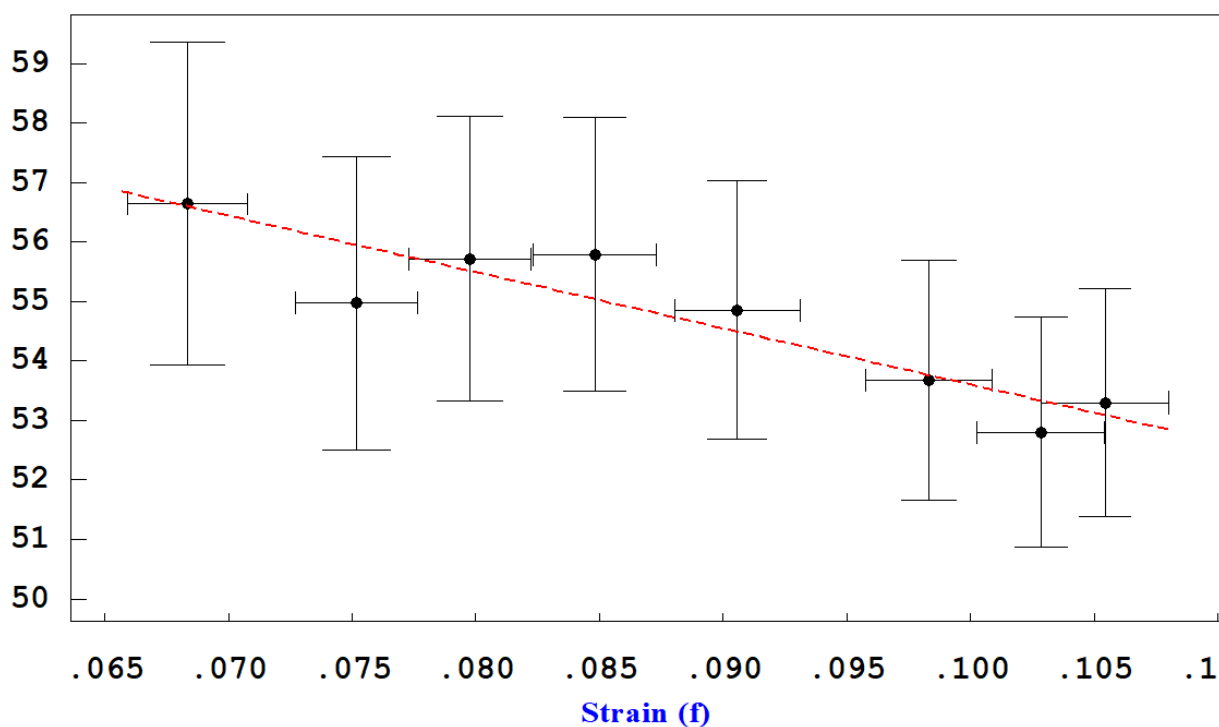
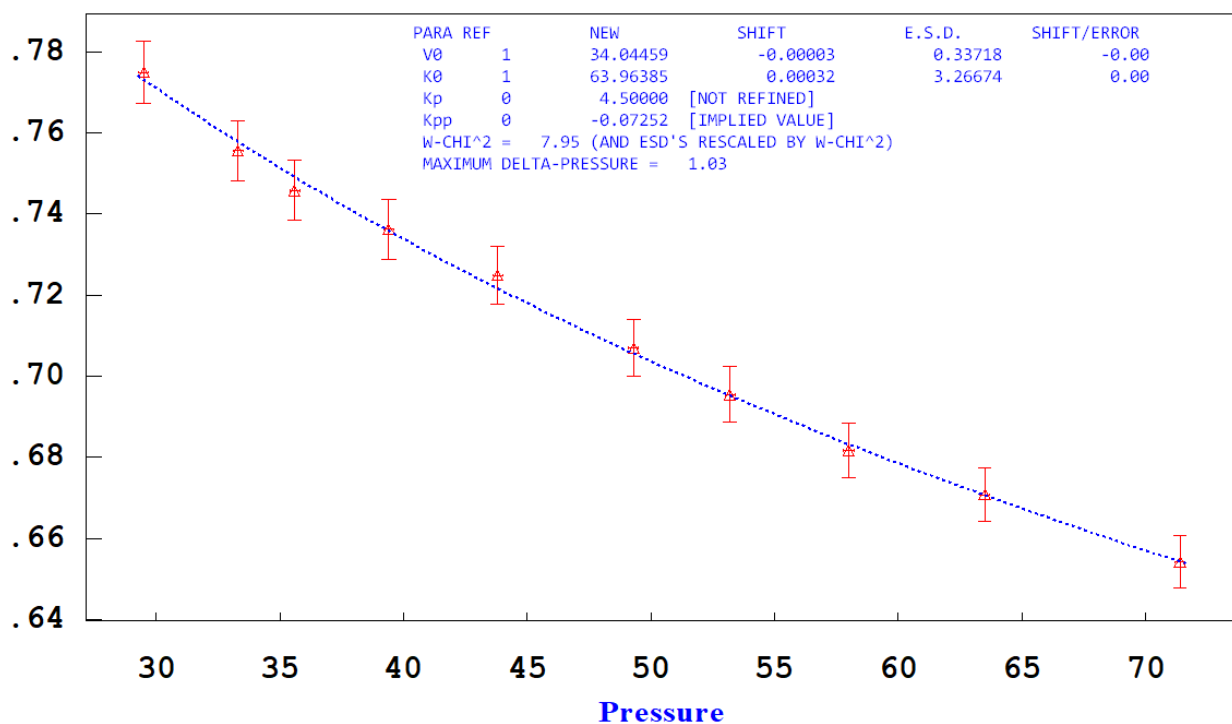


Figure S27. The fit of the volume per Yb atom to the third-order Birch-Murnaghan equation of state for I4/m phase of Yb₃H₈ compressed in Ne PTM (top) and the F–f plot (bottom). F – normalized pressure [GPa], f – Eulerian strain. Run (g).

V/V₀



Normalized Pressure (F)

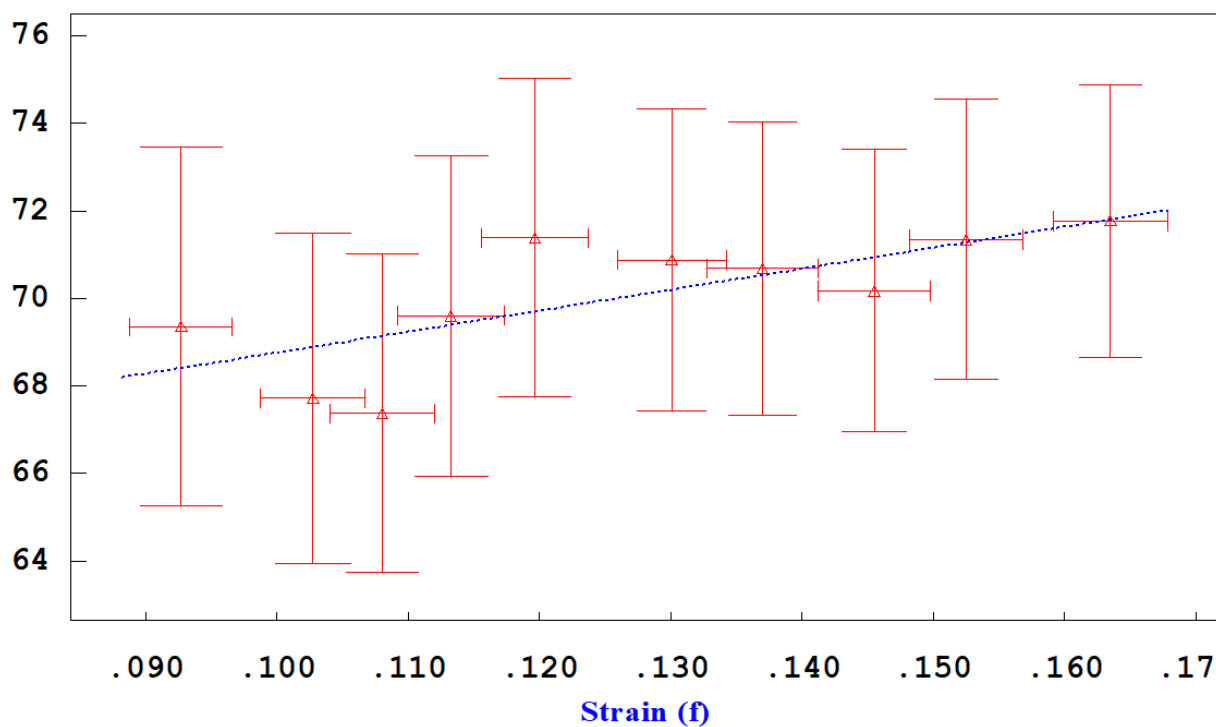
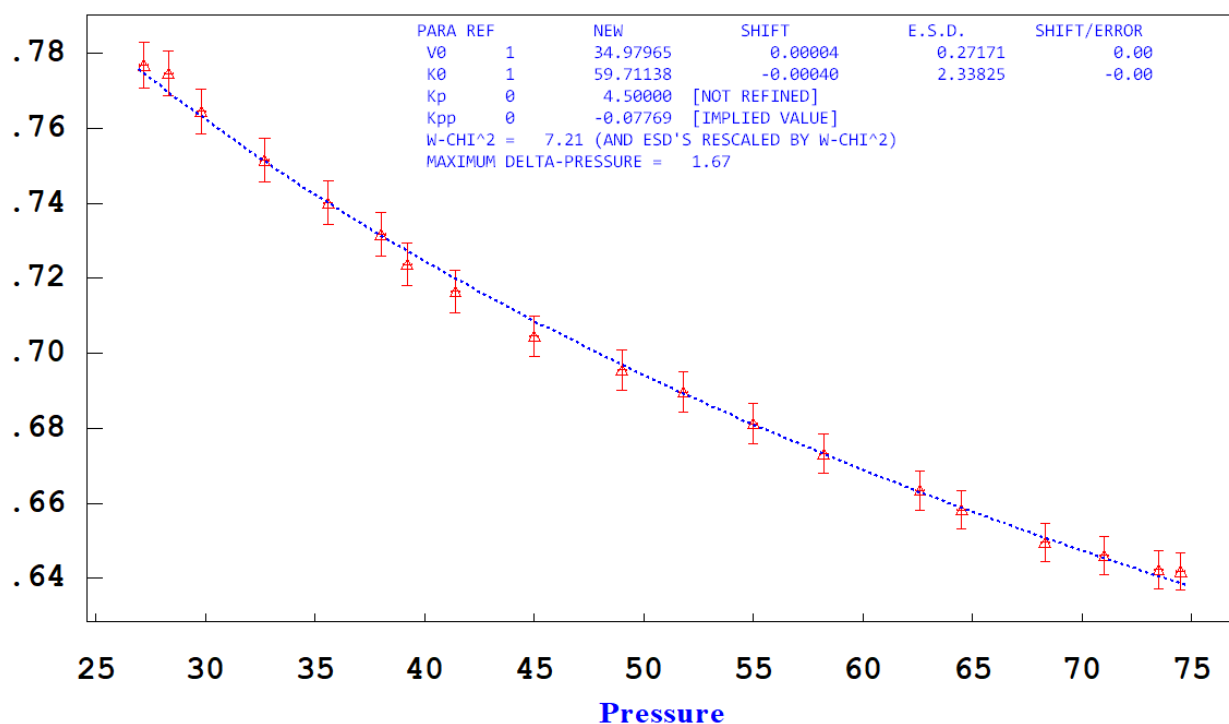


Figure S28. The fit of the volume per Yb atom to the third-order Birch-Murnaghan equation of state for I4/mmm phase of Yb₃H₈ compressed in Ne PTM (top) and the F–f plot (bottom). F – normalized pressure [GPa], f – Eulerian strain. run (i).

V/V₀



Normalized Pressure (F)

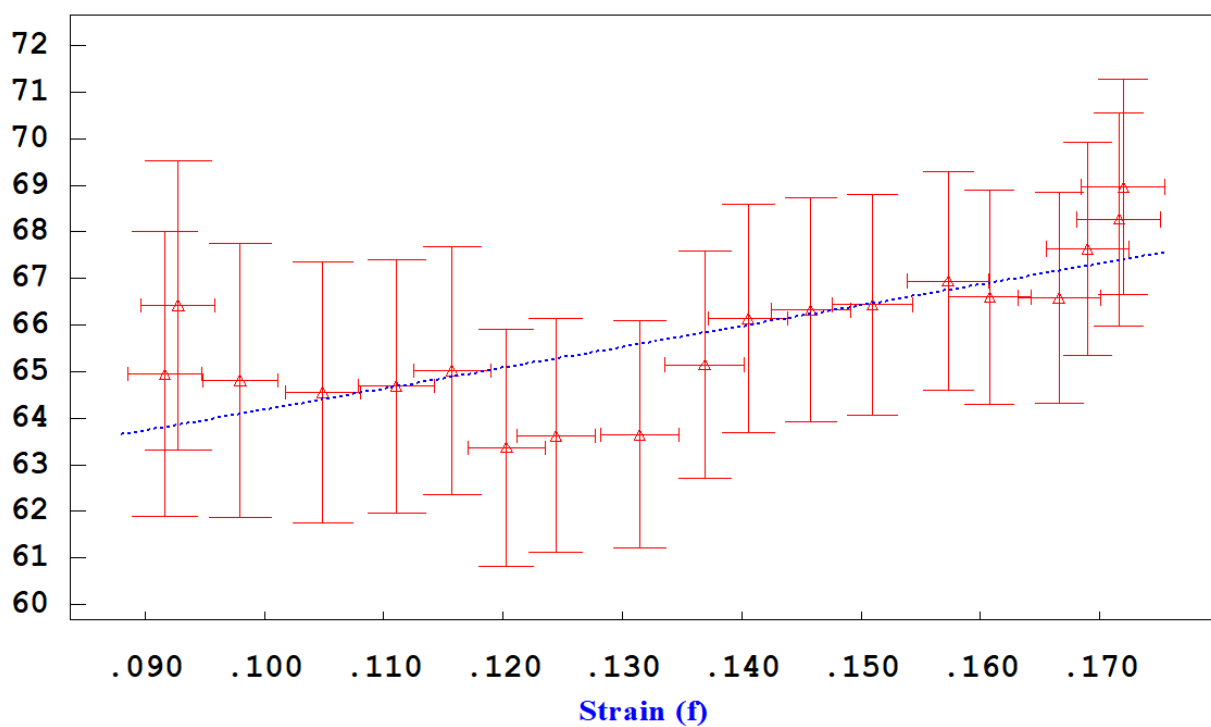


Figure S29. The fit of the volume per Yb atom to the third-order Birch-Murnaghan equation of state for $I4/mmm$ phase of Yb_3H_8 compressed in H_2 PTM (top) and the F - f plot (bottom). F – normalized pressure [GPa], f – Eulerian strain. run (d).

Table S2. Summary of the EoS parameters reported for some of the lanthanide hydrides relevant for this study. The estimated standard deviations (E.S.D.) are given in parentheses. EoS type: B-M – Birch-Murnaghan, M – Murnaghan.

phase	V_0 per metal atom [\AA^3]	B_0 [GPa]	B_0'	EoS type	notes	ref.
SmH₃ $P6_3/mmc$	41.68(33)	70(4)	4	M	silicone oil PTM	2
SmH₃ $Fm-3m$	38.69(33)	80(4)	4	M	silicone oil PTM	2
EuH₂ $Pnma$	42.6	39.9(5)	4	B-M	He PTM	3
EuH₂ $P6_3/mmc$	39.8(1)	44.9(9)	4	B-M	He PTM	3
EuH_{2+x} $I4/mmm$	38.8(2)	69(2)	4	B-M	H ₂ PTM; $I4/m$ phase shows similar compressibility	3
Eu₈H₄₆ $Pm-3n$	26.3(1)	471(70)	4	B-M	DFT – close to exp. data; V_0 at 100 GPa	4
EuH₉ $P6_3/mmc$	31.9(1)	594(70)	4	B-M	DFT – close to exp. data; V_0 at 100 GPa	4
EuH₉ $F-43m$	31.3(1)	699(27)	4	B-M	DFT – close to exp. data; V_0 at 100 GPa	4
TbH₃ $P6_3/mmc$	39.69	81	4	M	no PTM	5
TbH₃ $Fm-3m$	38.03	96	4	M	no PTM	5
DyH₃ $P6_3/mmc$	38.53	82	5.1	M	silicone oil PTM	6
DyH₃ $Fm-3m$	35.54	119	1.9	M	silicone oil PTM	6
DyH₃ $Fm-3m$	35.4(3)	85(3)	4	B-M	H ₂ PTM	7
HoH₃ $P6_3/mmc$	37.69	87(3)	4	M	silicone oil PTM	8
HoH₃ $Fm-3m$	36.20	90(2)	4	M	silicone oil PTM	8
ErH₃ $P6_3/mmc$	37.03	77(4)	4	M	silicone oil PTM	2
ErH₃ $Fm-3m$	35.70	81(3)	4	M	silicone oil PTM	2
TmH₃ $P-3c1$	35.69	84.94	3.22	B-M	DFT	9
TmH₃ $Fm-3m$	32.06	103.36	3.86	B-M	DFT	9
YbH₂ $Pnma$	35.63(7)	40.2(22)	4.75(45)	M	4:1 MeOH:EtOH PTM	10
YbH₂ $P6_3/mmc$	30.4(1)	138(3)	0	M	4:1 MeOH:EtOH PTM	10

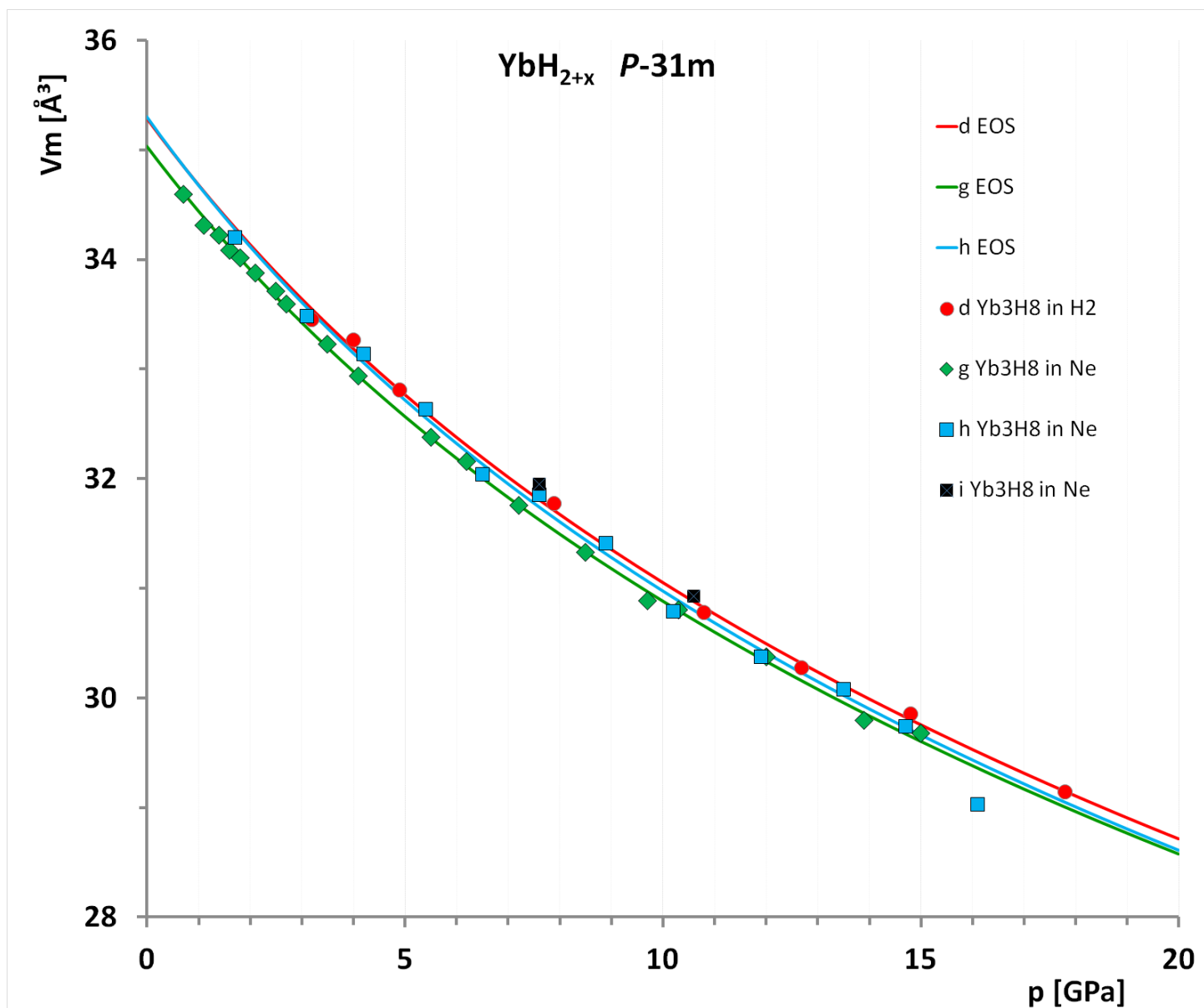


Figure S30. P-31m phase of Yb₃H₈ compressed in H₂ and Ne PTM. Comparison of the experimental data and EOS fitted.

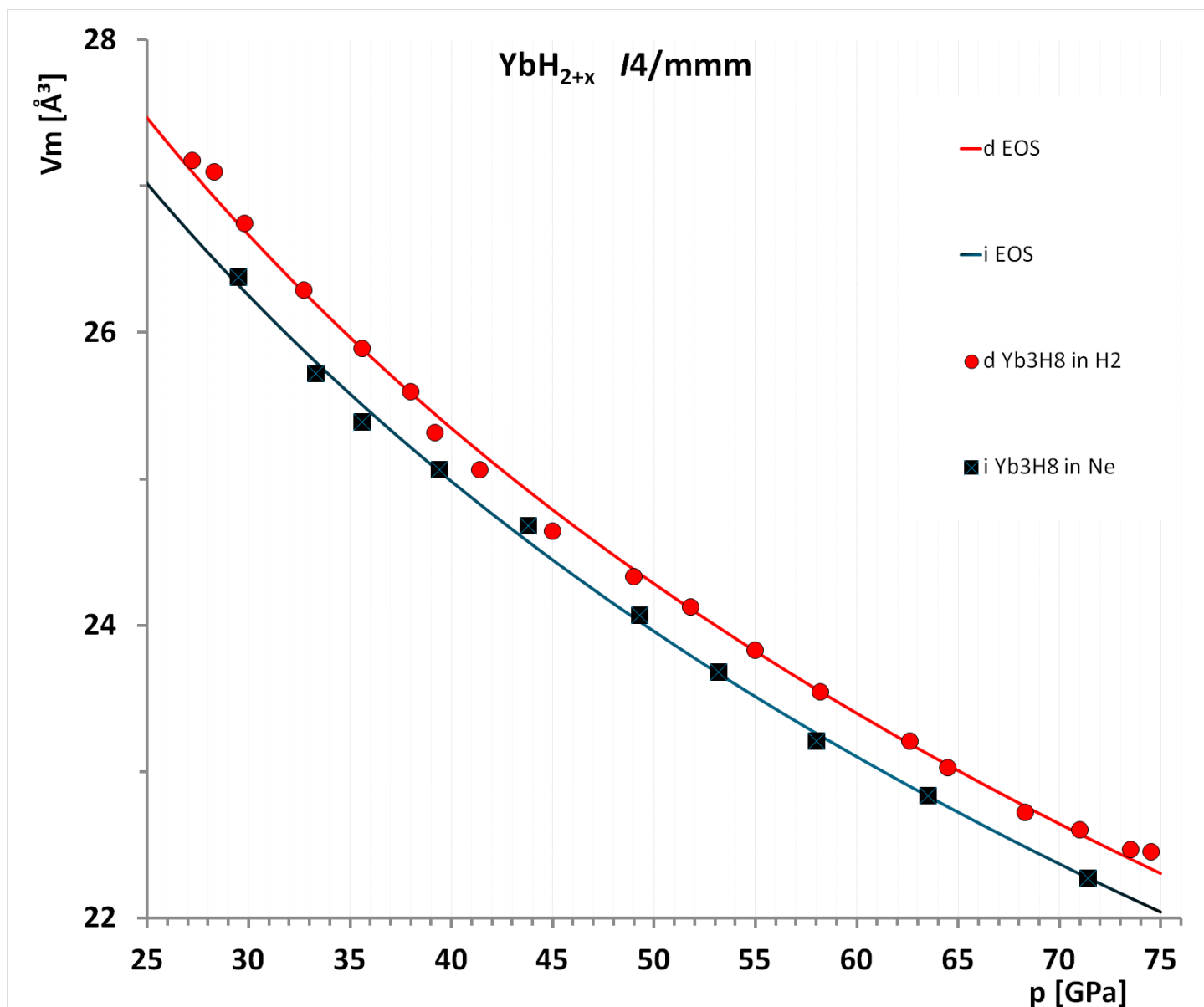


Figure S31. $I4/mmm$ phase of Yb_3H_8 compressed in H_2 and Ne PTM. Comparison of the experimental data and EOS fitted.

Table S3. Refined lattice parameters for Yb_3H_8 compressed in H_2 PTM. Run (d).

p [GPa]	YbH_{2+x} phase	a [Å]	a (e.s.d.)	c [Å]	c (e.s.d)	V/Z [Å ³]	c/a	cwRp [%]
3.2	P-31m	6.2625	9	8.8642	16	33.452	1.415	5.57
4.0		6.2491	4	8.8526	12	33.265	1.417	4.62
4.9		6.21623	13	8.8237	5	32.809	1.419	3.34
7.9		6.1535	4	8.7196	10	31.771	1.417	3.27
10.8		6.0898	5	8.6246	9	30.777	1.416	3.61
12.7		6.0497	4	8.5950	16	30.269	1.421	3.75
14.8		6.0441	5	8.4926	4	29.853	1.405	4.00
17.8		5.9762	8	8.4788	18	29.139	1.419	3.86
14.8	I4/m	7.7780	3	4.8923	3	29.597	0.629	4.00
17.8		7.6724	3	4.9259	3	28.997	0.642	3.86
20.6		7.6386	2	4.8978	3	28.578	0.641	5.65
21.7		7.6180	4	4.8849	5	28.349	0.641	7.52
24.0		7.5837	4	4.8612	5	27.958	0.641	6.83
27.2	I4/mmm	3.3679	3	4.7916	7	27.175	1.423	6.81
28.3		3.3613	4	4.7966	8	27.097	1.427	7.02
29.8		3.3470	5	4.7748	7	26.745	1.427	6.50
32.7		3.3270	9	4.7498	13	26.288	1.428	8.59
35.6		3.3100	13	4.726	2	25.889	1.428	11.18
38.0		3.2974	7	4.7082	9	25.596	1.428	7.26
39.2		3.2837	8	4.6955	11	25.315	1.430	7.72
41.4		3.2735	9	4.6778	13	25.063	1.429	7.76
45.0		3.2545	11	4.6537	18	24.645	1.430	8.42
49.0		3.2393	4	4.6375	9	24.331	1.432	8.38
51.8		3.2296	13	4.6258	17	24.124	1.432	8.66
55.0		3.2162	11	4.6075	14	23.830	1.433	7.34
58.2		3.2027	13	4.5912	19	23.547	1.434	8.51
62.6		3.1869	14	4.570	2	23.207	1.434	9.10
64.5		3.1778	13	4.560	2	23.024	1.435	8.82
68.3		3.1642	16	4.5392	18	22.724	1.435	6.86
71.0		3.1575	4	4.5341	10	22.602	1.436	8.22
73.5		3.1510	4	4.5261	10	22.469	1.436	7.67
74.5		3.1506	10	4.5236	17	22.451	1.436	8.31

Table S4. Refined lattice parameters for Yb_3H_8 compressed in Ne PTM. Run (g).

p [GPa]	YbH _{2+x} phase	a [Å]	a (e.s.d.)	c [Å]	c (e.s.d)	V/Z [Å ³]	c/a	cwRp [%]
0.7	P-31m	6.3317	6	8.967	3	34.592	1.416	5.31
1.1		6.3189	8	8.9311	18	34.314	1.413	5.47
1.4		6.3144	5	8.9195	12	34.221	1.413	4.78
1.6		6.3062	9	8.9072	12	34.085	1.412	4.82
1.8		6.3024	9	8.8999	12	34.016	1.412	4.97
2.1		6.2944	9	8.8869	10	33.880	1.412	4.81
2.5		6.2836	7	8.8737	11	33.714	1.412	4.43
2.7		6.2704	4	8.8793	16	33.594	1.416	4.78
3.5		6.2485	8	8.8444	17	33.228	1.415	5.31
4.1		6.2297	5	8.8207	16	32.940	1.416	5.40
5.5		6.1930	5	8.7739	15	32.380	1.417	5.89
6.2		6.1862	7	8.7334	16	32.160	1.412	5.43
7.2		6.1605	9	8.696	2	31.757	1.412	6.06
8.5		6.1270	7	8.6720	18	31.326	1.415	6.23
9.7		6.0967	6	8.6347	17	30.883	1.416	6.26
10.3		6.0908	9	8.6283	18	30.801	1.417	6.44
12		6.0617	7	8.5905	20	30.374	1.417	6.73
13.9		6.0427	3	8.4800	14	29.795	1.403	6.30
15		6.0333	9	8.4730	13	29.678	1.404	6.47
16.0	I4/m	7.7369	5	4.9373	7	29.554	0.638	4.61
17.6		7.6878	5	4.9117	7	29.029	0.639	5.82
19.3		7.6529	4	4.8981	5	28.687	0.640	4.58
21		7.6211	3	4.8752	5	28.316	0.640	3.41
22.6		7.5853	3	4.8494	6	27.902	0.639	3.79
24.8		7.5378	7	4.8156	7	27.361	0.639	4.36
26		7.5088	4	4.7985	5	27.055	0.639	4.27
27.2		7.4926	4	4.7883	5	26.881	0.639	4.71
28.9	I4/mmm	3.3381	4	4.7733	7	26.594	1.430	5.34
29.8		3.332	4	4.7637	6	26.444	1.430	5.12
30.6		3.324	3	4.7535	5	26.261	1.430	5.73
32.3		3.3154	2	4.7425	6	26.064	1.430	5.48
33.3		3.3079	4	4.7316	6	25.887	1.430	5.15
34.6		3.3036	7	4.7252	10	25.785	1.430	6.95
35.7		3.296	8	4.7148	14	25.610	1.430	7.35
37.9		3.2882	7	4.7042	13	25.432	1.431	7.09
39.3		3.2794	7	4.6923	13	25.232	1.431	7.21
41.5		3.2681	7	4.6783	16	24.983	1.432	7.92

Table S5. Refined lattice parameters for Yb_3H_8 compressed in Ne PTM. Run (i).

p [GPa]	YbH_{2+x} phase	a [Å]	a (e.s.d.)	c [Å]	c (e.s.d.)	V/Z [Å ³]	c/a	cwRp [%]
7.6	$P\text{-}31m$	6.15735	9	8.7581	3	31.951	1.422	4.32
10.6		6.0946	2	8.6523	7	30.925	1.420	6.83
17.1	$I4/m$	7.7117	3	4.8952	5	29.112	0.635	5.56
19.3		7.6438	7	4.8827	8	28.528	0.639	8.70
23.9		7.5509	3	4.8080	4	27.413	0.637	6.50
29.5	$I4/mmm$	3.3469	2	4.7099	6	26.380	1.407	7.85
33.3		3.3054	2	4.7086	5	25.722	1.425	8.73
35.6		3.2930	5	4.6825	4	25.388	1.422	7.99
39.4		3.2797	5	4.6601	8	25.063	1.421	11.59
43.8		3.2619	6	4.6386	10	24.677	1.422	8.88
49.3		3.2344	4	4.6011	6	24.067	1.423	10.51
53.2		3.2185	2	4.5714	5	23.677	1.420	8.70
58		3.1957	5	4.5453	7	23.209	1.422	8.22
63.5		3.17532	19	4.5299	7	22.837	1.427	10.74
71.4		3.1497	2	4.4900	7	22.272	1.426	12.51

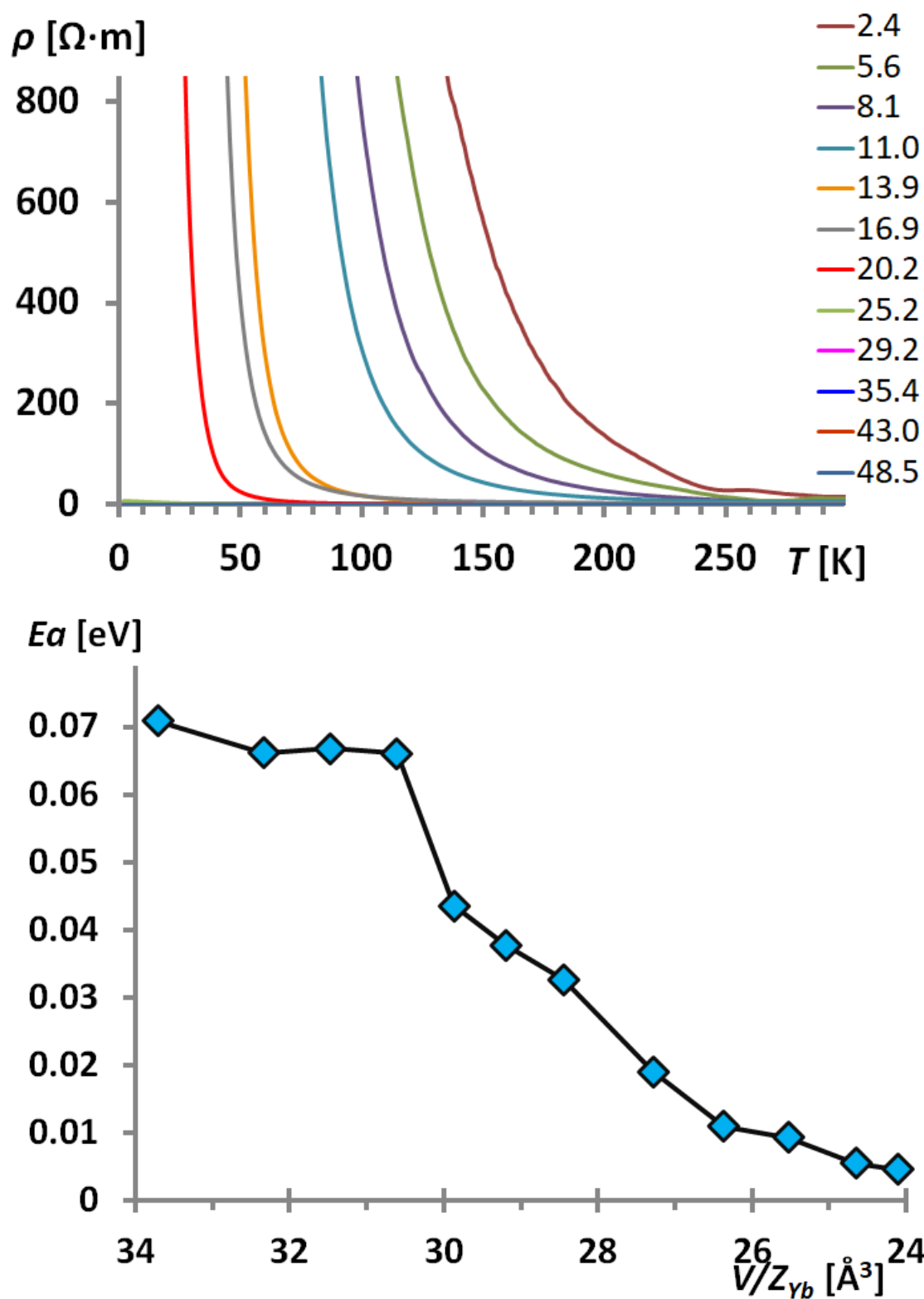


Figure S32. The resistivity vs. T [K] for Yb_3H_8 compressed in NaCl presented in a linear scale indicating semiconductor-like behavior (top). Evolution of the activation energy of the electronic transport in the function of volume per ytterbium atom (bottom).

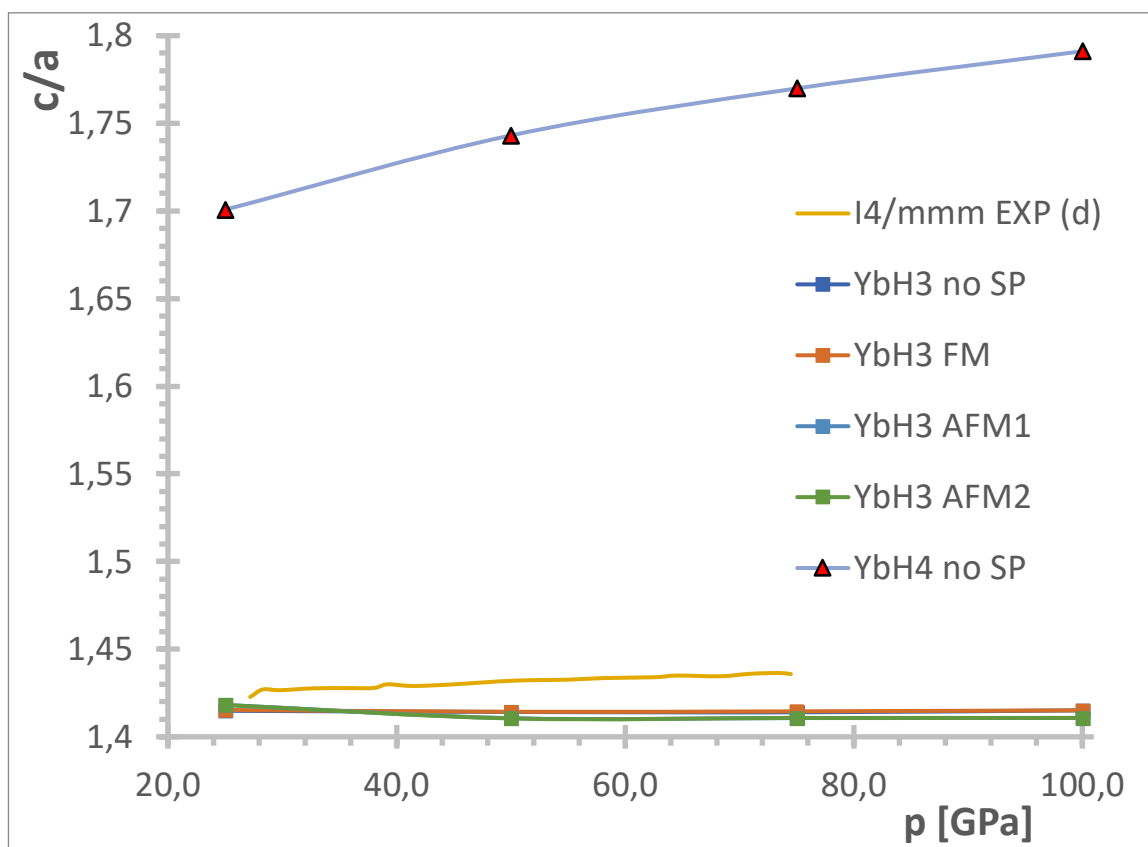
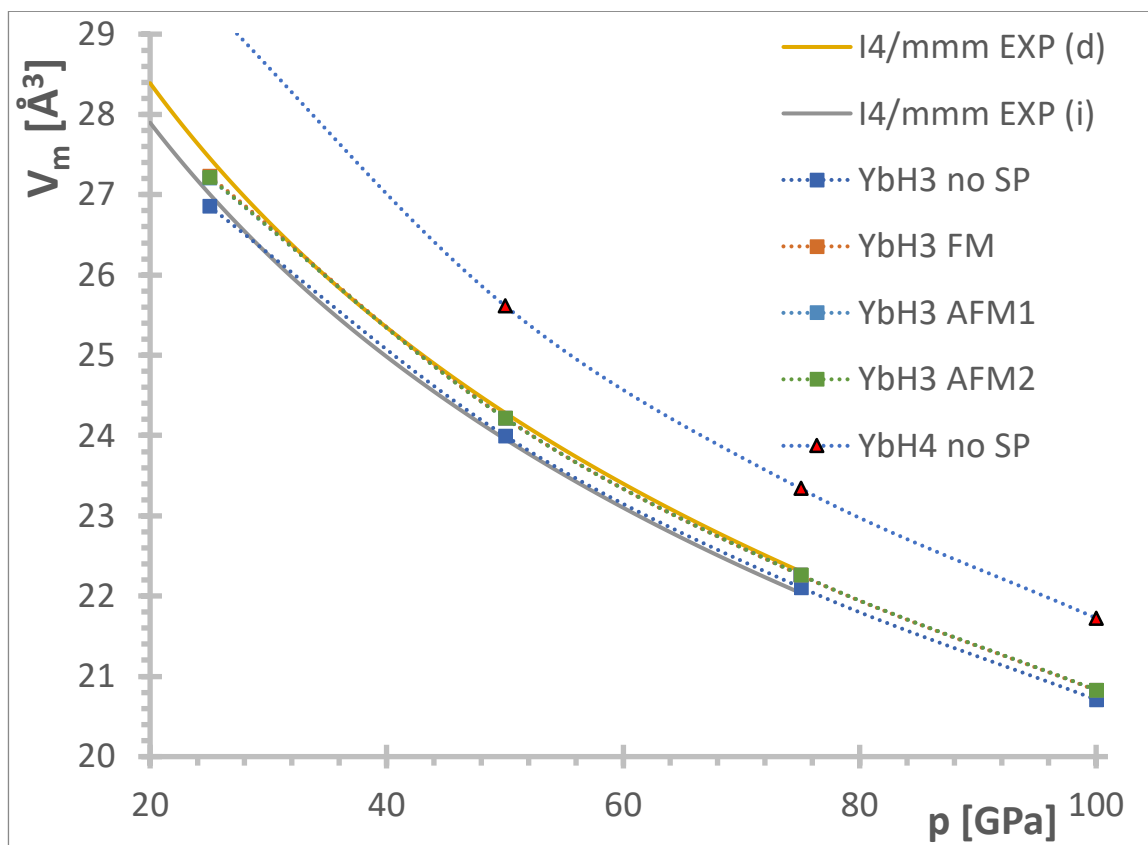


Figure S33. Top – The calculated molar volume of YbH₃ and YbH₄ (both I4/mmm) compared to the experimental results. Bottom – the calculated c/a ratio as compared to the experimental results.

CIF files: basic parameters, experimental data

Yb₃H₈ P-31m

Yb3H8 in Ne, 1.7 GPa (run (h)); LeBail fit (*cf. Fig. S16*)

```
#=====
# CRYSTAL DATA
#-----
data_phase_1

_chemical_formula_sum      'H2.67 Yb1'
_cell_length_a             6.30366(9)
_cell_length_b             6.30366(9)
_cell_length_c             8.9455(3)
_cell_angle_alpha          90
_cell_angle_beta           90
_cell_angle_gamma          120
_cell_volume               307.835(12)
_space_group_name_H-M_alt  'P -3 1 m'
_space_group_IT_number     162

loop_
_space_group_symop_operation_xyz
  'x, y, z'
  '-x, -y, -z'
  '-y, x-y, z'
  'y, -x+y, -z'
  '-x+y, -x, z'
  'x-y, x, -z'
  '-y, -x, -z'
  'y, x, z'
  '-x+y, y, -z'
  'x-y, -y, z'
  'x, x-y, -z'
  '-x, -x+y, z'

loop_
_atom_site_label
_atom_site_occupancy
_atom_site_fract_x
_atom_site_fract_y
_atom_site_fract_z
_atom_site_adp_type
_atom_site_U_iso_or_equiv
_atom_site_type_symbol
Yb1      1.0  0.000000  0.000000  0.000000  Uiso  0.025800 Yb
Yb2      1.0  0.333333  0.666667  0.000000  Uiso  0.025800 Yb
Yb3      1.0  0.3484(7) 0.000000  0.3292(13) Uiso  0.025800 Yb
H1       1.0  0.000000  0.000000  0.644000  Uiso  0.019000 H
H2       1.0  0.333333  0.666667  0.219000  Uiso  0.019000 H
H3       1.0  0.322000  0.000000  0.581200  Uiso  0.019000 H
H4       1.0  0.356000  0.000000  0.075700  Uiso  0.019000 H
H5       1.0  0.236400  0.000000  0.831900  Uiso  0.019000 H
```

"YbH₃" I4/m

Yb + H₂, sample heated *in situ*, ca. 12.5 GPa (run (c)); Rietveld fit (*cf.* Fig. S8)

#=====

CRYSTAL DATA

#-----

data_phase_2

_chemical_formula_sum 'H3 Yb1'
_cell_length_a 7.8268(3)
_cell_length_b 7.8268(3)
_cell_length_c 5.0150(3)
_cell_angle_alpha 90
_cell_angle_beta 90
_cell_angle_gamma 90
_cell_volume 307.21(2)
_space_group_name_H-M_alt 'I 4/m'
_space_group_IT_number 87

loop_

_space_group_symop_operation_xyz

'x, y, z'
'-x, -y, -z'
'-x, -y, z'
'x, y, -z'
'-y, x, z'
'y, -x, -z'
'y, -x, z'
'-y, x, -z'
'x+1/2, y+1/2, z+1/2'
'-x+1/2, -y+1/2, -z+1/2'
'-x+1/2, -y+1/2, z+1/2'
'x+1/2, y+1/2, -z+1/2'
'-y+1/2, x+1/2, z+1/2'
'y+1/2, -x+1/2, -z+1/2'
'y+1/2, -x+1/2, z+1/2'
'-y+1/2, x+1/2, -z+1/2'

loop_

_atom_site_label
_atom_site_occupancy
_atom_site_fract_x
_atom_site_fract_y
_atom_site_fract_z
_atom_site_adp_type
_atom_site_U_iso_or_equiv
_atom_site_type_symbol
Yb1 1.0 0.000000 0.000000 0.000000 Uiso 0.010000 Yb
Yb2 1.0 0.4109(7) 0.2013(13) 0.000000 Uiso 0.010000 Yb
H1 1.0 0.000000 0.000000 0.500000 Uiso 0.010000 H
H2 1.0 0.091400 0.307700 0.000000 Uiso 0.010000 H
H3 1.0 0.202200 0.107800 0.239600 Uiso 0.010000 H
H4 1.0 0.000000 0.500000 0.250000 Uiso 0.010000 H

"YbH₃" I4/mmm

Yb3H8 in Ne, 28.9 GPa (run (g)); LeBail fit (*cf. Fig. S19*). The H occupancies may vary.

#=====

CRYSTAL DATA

#-----

data_phase_3

_chemical_formula_sum	'H3 Yb1'
_cell_length_a	3.3381(4)
_cell_length_b	3.3381(4)
_cell_length_c	4.7733(7)
_cell_angle_alpha	90
_cell_angle_beta	90
_cell_angle_gamma	90
_cell_volume	53.190(12)
_space_group_name_H-M_alt	'I 4/m m m'
_space_group_IT_number	139

loop_

_space_group_symop_operation_xyz

'x, y, z'
'-x, -y, -z'
'-x, -y, z'
'x, y, -z'
'-y, x, z'
'y, -x, -z'
'y, -x, z'
'-y, x, -z'
'-x, y, -z'
'x, -y, z'
'x, -y, -z'
'-x, y, z'
'y, x, -z'
'-y, -x, z'
'-y, -x, -z'
'y, x, z'
'x+1/2, y+1/2, z+1/2'
'-x+1/2, -y+1/2, -z+1/2'
'-x+1/2, -y+1/2, z+1/2'
'x+1/2, y+1/2, -z+1/2'
'-y+1/2, x+1/2, z+1/2'
'y+1/2, -x+1/2, -z+1/2'
'y+1/2, -x+1/2, z+1/2'
'-y+1/2, x+1/2, -z+1/2'
'-x+1/2, y+1/2, -z+1/2'
'x+1/2, -y+1/2, z+1/2'
'x+1/2, -y+1/2, -z+1/2'
'-x+1/2, y+1/2, z+1/2'
'y+1/2, x+1/2, -z+1/2'
'-y+1/2, -x+1/2, z+1/2'
'-y+1/2, -x+1/2, -z+1/2'
'y+1/2, x+1/2, z+1/2'

loop_

_atom_site_label
_atom_site_occupancy

```

_atom_site_fract_x
_atom_site_fract_y
_atom_site_fract_z
_atom_site_adp_type
_atom_site_U_iso_or_equiv
_atom_site_type_symbol
Yb1    1.0  0.000000  0.000000  0.000000  Uiso 0.020000 Yb
H1     1.0  0.000000  0.000000  0.500000  Uiso 0.020000 H
H2     1.0  0.000000  0.500000  0.250000  Uiso 0.020000 H

```

Yb3H8 in H₂, 73.5 GPa (run (d)); LeBail fit (*cf. Fig. S14*). The H occupancies may vary.

```

#=====
# CRYSTAL DATA
#-----
data_phase_3

_chemical_formula_sum      'H3 Yb1'
_cell_length_a             3.1510(4)
_cell_length_b             3.1510(4)
_cell_length_c             4.5261(10)
_cell_angle_alpha          90
_cell_angle_beta           90
_cell_angle_gamma          90
_cell_volume               44.938(12)
_space_group_name_H-M_alt  'I 4/m m m'
_space_group_IT_number     139

loop_
_space_group_symop_operation_xyz
'x, y, z'
'-x, -y, -z'
'-x, -y, z'
'x, y, -z'
'-y, x, z'
'y, -x, -z'
'y, -x, z'
'-y, x, -z'
'-x, y, -z'
'x, -y, z'
'x, -y, -z'
'-x, y, z'
'y, x, -z'
'-y, -x, z'
'-y, -x, -z'
'y, x, z'
'x+1/2, y+1/2, z+1/2'
'-x+1/2, -y+1/2, -z+1/2'
'-x+1/2, -y+1/2, z+1/2'
'x+1/2, y+1/2, -z+1/2'
'-y+1/2, x+1/2, z+1/2'
'y+1/2, -x+1/2, -z+1/2'

```

'y+1/2, -x+1/2, z+1/2'
 '-y+1/2, x+1/2, -z+1/2'
 '-x+1/2, y+1/2, -z+1/2'
 'x+1/2, -y+1/2, z+1/2'
 'x+1/2, -y+1/2, -z+1/2'
 '-x+1/2, y+1/2, z+1/2'
 'y+1/2, x+1/2, -z+1/2'
 '-y+1/2, -x+1/2, z+1/2'
 '-y+1/2, -x+1/2, -z+1/2'
 'y+1/2, x+1/2, z+1/2'

```

loop_
  _atom_site_label
  _atom_site_occupancy
  _atom_site_fract_x
  _atom_site_fract_y
  _atom_site_fract_z
  _atom_site_adp_type
  _atom_site_U_iso_or_equiv
  _atom_site_type_symbol
Yb1      1.0  0.000000  0.000000  0.000000  Uiso  0.012700 Yb
H1       1.0  0.000000  0.000000  0.500000  Uiso  0.038000 H
H2       1.0  0.000000  0.500000  0.250000  Uiso  0.038000 H
  
```


Supporting references

- (1) Jacobsen, S. D.; Holl, C. M.; Adams, K. A.; Fischer, R. A.; Martin, E. S.; Bina, C. R.; Lin, J. F.; Prakapenka, V. B.; Kubo, A.; Dera, P. Compression of Single-Crystal Magnesium Oxide to 118 GPa and a Ruby Pressure Gauge for Helium Pressure Media. *Am. Mineral.* **2008**, *93* (11–12), 1823–1828. <https://doi.org/10.2138/am.2008.2988>.
- (2) Palasyuk, T.; Tkacz, M. Pressure-Induced Structural Phase Transition in Rare-Earth Trihydrides. Part II. SmH₃ and Compressibility Systematics. *Solid State Commun.* **2007**, *141* (5), 302–305. <https://doi.org/10.1016/j.ssc.2006.06.045>.
- (3) Matsuoka, T.; Fujihisa, H.; Hirao, N.; Ohishi, Y.; Mitsui, T.; Masuda, R.; Seto, M.; Yoda, Y.; Shimizu, K.; Machida, A.; Aoki, K. Erratum: Structural and Valence Changes of Europium Hydride Induced by Application of High-Pressure H₂ (Physical Review Letters (2011) 107 (025501) DOI: 10.1103/PhysRevLett.107.025501). *Phys. Rev. Lett.* **2019**, *122* (17), 179901. <https://doi.org/10.1103/PhysRevLett.122.179901>.
- (4) Semenok, D. V.; Zhou, D.; Kvashnin, A. G.; Huang, X.; Galasso, M.; Kruglov, I. A.; Ivanova, A. G.; Gavriluk, A. G.; Chen, W.; Tkachenko, N. V.; Boldyrev, A. I.; Troyan, I.; Oganov, A. R.; Cui, T. Novel Strongly Correlated Europium Superhydrides. *J. Phys. Chem. Lett.* **2021**, *12* (1), 32–40. <https://doi.org/10.1021/acs.jpclett.0c03331>.
- (5) Palasyuk, T.; Saxena, S.; Zaleski-Ejgierd, P.; Tkacz, M. High Pressure Studies of Terbium Trihydride. X-Ray, Raman and DFT Investigations. *J. Alloys Compd.* **2014**, *597*, 58–62. <https://doi.org/10.1016/j.jallcom.2014.01.150>.
- (6) Meng, H.; Palasyuk, T.; Drozd, V.; Tkacz, M. Study of Phase Stability and Isotope Effect in Dysprosium Trihydride at High Pressure. *J. Alloys Compd.* **2017**, *722*, 946–952. <https://doi.org/10.1016/j.jallcom.2017.06.181>.
- (7) Salke, N. P.; Davari Esfahani, M. M.; Yedukondalu, N.; Zhang, Y.; Kruglov, I. A.; Zhou, J.; Greenberg, E.; Prakapenka, V. B.; Liu, J.; Oganov, A. R.; Lin, J. F. Prediction and Synthesis of Dysprosium Hydride Phases at High Pressure. *Inorg. Chem.* **2020**, *59* (8), 5303–5312. <https://doi.org/10.1021/acs.inorgchem.9b03078>.
- (8) Palasyuk, T.; Tkacz, M. Pressure-Induced Structural Phase Transition in Rare-Earth Trihydrides. Part I. (GdH₃, HoH₃, LuH₃). *Solid State Commun.* **2005**, *133* (7), 481–486. <https://doi.org/10.1016/j.ssc.2004.11.036>.
- (9) Kong, B.; Zhang, L.; Chen, X. R.; Zeng, T. X.; Cai, L. C. Structural Relative Stabilities and Pressure-Induced Phase Transitions for Lanthanide Trihydrides REH₃ (RE=Sm, Gd, Tb, Dy, Ho, Er, Tm, and Lu). *Phys. B Condens. Matter* **2012**, *407* (12), 2050–2057. <https://doi.org/10.1016/j.physb.2012.02.003>.
- (10) Olsen, J. S.; Buras, B.; Gerward, L.; Johansson, B.; Lebech, B.; Skriver, H. L.; Steenstrup, S. A New High-Pressure Phase and the Equation of State of YbH₂. *Phys. Scr.* **1984**, *29* (5), 503–507. <https://doi.org/10.1088/0031-8949/29/5/016>.